Tampere University

Laura Keto

# PHYSIOLOGY OF CEREBELLAR ASTROGLIA FOR MORPHOLOGICALLY DETAILED SINGLE-CELL MODELING

Faculty of Medicine and Health Technology

Master of Science Thesis

April 2021

# ABSTRACT


| | |
|---|---|
| Place: | TAMPERE UNIVERSITY<br>Faculty of Medicine and Health Technology |
| Author: | KETO, LAURA MARIA |
| Title: | Physiology of cerebellar astroglia for morphologically detailed single-cell modeling |
| Pages: | 76 |
| Supervisor: | Academy Research Fellow Tiina Manninen, D.Sc. |
| Reviewers: | Professor Matti Nykter, Academy Research Fellow Tiina Manninen |
| Date: | 30.4.2021 |


---


**Background and aims:**
This thesis investigates calcium dynamics in a morphologically detailed model of a cerebellar astroglial cell. Since neither realistic computational models nor whole-cell morphologies exist presently for the cerebellar astroglial cells, the research aimed at building a model for the most well-known astroglial cell type; the Bergmann glia. The essential biological properties of cerebellar astroglial cells were assessed for building the functional and morphologically realistic single-cell computational model. The suitability of the novel astroglial modeling and simulation tool, ASTRO, was evaluated for modeling cerebellar astroglial cells.

**Methods:**
A 3D reconstruction of a Bergmann glial appendage was recreated from a video file using AgiSoft Metashape and Blender. Statistical properties of the nanoscopic processes were quantified from the reconstructed appendage 3D-model with ASTRO. A Bergmann glial stem tree was built with NEURON Cell Builder tool according to values found from literature. The computational model of a complete Bergmann glial morphology was constructed in ASTRO by populating the stem tree with the nanoscopic processes based on the obtained statistical properties. Simulations for calcium wave dynamics with and without mobile buffers were conducted in ASTRO using the full model.

**Results:**
The Bergmann glial appendage morphology was successfully reproduced from the video file and utilized for determining statistical properties for the nanoscopic processes characteristic of Bergmann glia. The functionality of ASTRO was extended to better accommodate the modeling of Bergmann glial cells. Simulations for calcium wave with and without mobile buffers elucidated the highly variable spatiotemporal dynamics of calcium within the specialized morphological structures of Bergmann glial cells.

**Conclusions:**
In this work, for the first time a whole cerebellar astroglial cell was modeled in the detail of nanoscopic processes that characterize these cells. Simulations for calcium dynamics provided insight into the significance of the highly heterogeneous morphology of Bergmann glial cells. The ASTRO tool was well suited for modeling the best-known cerebellar astroglial cell type, Bergmann glia, after the implemented modifications.

# TIIVISTELMÄ

Paikka: TAMPEREEN YLIOPISTO
Lääketieteen ja terveysteknologian tiedekunta
Tekijä: KETO, LAURA MARIA
Otsikko: Pikkuaivojen astrogliasolujen fysiologia morfologisesti yksityiskohtaiseen yksisolumallinnukseen
Sivumäärä: 76
Ohjaajat: Akatemiatutkija, TkT Tiina Manninen
Tarkastajat: Professori Matti Nykter, akatemiatutkija Tiina Manninen
Päiväys: 30.4.2021

---

**Tutkimuksen tausta ja tavoitteet:**
Tässä työssä tutkitaan kalsiumin dynamiikkaa morfologisesti yksityiskohtaisessa pikkuaivojen astrogliasolun mallissa. Koska pikkuaivojen astrogliasoluille ei ole olemassa realistisia laskennallisia malleja tai kokosolujen morfologioita, tutkimuksen tarkoituksena oli rakentaa malli parhaiten tunnetulle astrogliasolutyypille; Bergmann glialle. Pikkuaivojen astrogliasolujen olennaiset biologiset ominaisuudet selvitettiin toiminnallisen ja morfologisesti realistisen yksittäissolumallin rakentamista varten. Uuden astrosyyttien mallinnus- ja simulointityökalun, ASTRO:n, soveltuvuus arvioitiin pikkuaivojen astrogliasolujen mallintamista varten.
**Tutkimusmenetelmät:**
3D-rekonstruktio Bergmann glian soluhaarakkeesta luotiin videotiedoston pohjalta käyttämällä AgiSoft Metashape ja Blender -ohjelmistoja. Tilastolliset ominaisuudet nanoskooppisille prosesseille kvantifioitiin rekonstruoidun soluhaarakkeen 3D-mallista. Bergmann glian solurunko rakennettiin NEURON-simulaattorin CellBuilder-ominaisuudella kirjallisuudesta löydettyjen arvojen perusteella. Solurunkoon liitettiin nanoskooppisia prosesseja mallille laskettujen tilastollisten ominaisuuksien perusteella. Laskennallinen malli kokonaiselle Bergmann glian morfologialla toteutettiin ASTRO-mallinnustyökalulla. Simulaatiot kalsiumaallon dynamiikoille ja kalsiumpuskuroinnille toteutettiin koko mallilla.
**Tutkimustulokset:**
Bergmann glian soluhaarakkeen morfologia luotiin onnistuneesti videotiedostosta ja sitä käytettiin Bergmann glialle ominaisten nanoskooppisten prosessien tilastollisten ominaisuuksien määrittämiseen. ASTRO-työkalun toiminnallisuutta laajennettiin vastaamaan paremmin Bergmannin gliasolujen mallintamista. Simulaatiot kalsiumaallolle mobiilipuskurin kanssa ja ilman sitä havainnollistivat erittäin vaihtelevaa kalsiumin ajallis-paikallista dynamiikkaa Bergmannin gliasolujen erikoistuneissa morfologisissa rakenteissa.
**Johtopäätelmät:**
Tässä työssä mallinnettiin ensimmäistä kertaa kokonaista pikkuaivojen astrogliasolua niille tyypillisten nanoskooppisten prosessien tarkkuudella. Simulaatiot kalsiumaallon dynamiikoille osoittivat Bergmannin gliasolujen erittäin heterogeenisen morfologian merkityksen. ASTRO-työkalu soveltui hyvin parhaiten tunnetun pikkuaivojen astrogliasolun, Bergmann glian, mallinnukseen työkaluun toteutettujen muutosten jälkeen.

# ACKNOWLEDGEMENTS

This Master's thesis was done in the Computational Neuroscience Research Group at Tampere University. I would like to express my deepest gratefulness to my supervisor Tiina Manninen, D.Sc., and the group leader Marja-Leena Linne, D.Sc., for giving me the opportunity to perform my thesis project in the fascinating field of computational neuroscience and providing me excellent guidance and support. I would like to thank the whole Computational Neuroscience group for the supportive work atmosphere, and in particular Ippa Seppälä for proofreading the thesis. I am very thankful to Prof. Helmut Kettenmann for providing the video file of Bergmann glial appendage.

This research was supported by Academy of Finland (decision Nos 326494 and 326495) and the European Union's Horizon 2020 framework Programme for Research and Innovation under the Specific Grant Agreement No. 785907 (Human Brain Project SGA2).

Tampere, 30th April 2021

Laura Keto

# CONTENTS

# LIST OF SYMBOLS AND ABBREVIATIONS

| | |
|---|---|
| $\alpha_1$AR | α-1 adrenergic receptor |
| ABC | ATP-binding cassette |
| AC | adenylyl cyclase |
| AMPA | α-amino-3-hydroxy-5-methyl-4-isoxazolepropionic acid |
| AMPAR | AMPA receptor |
| AQP4 | aquaporin-4 |
| Asc-1 | Asc-type amino acid transporter 1 |
| ASCT1 | neutral amino acid transporter A |
| ATP | adenosine triphosphate |
| Best-1 | Bestrophin-1 |
| BC | basket cell |
| BG | Bergmann glia |
| BV | blood vessel |
| CA | cerebellar astrocyte |
| $Ca^{2+}$ | calcium ion |
| cAMP | cyclic adenosine 3',5'-monophosphate |
| CBP | calcium binding protein |
| CF | climbing fiber |
| $Cl^-$ | chloride ion |
| CLC | chloride channel |
| CNS | central nervous system |
| Cx43 | connexin 43 |
| Cys | cystine |
| DA | dopamine |
| DAG | diacylglycerol |
| DCN | deep cerebellar nuclei |
| D-Ser | D-serine |
| E | embryonic day |
| EAAT | excitatory amino acid transporter |
| EM | electron microscopy |
| ER | endoplasmic reticulum |
| $ET_B$ | endothelin receptor B |
| FA | fibrous astrocyte |
| FLIM | fluorescence-lifetime imaging microscopy |
| FRAP | fluorescence recovery after photobleaching |
| GABA | γ-aminobutyric acid |
| $GABA_A$ | GABA type A receptor |
| GAT | GABA transporter |
| GC | Golgi cell |
| GFAP | glial fibrillary acidic protein |
| GLAST | glutamate aspartate transporter 1 |
| Glut | glutamate |
| GLT-1 | glutamate transporter 1 |
| Gly | glycine |
| GlyT1 | glycine transporter 1 |
| GPCR | G-protein–coupled receptors |
| GrC | granule cell |

| | |
|---|---|
| GUI | graphical user interface |
| $H^+$ | hydrogen |
| $H_1$ | histamine receptor |
| $H_2O$ | water |
| ICC | immunocytochemistry |
| IGS | immunogold staining |
| IHC | immunohistochemistry |
| IP | immunoprecipitation |
| $IP_3$ | inositol 1,4,5-trisphosphate |
| $IP_3R$ | $IP_3$ receptor |
| ISH | *in situ* hybridization |
| IO | inferior olive |
| $K^+$ | potassium ion |
| $K_{Ca}$ | calcium-dependent potassium channel |
| KCC1 | potassium-chloride cotransporter 1 |
| $K_{dr}$ | delayed rectifying potassium channel |
| $K_{ir}$ | inwardly rectifying potassium channel |
| $K_v$ | voltage-gated potassium channel |
| LAT1 | large neutral amino acid transporter 1 |
| MF | mossy fiber |
| mGluR | metabotropic glutamate receptor |
| ML | molecular layer |
| $Na^+$ | sodium ion |
| $Na_v1.6$ | voltage-gated sodium channel 1.6 |
| NCX | sodium/calcium exchanger |
| NKA | sodium/potassium-ATPase |
| NKCC1 | sodium-potassium-chloride cotransporter 1 |
| NMDA | N-methyl-D-aspartate |
| NMDAR | NMDA receptor |
| P | postnatal day |
| $P2X_7$ | purinergic ATP activated channel receptor subtype 7 |
| P2Y | purinergic ATP activated G protein-coupled receptor |
| PAP | peripheral astrocytic process |
| PC | Purkinje cell |
| PF | parallel fiber |
| PKC | protein kinase C |
| PLC | phospholipase C |
| PM | pia mater |
| PMCA | plasma membrane calcium-ATPase |
| PN | pontine nuclei |
| RN | red nuclei |
| RT-PCR | reverse transcription polymerase chain reaction |
| RYR3 | ryanodine receptor 3 |
| SC | stellate cell |
| Shh | sonic hedgehog |
| SERCA | sarcoplasmic/endoplasmic reticulum calcium adenosine triphosphatase |
| SLC | solute carrier transporter |
| SOCE | store-operated calcium entry |
| VA | velate astrocyte |
| VGLUT3 | vesicular glutamate transporter 3 |

| | |
|---|---|
| VNUT | vesicular nucleotide transporter |
| VRAC | volume-regulated anion channel |
| WB | western blot |
| WCPC | whole-cell patch-clamp |
| xCT | cystine/glutamate antiporter |

| | |
|---|---|
| $\gamma$ | calcium pump flux density |
| A | area |
| [A] | concentration of a substance A |
| $[Ca]_c$ | calcium pump activation threshold |
| $B_m$ | mobile buffer |
| $B_s$ | endogenous buffer |
| D | diameter |
| $D_A$ | diffusion coefficient of a substance A |
| F | Faraday constant |
| i | current |
| $J_b$ | reverse flux |
| $J_f$ | forward flux |
| $j_{max}$ | maximal $IP_3R$ mediated flux |
| $K_{act}$ | dissociation constant for calcium binding to $IP_3R$ activation site |
| $K_{Dm}$ | dissociation constant for a mobile buffer |
| $K_{Ds}$ | dissociation constant for a stationary buffer |
| $k_{fm}$ | reaction rate constant for a mobile buffer |
| $k_{fs}$ | reaction rate constant for a stationary buffer |
| $k_{on}$ | reaction rate constant of calcium binding to $IP_3R$ inhibition site |
| $K_{inh}$ | dissociation constant for calcium binding to $IP_3R$ inhibition site |
| $K_{IP3}$ | dissociation constant for $IP_3$ binding to $IP_3R$ activation site |
| $K_p$ | half-activation constant of a pump |
| L | leak constant |
| $\overline{P}_{Ca}$ | maximal calcium permeability |
| R | ideal gas constant |
| $R_{gap}$ | gap junction resistance |
| T | temperature |
| V | membrane potential |
| $V_{gap}$ | gap junction reversal potential |
| $v_{max}$ | maximum rate |

# 1. INTRODUCTION

Glial cells are a major cellular component of the brain, comprising more or less half of the cellular population in the brain (von Bartheld et al., 2016). However, their functional importance has been underappreciated in the past, most of the research focusing solely on neurons and their networks. Glial cells include three types of cells: microglia, oligodendrocytes, and astroglial cells, also called astrocytes. Astroglial cells, embedded into the three-dimensional architecture of the brain, both support and maintain neurons and their communications. They take part in the tripartite synapses (Araque et al., 1999), directly affecting the information flow in the brain, and communicate as a syndicate, filling most of the brain as a network of branching, interconnected sponge-like cells. In addition to their roles in the functioning of a healthy brain, astrocytes, together with other neural cells, determine the faith of diseased or disrupted brain.

Here the focus is on the Bergmann glia, the most well-studied astroglial cell type of the cerebellum. Bergmann glial cells are in close contact with the main neurons of the cerebellum, the Purkinje cells, with several Bergmann glial cells surrounding single Purkinje cells (Reichenbach et al., 1995). Bergmann glial morphology is characterized by soma, 2-6 main processes populated with numerous lateral processes of complex shapes, and endfeet (Palay & Chan-Palay, 1974). These morphological structures are decorated with assortments of channels, transporters, and receptors that allow Bergmann glia to both respond to and influence their environment. The main functions of Bergmann glia include calcium ($Ca^{2+}$) signaling, uptake of potassium ($K^{+}$) ions, and clearance of glutamate (Verkhratsky & Reichenbach, 2009).

Even though more is known about the Bergmann glia than the other astroglial cell types of the cerebellum, still more needs to be known about their function to elucidate their role in the cerebellum. Computational models provide a framework for testing and visualizing both experimental results and hypothetical conditions. These kind of *in silico* cell models have been implemented widely for neuronal cells, including single-cell models and network models (reviewed in D'Angelo et al., 2016). To date, realistic and accurate models exist for most of the cerebellar neurons. While studied to a significantly lower degree than neuronal cells, multiple models have emerged for single astrocytes, astrocyte networks, and astrocyte–neuron

interactions, including various models simulating $Ca^{2+}$ dynamics (reviewed in Manninen et al., 2018, 2019). Computational models and complete 3D morphologies can be found from public neuroscience databases for neural cells, but for cerebellar astroglial cells neither publicly available models nor morphologies yet exist. Only a handful of computational studies regarding cerebellar astroglial cell functions can be found from current literature.

One of the widely used simulation platforms for building and simulating models of neural cells as cylindrical structures is NEURON (Hines & Carnevale, 2001). Two models constructed in NEURON for Bergmann glia were found from literature; a single-cell model of the basic Bergmann glial morphology, including the soma, endfeet, and main processes but not the lateral processes (Dzubay & Jahr, 1999), and a detailed model for a Bergmann glial branch (Grosche et al., 2002). Building a single-cell model that reproduces the complete Bergmann glial morphology in detail, however, has been thus far unattainable in a computationally viable form.

The challenge of modeling astrocytes is their morphology, characterized by hundreds or thousands of nanoscopic processes. Due to computational constraints, realistic models able to capture the complete astrocytic morphology have been unattainable. ASTRO, a novel computational tool for astrocyte modeling based on the NEURON simulation platform, provides functionalities to reconstruct and simulate the complex astrocytic morphologies (Savtchenko et al., 2018). ASTRO utilizes a method for transforming the irregular nanoscopic processes into NEURON compatible stacks of cylinders, which, while simplified, retain the essential biophysical properties of the original astrocyte.

The regulation of free $Ca^{2+}$ ions is of particular importance in excitable cells like neurons but also in non-excitable cells like glial cells. The aim of this study is to build a morphologically detailed single-cell model for Bergmann glia to study the spatiotemporal dynamics of $Ca^{2+}$ with and without mobile $Ca^{2+}$ buffers. First, the basic context of cerebellar astroglial cells, from the level of the cerebellum to the cell circuitry they are embedded in, is reviewed. Next, the current knowledge on the single-cell properties of cerebellar astroglial cells is revised, with a focus on the properties of Bergmann glia. In the computational part, the morphometric and functional data will be utilized for building the Bergmann glial model. The nanoscopic processes of the Bergmann glia model will be created based on a Bergmann glial appendage morphology provided in a video format (Grosche et al., 1999), and the final model assembled with ASTRO.

This work has been presented as a poster at the 29th Annual Computational Neuroscience Meeting CNS*2020 (Keto & Manninen, 2020).

# 2. LITERATURE REVIEW

## 2.1 The cerebellum

The cerebellum (Latin for "little brain") is part of the hindbrain of all vertebrates. The cerebellum plays important roles both in movement and cognition. The cerebellum does not initiate movement; it is involved in the precise coordination and accurate timing of fine-tuned motor activity. Its roles in cognitive processes are less well-known, with possible functions in the regulation of emotional responses, attention, and language. (Adamaszek et al., 2017; Koziol et al., 2014)

### 2.1.1 Anatomy and connectivity

The cerebellum functions together with the cerebral cortex and basal ganglia as a dynamic organization (Caligiore et al., 2019; Doya, 1999). Distinct learning forms are associated with the different brain areas. Cerebral cortex is associated with unsupervised learning, where correlations in the input are detected and mapped, for example, via Hebbian mechanisms. In Hebbian learning, synapses are either weakened or strengthened based on the co-activity of neurons. Basal ganglia evaluate actions and adjust the associated synapses based on the reward prediction error of reinforcement learning. The prevailing learning form in the cerebellum is supervised, which is based on minimizing the error between the network output and the desired pattern.

The cerebellum is located at the base of the brain, underneath the cerebral cortex, and connected to other parts of the brain and body via portion of the brainstem called the pons (Figure 1) (Voogd & Glickstein, 1998). The outer layer of the cerebellum consists of gray matter, called the cerebellar cortex, which is a sheet-like structure with intricate layering of cells. Inside the cortex lies the cerebellar white matter, also known as *arbor vitae* or the Tree of Life, consisting of myelinated neuronal axons. Embedded into the white matter are four deep cerebellar nuclei, composed of gray matter. The innermost structure within the cerebellum, the fourth ventricle, is a cavity filled with cerebrospinal fluid. The two hemispheres of the cerebellar cortex are united by a region known as the vermis and divided into three lobes: anterior lobe, posterior lobe, and the flocculonodular lobe.

Afferent connections to the cerebellum comprise climbing fibers from the inferior olive and mossy fibers from multiple locations, including the cortex via the pontine nuclei, the reticular formation, and muscles via the spinocerebellar tracts (Figure 1) (Voogd & Glickstein, 1998). In addition, the cerebellum receives monoaminergic and cholinergic afferents. Efferent connections from the cerebellum are projected through the deep cerebellar nuclei to the brainstem, cortex, and spinal cord. The brainstem targets include the reticular formation, vestibular nuclei, superior colliculus, and red nuclei. The cortex receives signals from the cerebellum via the red nuclei and thalamus.

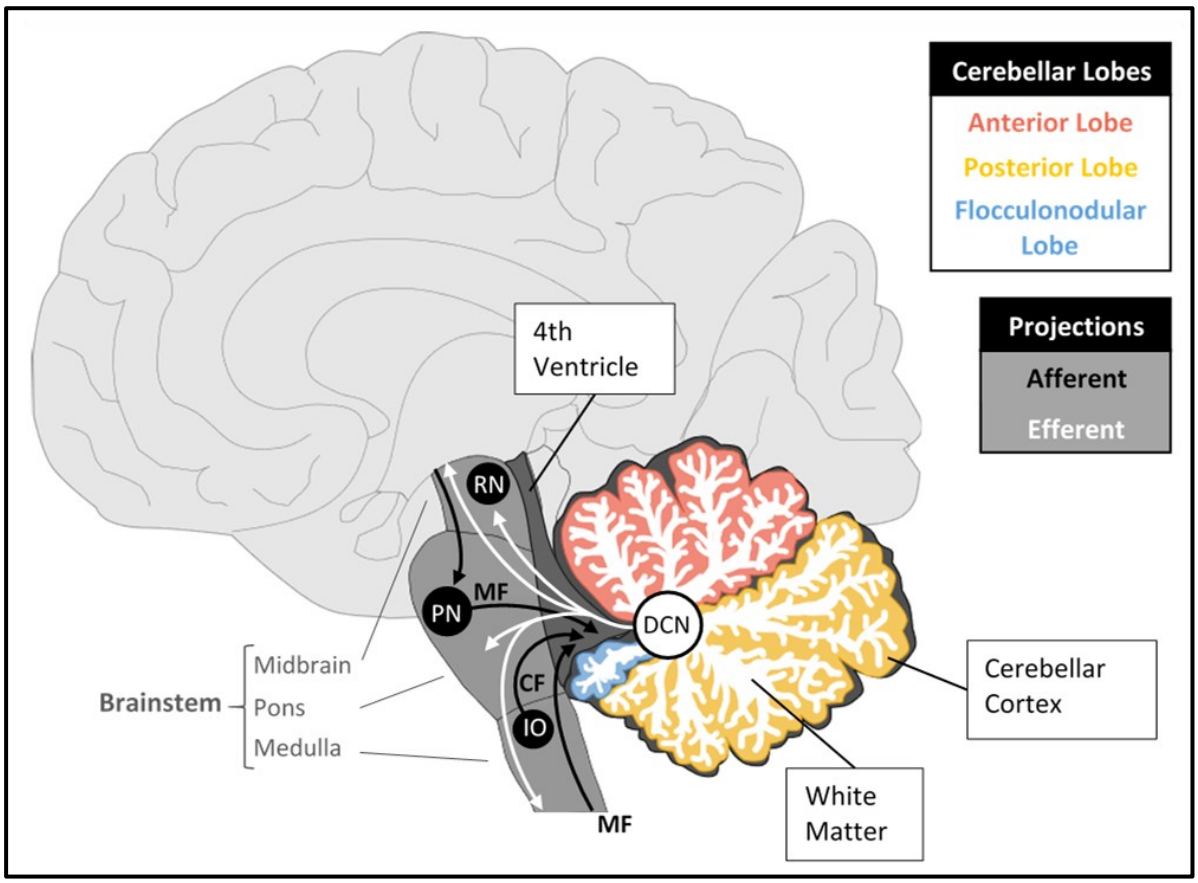


***Figure 1.*** *The cerebellar anatomy and connectivity (midsagittal view). The anatomical structures of the cerebellum are the 4th ventricle, deep cerebellar nuclei (DCN), white matter, and cerebellar cortex. The cerebellum consists of three main lobes. All of the afferent and efferent connections of the cerebellum are conveyed via the pons. Afferent connections comprise climbing fiber (CF) input from the inferior olive (IO) and mossy fibers (MF) input from many different locations, including from cortical locations via the pontine nuclei (PN) and from spinocerebellar tracts. The cerebellar output is relayed via the DCN to the cortex via the red nuclei (RN).CF, climbing fiber; DCN, deep cerebellar nuclei; IO, inferior olive; MF, mossy fiber; PN, pontine nuclei; RN, red nuclei.*

### 2.1.2 Zonal organization

The cerebellar anatomy is characterized by longitudinal and transverse zonal arrangement of the afferent and efferent axonal projections (Figure 2) (Apps & Hawkes, 2009). The deep cerebellar nuclei receive projections from defined longitudinal zones in the cerebellar cortex and target specific extracerebellar locations. The three main lobes are partitioned rostro-caudally by two deep fissures, the primary fissure and the posterolateral fissure; and further subdivided by shallow fissures into smaller lobules, or the transverse zones. Another deep fissure, the horizontal fissure, runs across the posterior lobe. Longitudinally, the cerebellum can be further divided into a striping pattern of alternating Z+ and Z– zones, determined by the prevalence of the marker protein Zebrin II in the Purkinje cells (Apps et al., 2018). The Z+ and Z– Purkinje cells are both histologically and functionally different, with differences in parallel fiber to Purkinje cell synapse plasticity and spontaneous firing rates (Zhou et al., 2014).

The functional module of the cerebellum is represented by the microcomplex, which is a conglomerate of several parasagittally aligned microzones (Figure 2C,D) (Cerminara et al., 2015). Each microzone in the microcomplex is connected to the same defined area in the inferior olive and the deep cerebellar nuclei, and comprise cellular circuits formed in the order of 1,000 Purkinje cells and the associated cells (D'Angelo et al., 2016). The cellular circuitry is for the most part identical throughout the cerebellar cortex and contains a specific set of neuronal cells and glial cells, except for the flocculonodular lobe, which contains an additional neuronal cell type, the unipolar brush cell (Mugnaini et al., 2011).

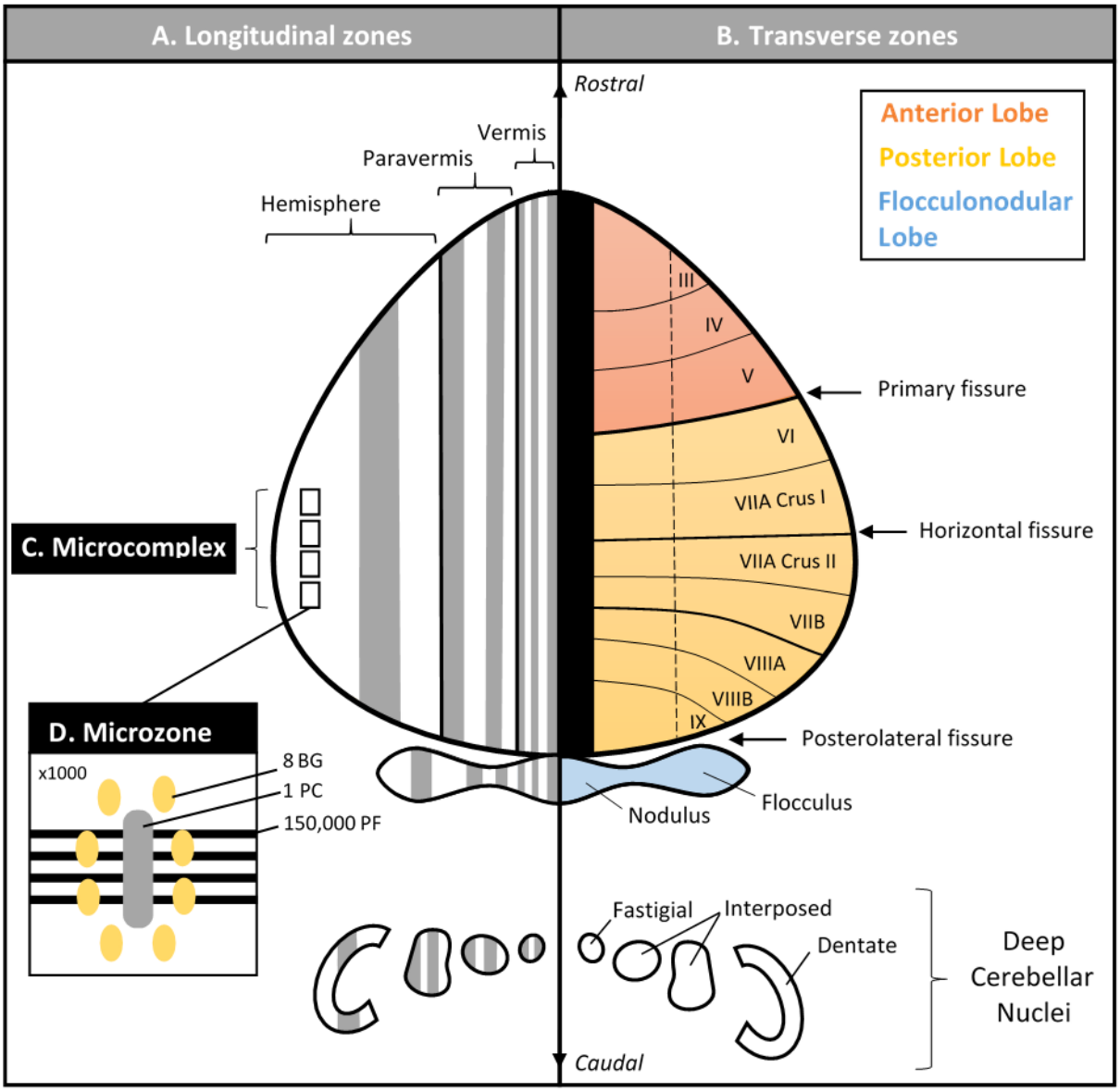


***Figure 2.*** *The cerebellar zones. A) Longitudinal zones. B) Transverse zones. C) Microcomplex, consisting of several parasagittally oriented microzones. D) Microzone, depicting the spatial orientation of three of the main cells in the cerebellar cortex. Each microzone consists in the order of 1,000 Purkinje cells (PC) and the associated cells. For each PC in the microzone there are approximately eight Bergmann glial cells (BG). Every PC receives excitatory input from approximately 150,000 parallel fibers (PF).*

### 2.1.3 Cellular circuitry

The cerebellar cortex can be divided into three cellular layers from the innermost to the outermost: the granular layer, Purkinje cell layer, and molecular layer (Figure 3) (D'Angelo & Casali, 2013). An incoming input is first processed in the granular layer. The granular layer is populated by small but numerous granule cells as well as Golgi cells. The granular layer is compartmentalized into glomeruli, each comprised of multiple granule cells, Golgi cells, and

mossy fiber afferents. The granule cells project long axons through the Purkinje cell layer into the molecular layer, where they bifurcate into T-shaped structures known as the parallel fibers. Purkinje cell somata are located in the Purkinje cell layer, and the dendritic tree in the molecular layer. The parallel fibers run across the molecular layer perpendicular to the flat-shaped dendritic trees of the Purkinje cells and make contacts with multiple Purkinje cells and molecular layer interneurons; stellate cells and basket cells. Each Purkinje cell receives excitatory input from two different sources: over 150,000 different parallel fibers and a single climbing fiber (D'Angelo et al., 2016). In addition, the Purkinje cells receive inhibitory input from the molecular layer interneurons. Purkinje cell is the sole output neuron of the cerebellar cortex, and the deep cerebellar nuclei the sole output of the cerebellum as a whole. The deep cerebellar nuclei receive inhibitory inputs from the Purkinje cells as well excitatory inputs from the climbing fibers and mossy fibers.

In addition to the neuronal cells, the cerebellum contains multiple different types of glial cells. The cerebellar glial cells can be divided into three main categories: microglia, oligodendrocytes, and astrocytes (Palay & Chan-Palay, 1974). The cerebellar astrocytes are located in defined territories within the cell layers and the white matter, whereas the distribution of the oligodendrocytes and the microglia is more universal across the cerebellar cortex (Araujo et al., 2019). The following chapters will concentrate on the properties of the cerebellar astrocytes, with a focus on the single-cell properties of the most well-known cerebellar astrocyte, the Bergmann glia.

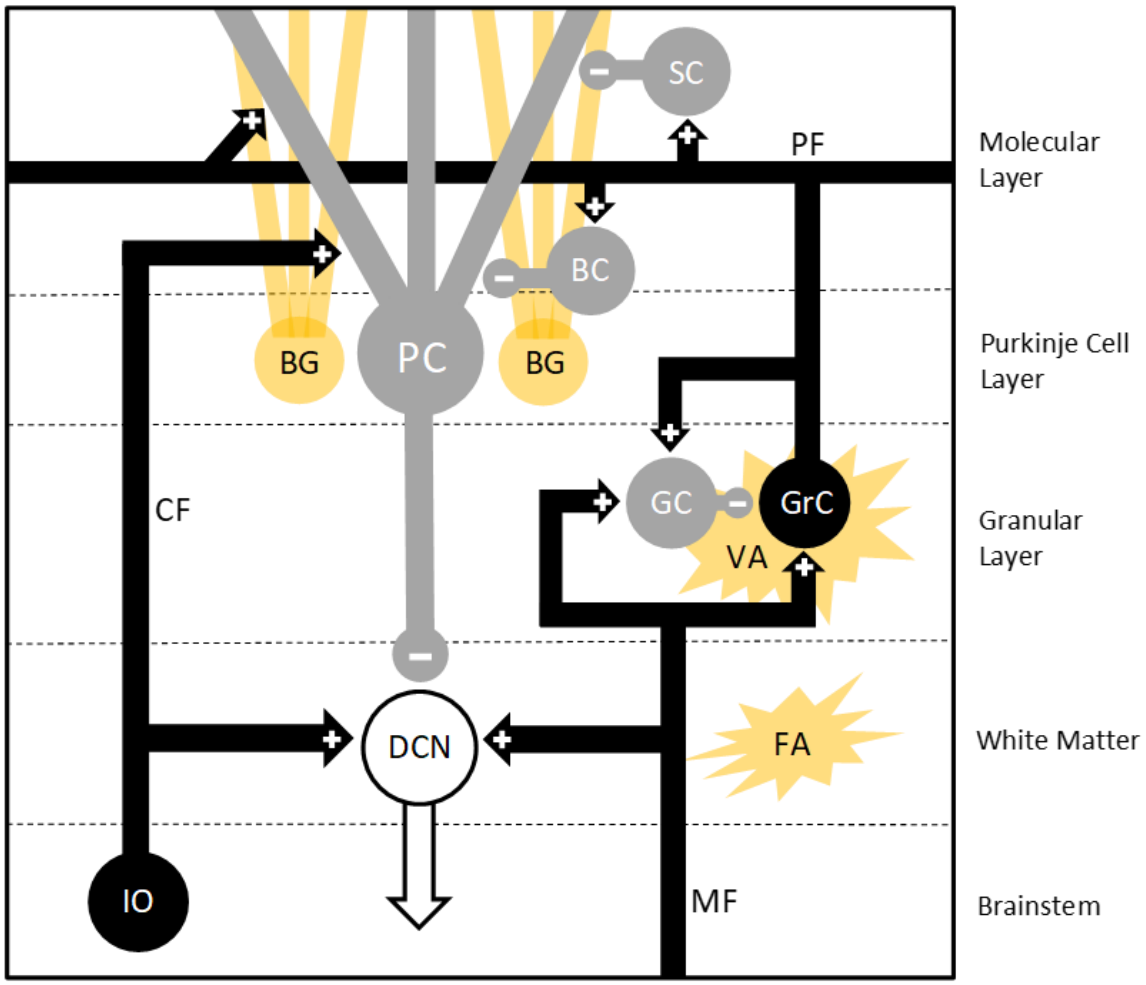


***Figure 3.*** *The cerebellar circuitry, showcasing the main types of cerebellar astrocytes, inhibitory (gray) and excitatory (black) neurons, and the deep cerebellar nuclei (DCN). BC, basket cell; BG, Bergmann glia; CF, climbing fiber; DCN, deep cerebellar nuclei; FA, fibrous astrocyte; GC, Golgi cell; GrC, granule cell; IO, inferior olive; MF, mossy fiber; PC, Purkinje cell; PF, parallel fiber; SC, stellate cell; VA, velate astrocyte.*

## 2.2 Cerebellar astroglia

### 2.2.1 Classification

Multiple different types of astroglial cells, also known as astrocytes, are found throughout the central nervous system. Verkhratsky and Nedergaard (2018) define astrocytes as cells that originate from the neuroepithelium and that have any kind of a homeostatic role in the central nervous system (CNS). This classification excludes the microglia, that are of myeloid origin, and the oligodendrocytes whose main function is myelination. Classically, astrocytes are described as star-shaped cells: “astro” means “star” and “cyte” means cell. Many of the cells classified as astrocytes differ from the “classical” star-like astrocyte morphology. The

cerebellar astrocytes are divided into protoplasmic astrocytes of the cortex and fibrous astrocytes of the white matter (Araujo et al., 2019). The protoplasmic astrocytes include velate astrocytes that are rounded in shape, and Bergmann glial cells, a subtype of radial astrocytes. Bergmann glial cells are one of the few radial glial cells present in mature brain. During their development, they acquire characteristics of astrocytes but retain many stem-cell related properties (Koirala & Corfas, 2010). One other type of cerebellar astroglial cell, denoted as the Fañanas cell after its finder (Fañanas, 1916), is described as a subtype of short Bergmann glial cell (Reichenbach & Wolburg, 2013). In contrast to Bergmann glial cells, Fañanas cells have smaller cell bodies located higher in the cerebellar cortex and lack the pial processes (Goertzen & Veh, 2018). Fañanas cells express two astrocytic marker proteins, the potassium ($K^+$) channel-related polypeptides $K_v2.2$ and calsenilin, but not the main astrocytic marker glial fibrillary acidic protein (GFAP) characteristic of Bergmann glial cells (Goertzen & Veh, 2018). Apart from this, very little is known about the Fañanas cells.

The Bergmann glial radial processes in cat, dog, and human cerebella were first described by Karl Bergmann in 1857. Later Camillo Golgi (1885) found out that the radial processes comprised of glial elements. The name “Golgi epithelial cell”, that has been sometimes interchangeably used to denote Bergmann glia, was termed by Ramon y Cajal (1911). Palay & Chan-Palay (1972) introduced the term velate astrocyte, and designated both Bergmann glia and velate astrocytes under this term as variations of the same cell type. For such close located astroglia, velate astrocytes and Bergmann glia are exceptionally differentiated both in form and function (Verkhratsky & Nedergaard, 2018). As highly plastic cells, however, the morphology and function of cerebellar astroglial cells is liable to their environment. Under a certain morphogen, velate astrocytes have been shown to take on the identity of Bergmann glial cells (Farmer et al., 2016).

### 2.2.2 Location and interactions

Bergmann glial somata are located in the Purkinje cell layer with approximately eight of them surrounding a single Purkinje cell (Reichenbach et al., 1995). The somata give rise to the Bergmann fibers that extend across the molecular layer and terminate as endfeet at the pial surface or blood vessels (Chan-Palay & Palay, 1972). The plane of Bergmann fibers is perpendicular to the dendrites of Purkinje cells and parallel to the long axis of the cerebellum (Kettenmann & Ransom, 2013). The columns formed by Bergmann fibers are flatter perpendicular to parallel fibers, but not as flat as the dendritic trees of Purkinje cells.

Neighboring Bergmann fibers overlap and form so-called palisades. The spacing of Bergmann glial cells is slightly wider in rostro-caudal axis than along the direction of parallel fibers, where intervals of a few μm separate the adjacent cells. (De Blas, 1984; Hoogland & Kuhn, 2010; Reichenbach et al., 1995). Velate astrocytes are located in the granular layer, where they form glial sheaths that compartmentalize the granule layer neurons into glomeruli, thus effectively grouping the sensory information conveyed by the mossy fibers (Palay & Chan-Palay, 1974). The velate processes constitute an elaborate network where distinguishing individual cells is difficult (Palay & Chan-Palay, 1974). The endfeet of velate astrocytes contact blood vessels, either by coiling around the vessels or simply abutting against them (Palay & Chan-Palay, 1974). Fibrous astrocytes reside in the white matter and with their long fibrous processes contact blood vessels and the nodes of Ranvier, the myelin-free spots along the neuronal axons (Sofroniew & Vinters, 2010).

The cerebellar cortex is packed with neuronal and glial cells. In the cerebellar molecular layer, only about 0.12% of the tissue volume is taken by the extracellular fluid (Nicholson & Syková, 1998). Approximately half of the extracellular space in the molecular layer is enclosed between one astroglial cell and one nonastroglial membrane (Lehre & Danbolt, 1998). While astrocytes usually occupy distinct, non-overlapping regions, the processes of separate Bergmann glial cells are often intermingled (Grosche et al., 2002). The tissue-volume fraction of Bergmann glia in the molecular layer is about 20-30% (Barros et al., 2009), and the tissue-volume fraction of one Bergmann glial cell about 17.5% (Grosche et al., 2002). Near parallel fiber to Purkinje cell synapses, Bergmann glia occupy ~32% of the tissue volume (Lehre & Rusakov, 2002). The mean surface density of Bergmann glial processes in the molecular layer is about 3.8 $\mu m^2/\mu m^3$ (Lehre & Danbolt, 1998). The mean surface density for processes originating from a single Bergmann glial cell is about half of that, around 1.89 $\mu m^2/\mu m^3$, indicating that processes from different Bergmann glial cells interdigitate in the tissue (Grosche et al., 2002). The estimated surface densities of Bergmann glial membranes contacting other Bergmann glial membranes or large dendrites are about 0.46 $\mu m^2/\mu m^3$ and 0.13 $\mu m^2/\mu m^3$, or 12% and 3% of the total Bergmann glial surface area, respectively (Lehre & Danbolt, 1998). The precise percentage of Bergmann glial membrane area apposing pia mater or blood vessels has not been calculated, but estimated to be in the orders of magnitude smaller (Lehre & Danbolt, 1998).

The cerebellar astrocytes acquire and maintain their distinct phenotypes via complex molecular pathways intertwined with those of cerebellar neuronal cells and sustained by reciprocal communication. The association between Bergmann glia and Purkinje cells with each other

enables the normal development of their distinct phenotypes, making their dependence of each other reciprocal (Farmer et al., 2016; Fisher et al., 1993). The development of Bergmann glia is tightly linked with that of Purkinje cells; likewise, that of velate astrocytes with the granule cells and mossy fibers. The distinct yet intersecting phenotypes and molecular profiles of Bergmann glia and velate astrocytes emerge through differentially regulated gene expression (Farmer et al., 2016). One of the main pathways involved in making this separation is the sonic hedgehog (Shh) morphogen that is secreted by mature Purkinje cells and maintains the identity of surrounding Bergmann glial cells. If exposed to the Shh morphogen, velate astrocytes develop the characteristics of Bergmann glia, including the transcriptome and electrophysiological properties (Farmer et al., 2016).

In contrast to velate astrocytes that predominantly isolate multiple neuronal synapse within a single glial sheath, Bergmann glial cells enwrap individual synapses. Bergmann glial processes ensheath the Purkinje cells in their entirety: the Purkinje cell body, dendrites, and initial segment of axon are all covered (Muller & Kettenmann, 1995). The inhibitory and excitatory connections to Purkinje cell pierce through the sheath formed by Bergmann glia. The inhibitory molecular layer interneurons, basket and stellate cells, mainly target the Purkinje cell somata, and the excitatory parallel fibers and climbing fibers the Purkinje cell processes (Castejon et al., 1999). Bergmann glia may also make contact with the dendrites of Golgi cells and basket cells (Palay & Chan-Palay, 1974). Excluding the Purkinje cell and their synaptic clefts that are completely ensheathed, the cells of the molecular layer are covered only partially by Bergmann glia; the ensheathment of parallel fiber to Purkinje cell synapses is 3-4 folds higher postsynaptically than presynaptically (Grosche et al., 2002; Lehre & Rusakov, 2002; Palay & Chan-Palay, 1974). While the parallel fiber to Purkinje cell synapses are around 65-69% covered by Bergmann glial cells, the coverage of climbing fiber to Purkinje cell synapses is about 87%, making the latter especially shielded from synaptic cross-talk and glutamate spillover (Grosche et al., 1999; Lehre & Rusakov, 2002; Xu-Friedman et al., 2001). The coverage of individual mossy fiber to granule neuron synapses by velate astrocytes is only around 15%, as most of the synapses are agglomerated within glomeruli (Mitchell & Silver, 2000; Sylantyev et al., 2013). In the rat cerebellum, each Bergmann glial cell process ensheaths more than 500-1,000 Purkinje cell synapses and a single Bergmann glial cell with 4-5 processes 2,000-6,000 synapses (Reichenbach et al., 1995). Eight Bergmann glial cells are therefore able to provide coverage for the total of 17,000–51,500 dendritic spine synapses of a single Purkinje cell (Reichenbach et al., 1995).

Besides neuronal ensheathment and endfeet connections to pia mater and blood vessels, cerebellar astroglial cells are linked with each other. Through numerous gap junctions distributed across their distal processes, cerebellar astroglial cells share their cytoplasm into a syncytia of connected cells. Conversely to the orientation of the Bergmann glial palisades, gap junctions couple Bergmann glial cells electrically into rows perpendicular to parallel fibers (Verkhratsky & Reichenbach, 2009). A longitudinally cut Bergmann glial process of length 35 μm with two major branches contained 11 gap junctions, located 10-30 μm distal to the soma (Müller et al., 1996). Somata and wide initial segments of processes usually do not have gap junctions; only in one cell a singular small gap junction was found on the soma and the initial segment of process (Müller et al., 1996). Majority of the gap junctions were less than 100 nm wide (Müller et al., 1996). Velate astrocytes form gap junctions with nine neighboring cells in average (Hoogland & Kuhn, 2010; Kiyoshi et al., 2018). Fibrous astrocytes form gap junctions via their distal processes with other fibrous astrocytes (Sofroniew & Vinters, 2010). In addition to coupling with other astrocytes via gap junctions, astrocytes may form gap junctional connections with neuronal cells. In the rat cerebellum, Bergmann glia and Purkinje cells were electrically coupled via gap junctions (Pakhotin & Verkhratsky, 2005).

### 2.2.3 Developmental stages

Bergmann glia development in mice consists of four stages: radial glia (E14), migration (E14–P7), transformation (P7-P21), and protoplasmic astrocyte (P21-) (Yamada & Watanabe, 2002). Comparison of Bergmann glia in different stages of development revealed differences in morphology and in voltage-gated $K^+$ currents (Muller et al., 1994). The mature Bergmann glia had more protrusions, whereas younger ones were smoother and thinner in appearance. In addition to the more arborized morphology, density and length of the processes increased with age (Lippman et al., 2008). The voltage-gated currents, including the outward- and inward-rectifying $K^+$ currents, were recorded only from younger animals. In contrast, $K^+$ currents in older animals were large and independent of time and voltage (Muller et al., 1994). The extent of gap junctional coupling increases during development; early postnatal cells are not yet coupled whereas later stage cells are (Müller et al., 1996).

Aging-related changes affect different parts of the brain differently, the cerebellum being the region with most neuronal death (Boisvert et al., 2018). In accordance with the aging-related Purkinje cell death observed in the cerebellum, most aging-related changes in astroglial gene expression have been demonstrated to occur in the cerebellar astrocytes, including Bergmann

glia (Boisvert et al., 2018). The causal relationships between the changes in the astroglial gene expression and the Purkinje cell death remains to be elucidated.

### 2.2.4 Evolutionary changes

The basic morphology of Bergmann glia is similar in all vertebrates, with differences only in length and the extent of branching (Siegel et al., 1991). As the length of the Bergmann glia is determined by the depth of the molecular layer that it occupies, its length is linked to the size of the animal. Comparison of morphologies from different species (mouse, rat, monkey, and human) showed considerable differences in length and the fractal dimension (Siegel et al., 1991). The fractal dimension is a quantitative measure of complexity, corresponding to the abundance of protrusions from the Bergmann glial main fibers. The smaller animals had shorter Bergmann glial cells and higher fractal dimension. In contrast, the larger species had longer Bergmann glial cells with lower fractal dimension.

In addition to differences between species, sex-related differences may exist between male and female astrocytes (Verkhratsky & Nedergaard, 2018). In the cerebellum, the Bergmann glial immunoreactivity for GFAP was higher in males in comparison to females that had a higher immunoreactivity for vimentin (Suárez et al., 1992).

## 2.3 Single-cell morphology

The Bergmann glial stem tree consists of soma and several main processes that are connected to the pia mater, other Bergmann glial cells, and neuronal synapses via specialized structures (Figure 4). The main processes give rise to lateral processes in three levels of complexity: a nanodomain, a microdomain, and multiple microdomains connected to each other in a single lateral appendage. The lateral processes contain small membrane outgrowths, peripheral astrocytic processes (PAPs), that ensheath neuronal synapses and join together adjacent Bergmann glial cells via gap junctions. The main processes terminate as endfeet to form the glia limitans.

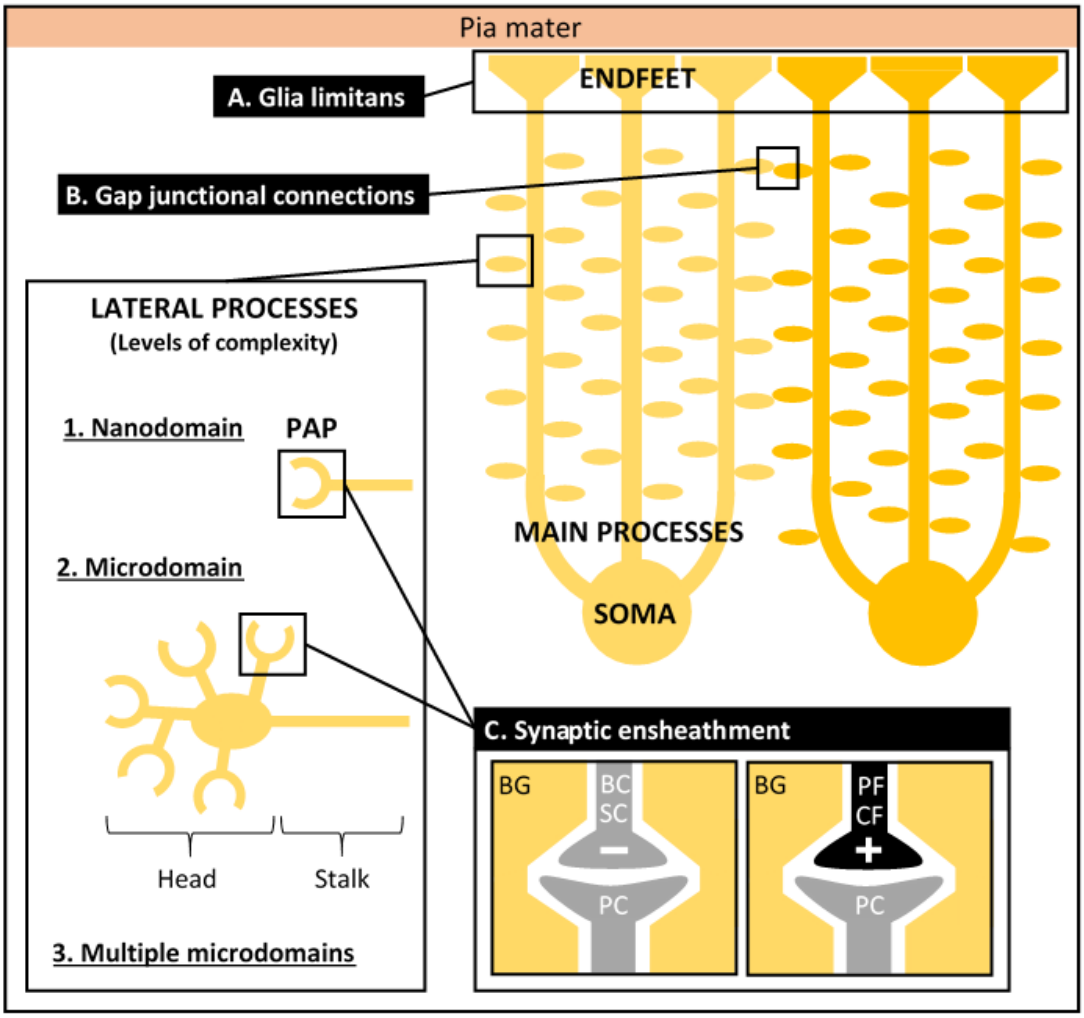


***Figure 4.*** *Morphology of a Bergmann glial cell and its specialized structures that connect it to the pia mater, other Bergmann glial cells, and neuronal synapses (A-C). Abbreviations: BG, Bergmann glia; BC, basket cell; CF, climbing fiber; PAP, peripheral astrocytic process; PC, Purkinje cell; PF, parallel fiber; SC, stellate cell.*

### 2.3.1 Whole cell

An adult rat Bergmann glial cell has a volume of about 3,600 μm$^3$ (Reichenbach et al., 1995). Velate astrocytes are approximately the same size as granule cells or slightly larger (Palay & Chan-Palay, 1974).

### 2.3.2 Soma

A mouse Bergmann glial soma is approximately 8.5 μm in diameter (Muller et al., 1994). In rats, the soma is slightly larger, about 10 μm in diameter (Bergles et al., 1997). The Bergmann glial soma is not completely spherical, but elongated in the longitudinal direction (Rakic, 1971).

### 2.3.3 Main processes

About 2-6 fibers or stem processes arise from the Bergmann glial soma and traverse across the molecular layer (Muller & Kettenmann, 1995). The fibers are not completely straight, instead, they are often twisted and sometimes folded, and uneven in thickness (Rakic, 1971). The fibers are not completely cylindrical, either; they are ellipsoidal with the longer diameter facing the same direction as the parallel fibers (Rakic, 1971). In the 3-4-week-old mouse cerebellum, the area encompassed by the fibers of a single Bergmann glial cell was 40±10 μm in the transverse direction and 19±3 μm longitudinally (Hoogland et al., 2009). The surface to volume ratio of the main processes (excluding the lateral processes) is about 4.15 $\mu m^{-1}$ (Grosche et al., 1999). The stem processes have an electronlucent cytoplasm that is packed with longitudinal bundles of microtubules and microfilaments, with diameters of around 200 Å and 80-90 Å, respectively (Rakic, 1971). Alongside the filaments runs tubular elements of the endoplasmic reticulum, sprinklings of glycogen particles, and a single elongated, thin mitochondrion of 5-10 μm in length (Palay & Chan-Palay, 1974).

The length of the Bergmann glial stem processes differs widely depending on which vertebrate cerebellum they are located in, as larger animals have thicker molecular layers that the fibers must traverse. The average lengths in 2-year-old mouse, 1-year-old rat, 7-year-old monkey, and 62-64-year-old human were 80 μm, 165 μm, 250 μm, and 328 μm, respectively (Siegel et al., 1991). Likewise, the length of the processes increases as the animal matures. The average length of the processes in rats aged between 16 days and two years ranged from 140 μm to 195 μm (Hanke & Reichenbach, 1987). Within this same age window in rats, the absolute length covered by lateral processes also increased as the animal matured, from 42 μm to 96 μm of a main process covered (Hanke & Reichenbach, 1987). The relative coverage by the lateral processes in rats of different ages from 16 days, 30 days, 5 months, 1 year, to 2 years changed from 39 %, 49 %, 63 %, 58 %, to 53 % (Hanke & Reichenbach, 1987). In contrast to the fiber lengths, the fiber diameters of Bergmann glia are in roughly similar caliber in different animals. The average diameters in 2-year-old mouse, 1-year-old rat, 7-year-old monkey, and 62-64-year-old human were 0.7 μm, 0.79 μm, 1.2 μm, and 0.96 μm, respectively (Siegel et al., 1991). The diameter tends to shrink somewhat as the animal matures and the processes elongate. The average diameters of the processes in rats aged 16 days, 30 days, 5 months, 1 year, and 2 years were 0.77 μm, 0.68 μm, 0.81 μm, 0.66 μm, and 0.63 μm, respectively (Hanke & Reichenbach, 1987).

### 2.3.4 Lateral processes

The main processes of cerebellar astrocytes give rise to highly heterogeneous lateral processes (Chan-Palay & Palay, 1972; Rakic, 1971). The lateral processes consist of a single peripheral astrocytic processes (PAP) or a cluster of PAPs whose principal function is to ensheath neuronal synapses. PAPs are thin membrane folds of finger-like or lamellar shapes that lack most cytoplasmic organelles, including the endoplasmic reticulum (ER). They are dynamic small lamellipodia or filopodia whose structural changes are dependent on the reorganization of their actin cytoskeleton (Schiweck et al., 2018). While most of the PAPs are associated with synapses, PAPs known as glial thimbles are associated with non-synaptic neuronal structures that might be growing synapses or relics of dying ones (Grosche et al., 1999). In contrast to perisynaptic Bergmann glial PAPs that ensheath Purkinje cell excrescences but leave room for the presynaptic neuron to form the synaptic connection, glial thimbles enwrap the Purkinje cell excrescences completely (Grosche et al., 1999).

The functional domains formed by PAPs can be classified by magnitude into three levels: nanodomains, microdomains, and glomeruli (Grosche et al., 1999; Reichenbach & Wolburg, 2009). Nanodomains are singular PAPs that ensheath one synapse, microdomains a cluster of PAPs that ensheath on average about five synapses, and glomeruli a hollow compartment formed by multiple PAPs that do not directly contact the synapses they ensheath within this structure. Bergmann glia forms both nanodomains and microdomains; velate astrocytes form the glomeruli. The fibrous astrocytes also form PAPs, however, they do not ensheath synapses but the neuronal axons that traverse the white matter (Sofroniew & Vinters, 2010). The PAPs of Bergmann glia and velate astrocytes are highly heterogeneous and appear as thin and involuted lamellae (Palay & Chan-Palay, 1974). Bergmann glial PAPs are drumstick-shaped protrusions 1-2 μm long that terminate as cup-like formations that enwrap the spines of Purkinje cell dendrites. If cut transversely, the expansions are observed to radiate in all directions from the stalk or stem process. Several expansions are often located close to each other on ribbon-like stalk, in a resemblance of a chimney-brush (Rakic, 1971). Grosche et al. (1999) distinguished two classes: abundant tiny lamellar or thorn-like PAPs, and large branching structures of complex shapes, the microdomains.

Microdomains were first described in Bergmann glial cells (Grosche et al., 1999) and later also computationally modeled (Grosche et al., 2002). Microdomains are the smallest unit of Bergmann glial lateral processes excluding the finger-like PAPs or glial thimbles. A single

microdomain consists of a thin stalk that projects from the stem fiber more or less orthogonally, and a rounded head structure that hosts one or several PAPs. The stalks were nearly cylindrical with diameter around 0.1-0.3 μm and length of up to 7 μm or more. The surface areas and volumes were 5.4 $\mu m^2$ and 0.37 $\mu m^3$ for the stalk, and 316.9 $\mu m^2$ and 16.1 $\mu m^3$ for the head, respectively. Stimulation of parallel fibers resulted in $Ca^{2+}$ rises in individual microdomains. In addition, the computational simulation indicated that depolarization, induced for example by glutamate, does not spread via the stalk to neighboring microdomains or the stem process. Microdomains thus seem to be electronically isolated and capable of interacting autonomously with the clusters of synapses that they ensheath. The electrical independence of microdomains is supported by the metabolic independence provided by one or more mitochondria that they contain. (Grosche et al., 1999, 2002) The thicker parts of microdomains may also contain fascicles of neuroglial filaments and particles of glycogen (Palay & Chan-Palay, 1974).

Microdomains are the repetitive unit of the Bergmann glial cell attached either directly onto stem processes or to another microdomain. A single Bergmann glial cell might have hundreds of microdomains in total (Grosche et al., 1999). The estimated tissue-volume fraction of one microdomain is about 1/12 or 8.3% (Grosche et al., 2002). As the tissue-volume fraction of one Bergmann glial cell is about 1/6 or 17.5%, around half of the Bergmann glial volume within this volume fraction must thus be contributed by microdomains (Grosche et al., 2002). The surface-to-volume ratio of lateral processes is on average about 13-15 $\mu m^{-1}$ and up to 25 $\mu m^{-1}$ for appendages with very high complexity, and in total, the head structures can constitute nearly 90% of the cell surface area (Grosche et al., 1999).

Lippman et al. (2008) categorized and determined the frequency of four lateral process subtypes: stubby, thin, branching, and bulbous along the length of the stem processes. Stubby and thin processes are nanodomains, and branching and bulbous processes are microdomains or several microdomains attached to each other or thicker lateral processes. Stubby processes are under 2 μm long and thin between 2 μm and 10 μm. Stubby processes are defined to be under 2 μm long, whereas thin processes are between 2-10 μm. Branching corresponds to a process that splits more than once while still being under 10 μm and bulbous is described as having a rounded reticular head connected by a small neck. The subtypes did not include lateral processes longer than 10 μm or shapes otherwise unclassifiable to the above categories. In Bergmann glia of 14-day-old mice, the frequency of the lateral process subtypes along 10 μm of stem process were in average 1.8, 0.24, 0.23, and 0.5 for the stubby, thin, branching, and

bulbous subtypes, respectively. In 20-day-old mice, the values for the same subtypes were 1.49, 0.36, 0.4, and 1.25, respectively. As expected, the number of the stubby processes decreased and the number of the larger lateral processes increased, corresponding to the increased ensheathment of neuronal synapses.

### 2.3.5 Endfeet

The Bergmann glial stem processes terminate as endfeet at surface of the pia mater and connect to each other via gap junctions to form the glia limitans (Palay & Chan-Palay, 1974). The endfeet can also be found surrounding large blood vessels. Palay & Chan-Palay (1974) described two types of Bergmann glial endfeet: shapeless clumps that are flattened against the pia mater, and bulbous tips that abut against the pia mater or blood vessels. The first type exhibits various forms, including leaf-like plasmalemmal folds reminiscent of PAPs and larger structures containing organelles. The leaf-like endfeet may join into overlapping laminae to form the glia limitans. The second type is button-like structure containing whorls of endoplasmic membrane and one or two mitochondria. They are often arranged in rows and the two types may be interspersed. The distinction between the two types is not definite, and many intermediate forms may be exhibited by the highly polymorphic and dynamic endfeet. (Palay & Chan-Palay, 1974) The average diameter of the endfeet in 13-19-day-old rats was about 5 μm (Beierlein & Regehr, 2006), and slightly smaller in 26-day-old mice, about 4 μm (Saab et al., 2012).

## 2.4 Membrane proteins

Cerebellar astrocytes express a wide assortment of membrane proteins. The distribution and function of the membrane proteins vary across different types of astrocytes as well as within the astrocyte's specialized structures. Soma, endfeet, processes, and PAPs have different concentrations of different membrane proteins relevant to their function. Knowledge on the physiology and localization of membrane proteins is essential for realistic single-cell modeling. The following tables list the membrane proteins that are found on cerebellar astrocytes, including Bergmann glia, velate astrocytes, and fibrous astrocytes. In addition, the membrane proteins that are expressed highly at P6 and/or P30 in Bergmann glial cells according to the genetic study by Koirala and Corfas (2010) are included.

### 2.4.1 Channels

Ion channels are integral membrane proteins that form aqueous pores for the selective transfer of water-soluble ions, regulated by environment-sensitive gating mechanisms that define the kinetics of the channels closing and opening (Verkhratsky & Parpura, 2015). Ion channels can be classified based on either their ion selectivity, gating mechanism, topology, number of transmembrane domains per subunit, or by historical nomenclature such as large and long-lasting (L-type) $Ca^{2+}$ channels. The channels expressed in cerebellar astroglial cells include $K^+$ channels, sodium ($Na^+$) channels, $Ca^{2+}$ channels, anion channels, water channels, and gap junctional channels (Table 1).

### 2.4.2 Ionotropic receptors

Ionotropic receptors are ligand-gated ion channels that are opened by neurotransmitter binding and allow the passage of different ions, producing diverse dynamical effects on cell membrane potential and ion concentrations (Verkhratsky & Parpura, 2015). Astroglial cells express all of the three topologically distinct types of ionotropic channels known as trimeric adenosine triphosphate (ATP) purinoceptors, tetrameric glutamate receptors, and pentameric receptors. The ionotropic receptors expressed in Bergmann glia include purinoceptor $P2X_7$, glutamate receptors α-amino-3-hydroxy-5-methyl-4-isoxazolepropionic acid receptor (AMPAR) and N-methyl-D-aspartate receptor (NMDAR), and γ-aminobutyric acid (GABA) type A receptor ($GABA_AR$) (Table 2). Purinoceptors and glutamate receptors translocate $Ca^{2+}$ and $Na^+$ ions into the cell and $K^+$ ions out, GABA receptors translocate $Ca^{2+}$, $Cl^-$, and $Na^+$ ions in and $Cl^-$ and $K^+$ ions out.

***Table 1.*** *Channels in cerebellar astroglial cells*

| Channel | Animal & age | Preparation & cell type | Technique | Localization | References |
|---|---|---|---|---|---|
| **POTASSIUM CHANNELS** | | | | | |
| $K_{ir}2.2$ | Rat, adult | Slice, BG, VA | IHC | Processes | (Leonoudakis et al., 2001) |
| $K_{ir}4.1$ | Rat, adult | Slice, BG | ISH | Processes close to the primary branches of PCs | (Poopalasundaram et al., 2000) |
| | Mouse, P49-365 | Slice, BG | IHC | Endfeet that contact the pia mater | (Hirrlinger et al., 2008) |
| | Mouse, P7–11 | Slice, BG, FA, VA | IHC, IP, WB | High expression in processes | (Brasko et al., 2017) |
| $K_{ir}5.1$ | Mouse, P7–11 | Slice, VA | IHC, IP, WB | Soma and processes | (Brasko et al., 2017) |
| $K_{ir}6.1$ | Rat, adult Mouse, P14 | Slice, BG | IHC (rat), WCPC (mouse) | Peridendritic and perisynaptic processes | (Thomzig et al., 2001) |
| $K_{ir}6.2$ | Rat, P28-56 | Slice, BG, FA | IHC, ISH | ER, Golgi apparatus and plasma membrane | (M. Zhou et al., 2002) |
| $K_{dr}1.5$ | Rat, adult | Slice, BG | IHC | Processes and endfeet | (Roy et al., 1996) |
| $K_{Ca}1.1$ | Rat, 1 month | Slice, CA | IHC | Perivascular endfeet | (Price et al., 2002) |
| **CALCIUM CHANNELS** | | | | | |
| $IP_3R2$ | Rat, adult | Slice, BG, FA, VA | IHC | Soma and perisynaptic processes | (Holtzclaw et al., 2002) |
| | Mouse, P13-15 | Slice, BG | $Ca^{2+}$ imaging, IHC | Processes | (Tamamushi et al., 2012) |
| SOCE channel | Rat, P8-15 | Slice, BG | $Ca^{2+}$ imaging | | (Singaravelu et al. 2006) |
| RYR3 | Mouse, P14 | Primary culture, CA | RT-PCR | Expressed | (Matyash et al., 2001) |
| **SODIUM CHANNELS** | | | | | |
| $Na_v1.6$ | Rodent, N/D | Slice, BG | IHC, ISH | Processes, mostly in the lower regions of the ML | (Schaller & Caldwell, 2003) |
| **ANION CHANNELS** | | | | | |
| Best-1 | Mouse, adult | Slice, BG | IHC, WCPC | Processes | (Lee et al., 2010) |
| | Mouse, 8–10 wk | Slice, BG | IHC, WCPC | | (Yoon et al., 2014) |
| | Mouse, 5-10 wk | Slice, BG | ICC | No expression in processes | (Ormel et al., 2020) |
| CLC-2 | Mouse, P35 | Slice, BG | IHC | Expressed | (Blanz et al., 2007) |
| CLC-3 | Mouse, P30 | Isolated cells, BG | Single-Cell RT-PCR | Highly expressed | (Koirala & Corfas, 2010) |
| CLC-4 | Mouse, P6 & P30 | | | | |
| VRAC | Mouse, P30 | | | | |
| **CONNEXONS** | | | | | |
| Cx43 | Mouse, P5-7, P20-24 | Slice, BG | EM, WCPC | Distal parts of the processes | (Müller et al., 1996) |
| | Mouse, 3.5 months | Slice, BG | IHC | Processes | (Tanaka et al., 2008) |
| **WATER CHANNELS** | | | | | |
| AQP4 | Mouse, P49-365 | Slice, BG, VA | IHC | Endfeet contacting the pia mater and capillaries | (Hirrlinger et al., 2008) |

Abbreviations: AQP4, aquaporin-4; Best-1, Bestrophin-1; BG, Bergmann glia; CA, cerebellar astrocyte; $Ca^{2+}$, calcium; CLC, chloride channel; Cx43, connexin 43; EM, electron microscopy; ER, endoplasmic reticulum; FA, fibrous astrocyte; ICC, immunocytochemistry; IHC, immunohistochemistry; IP, immunoprecipitation; $IP_3R2$, inositol 1,4,5-trisphosphate receptor 2; ISH, *in situ* hybridization; $K_{Ca}$, calcium-dependent potassium channel; $K_{dr}$, delayed rectifying potassium channel; $K_{ir}$, inwardly rectifying potassium channel; ML, molecular layer; $Na_v1.6$, voltage-gated sodium channel 1.6; N/D, not defined; P, postnatal day; PC, Purkinje cell; RT-PCR, reverse transcription polymerase chain reaction; RYR3, ryanodine receptor 3; SOCE, store-operated calcium entry; VA, velate astrocyte; VRAC, volume-regulated anion channel; WB, western blot; WCPC, whole-cell patch-clamp; wk, week.

***Table 2.*** *Ionotropic receptors in cerebellar astroglial cells*

| Agonist | Type | Animal & age | Preparation & cell type | Technique | Localization | References |
|---|---|---|---|---|---|---|
| Purines | $P2X_7$ | Mouse, 2–4 months | Slice, BG | $Ca^{2+}$ imaging, IHC, WCPC | Processes | (Habbas et al., 2011) |
| | | Mouse, P4-5 | Primary culture, CA | $Ca^{2+}$ imaging, ICC, WCPC | Processes | (Salas et al., 2013) |
| Glutamate | AMPAR | Rat, adult | Slice, BG, FA, VA | ICC | BG processes. No staining in VA or FA. | (Blackstone et al., 1992) |
| | | Rat, N/D | Slice, BG | ICC | Processes near PC dendrites & spines, axon terminals of PF/CF | (Baude et al., 1994) |
| | | Rat, P20-24 | Slice, BG | IHC, WCPC | Soma, processes | (Iino et al., 2001) |
| | | Rat, E19-P30 | Slice, BG | ICC | Soma, perisynaptic processes at PF/CF to PC synapses | (Douyard et al., 2007) |
| | NMDAR | Rat, N/D | Slice, BG | ISH | Subunits GluN1 and GluN2B expressed | (Luque & Richards, 1995) |
| | | Mouse & rat, adult | Slice, BG | IHC | Soma and processes. Subunits GluN1 and GluN2A expressed. | (Thompson et al., 2000) |
| GABA | $GABA_AR$ | Mouse, P5-30 | Slice, BG | IHC, WCPC | Processes of immature cells, downregulated in mature cells | (Muller et al., 1994) |
| | | Rat, P35-P70 | Slice, BG | ICC, IGS | Processes near inhibitory synapses. Some $GABA_ARs$ near excitatory synapses. | (Riquelme et al. 2002) |

Abbreviations: AMPAR, α-amino-3-hydroxy-5-methyl-4-isoxazolepropionic acid receptor; BG, Bergmann glia; CA, cerebellar astrocyte; $Ca^{2+}$, calcium; CF, climbing fiber; E, embryonic day; FA, fibrous astrocyte; GABA, γ-aminobutyric acid; $GABA_AR$, γ-aminobutyric acid type A receptor; ICC, immunocytochemistry; IGS,

immunogold staining; IHC, immunohistochemistry; ISH, *in situ* hybridization; N/D, not defined; NMDAR, N-methyl-D-aspartate receptor; $P2X_7$, purinergic adenosine triphosphate activated channel receptor subtype 7; P, postnatal day; PC, Purkinje cell; PF, parallel fiber; VA, velate astrocyte; WCPC, whole-cell patch-clamp.

### 2.4.3 Metabotropic receptors

Metabotropic receptors, characterized by seven transmembrane α-helices, employ a completely different signaling strategy than ionotropic receptors (Verkhratsky & Parpura, 2015). The representative class of metabotropic receptors, G-protein–coupled receptors (GPCRs), utilize G-proteins that are coupled with ion channels or enzymes that synthesize intracellular second messengers that in turn regulate a plethora of processes inside the cell. Examples of enzymes and their subjects include phospholipase C (PLC) that produces inositol trisphosphate ($IP_3$) which induces $Ca^{2+}$ release from ER, diacylglycerol (DAG) which activates protein kinase C (PKC), and adenylyl cyclase (AC) that synthesizes cyclic adenosine 3',5'-monophosphate (cAMP). Bergmann glial cells are equipped with a similar set of metabotropic receptors as Purkinje cells; including PLC/$IP_3$ cascade-mediating glutamate receptor (mGluR1/5) (Piet & Jahr, 2007), purine receptor (P2Y) (Habbas et al., 2011), noradrenaline receptor ($\alpha_1$AR) (Kulik et al., 1999), histamine receptor ($H_1$) (Kirischuk et al., 1996), and endothelin receptor ($ET_B$) (Tuschick et al., 1997). In addition, Bergmann glia express multiple other types of receptors for sensing their environment (Chrobak & Soltys, 2017).

### 2.4.4 Transporters

Transporters are pore-forming transmembrane proteins that can be classified into two main categories depending on the energy source they utilize for translocating their substrates: ATP-dependent transporters (also known as pumps) hydrolyze ATP, while the solute carrier transporters (SLCs) in general exploit the electrochemical gradients created by different ions (Verkhratsky & Parpura, 2015). The ATP-dependent transporters can be classified into ion pumps (further subdivided into P-type, F-type, and V-type) and ATP-binding cassette (ABC) transporters. The SLCs are either uniporters, transferring the substrate down its concentration gradient, or cotransporters that translocate the substrate against its concentration gradient by coupling the movement with another molecule that moves down its concentration gradient, in the same (symporter) or in the opposite direction (antiporter). The direction of transportation may change in some transporters depending on the membrane potential; the flux of $Na^+$ ions can be directed inside (forward mode) or outside (reverse mode).

ATP-dependent transporters in Bergmann glia include P-type pumps $Na^+/K^+$-ATPase (NKA), sarcoplasmic/endoplasmic reticulum $Ca^{2+}$ ATPase (SERCA), and plasma membrane $Ca^{2+}$-ATPase (PMCA). In addition, many members of F-type, V-type, and ATP-binding cassette transporters are expressed in Bergmann glia (Koirala & Corfas, 2010). NKA is expressed in high degree in Bergmann glia (Rose et al., 2009). SERCA2 is expressed in a very high degree, PMCA subtypes PMCA1 and PMCA2 to a lesser degree (Koirala & Corfas, 2010). NKA pumps two $K^+$ ions in and three $Na^+$ ions out. PMCA and SERCA pumps are involved in the maintenance of low cytosolic $Ca^{2+}$ concentration. PMCA pumps are located in the plasma membrane and pumps $Ca^{2+}$ ions out of the cells. SERCA is located in the endoplasmic reticulum (ER) membrane and pumps $Ca^{2+}$ ions into the ER lumen. In addition to the ATP-dependent transporters, Bergmann glia express many members of the SLC transporter family (Table 3).

## 2.5 Homeostatic and signaling mechanisms

The main membrane mechanisms present in different morphological structures of Bergmann glia are presented in the Figure 5. Velate astrocytes have the same morphological and connective structures as Bergmann glia, except that their PAPs form glomeruli instead of individual synaptic sheaths (Palay & Chan-Palay, 1974). The focus of this section are the astroglial mechanisms modulating the dynamics of $Ca^{2+}$, $K^+$, and glutamate in Bergmann glia.

The PAPs host the molecular machinery for sensing and regulating synaptic activity, including metabotropic receptors for neurotransmitters, channels and transporters for the uptake of $K^+$ ions, and ionotropic receptors and transporters for either excitatory neurotransmitter glutamate or the inhibitory neurotransmitter GABA (Verkhratsky & Nedergaard, 2018). In addition to sensing neurotransmitters, astrocytes can also release them as gliotransmitters to modulate the function of the synapses. Intracellular $Ca^{2+}$ increases can induce the release of gliotransmitters, such as glutamate, GABA, ATP, and D-serine (Verkhratsky & Parpura, 2015).

***Table 3.*** *SLC transporters in cerebellar astroglial cells*

| Type | Animal & age | Prepa-ration & cell type | Technique | Localization | References | Stoichiometry | |
|---|---|---|---|---|---|---|---|
| | | | | | | In | Out |
| EAAT1/ GLAST<br>EAAT2/ GLT-1 | Rat, N/D | Slice, BG, FA, VA | IGS, IHC | High expression in glial membranes close to nerve terminals, axons, and spines. Less expression close to capillaries, pia, or stem dendrites. GLAST high in BG, low in FA, and intermediate in VA. | (Chaudhry et al., 1995) | Glut $3Na^+$ $H^+$ | $K^+$ |
| | Rat, 7–8 weeks | Slice & primary culture, BG | WB | Membrane densities of GLAST and GLT-1 4700 and 740 $\mu m^{-2}$ | (Lehre & Danbolt, 1998) | | |
| VGLUT3 | Rat, P28-42 | Slice, BG | IGS, IHC | Radial processes | (Ormel et al., 2012) | | Glut |
| xCT | Chick, P18 | Slice, BG & VA | IHC | Soma, processes | (Suárez-Pozos et al., 2017) | Cys | Glut |
| GAT1 | Rat, young adult | Slice, BG & VA | IHC | Soma, processes | (Morara et al. 1996) | GABA $2Na^+$ $Cl^-$ | |
| GAT3 | Rat, adult | Slice, CA | IHC | Processes | (Minelli et al., 1996) | | |
| Asc-1 | Mouse, P6 & P30 | Isolated cells, BG | Single-Cell RT-PCR | Highly expressed | (Koirala & Corfas, 2010) | Gly | |
| GlyT1 | Rat, N/D | Slice, BG & VA | ICC | High expression in soma and processes | (Zafra et al., 1995) | Gly, $Cl^-$, $2Na^+$ | Gly, $Cl^-$, $2Na^+$ |
| | Mouse, P10-23 | Slice, BG | IHC, WCPC | | (Huang et al. 2004) | | |
| LAT1 | Mouse, P6 | Isolated cells, BG | Single-Cell RT-PCR | Highly expressed | (Koirala & Corfas, 2010) | DA, $½Na^+$, $Cl^-$ | |
| ASCT1 | Mouse, E13-18, P1-21, 2-3 months | Slice, BG | IHC, ISH | Soma, processes, and endfeet contacting the pia mater and capillaries | (Sakai et al., 2003) | D-Ser | $Na^+$ |
| VNUT | Mouse, P15 & adult | Slice, BG | IHC | Expressed both in P15 and adult | (Miras-Portugal et al., 2019) | | ATP |
| NCX | Mouse, P20-30 | Slice, BG | WCPC | Expressed | (Kirischuk et al., 1997) | $3Na^+$ | $Ca^{2+}$ |
| NKCC1 | Mouse, P5–100 | Slice, BG | FLIM, $Na^+$ imaging, WB | Soma, processes | (Untiet et al., 2017) | $Na^+$, $K^+$, $2Cl^-$ | |
| KCC1 | | | | | | $K^+$, $Cl^-$ | |

Abbreviations: Asc-1, Asc-type amino acid transporter 1; ASCT1, neutral amino acid transporter A; ATP, adenosine triphosphate; BG, Bergmann glia; CA, cerebellar astrocyte; $Ca^{2+}$, calcium; $Cl^-$, chloride; Cys, cystine; DA, dopamine; D-Ser, D-serine; E, postnatal day; EAAT, excitatory amino acid transporter; FA, fibrous astrocyte;

FLIM, fluorescence-lifetime imaging microscopy; GABA, γ-aminobutyric acid; GAT, γ-aminobutyric acid transporter; GLAST, glutamate aspartate transporter 1; Glut, glutamate; GLT-1, glutamate transporter 1; Gly, glycine; GlyT1, glycine transporter 1; $H^+$, hydrogen; ICC, immunocytochemistry; IGS, immunogold labeling; IHC, immunohistochemistry; ISH, *in situ* hybridization; $K^+$, potassium; KCC1, potassium-chloride cotransporter 1; LAT1, large neutral amino acid transporter 1; $Na^+$, sodium; NCX, sodium/calcium exchanger; N/D, not defined; NKCC1, sodium-potassium-chloride cotransporter 1; P, postnatal day; RT-PCR, reverse transcription polymerase chain reaction; VA, velate astrocyte; VGLUT3, vesicular glutamate transporter 3; VNUT, vesicular nucleotide transporter; WB, Western blot; WCPC, whole-cell patch-clamp; xCT, cystine/glutamate antiporter.

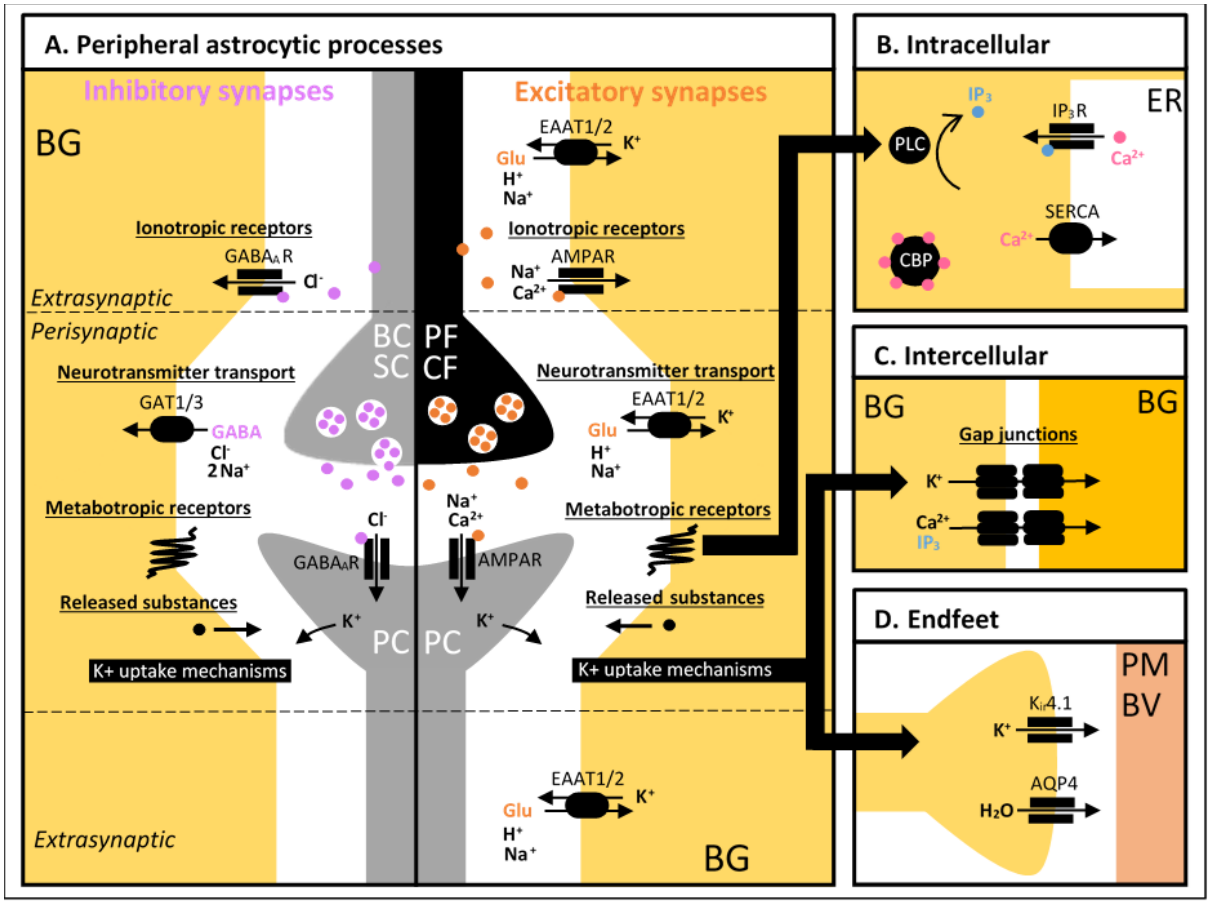


***Figure 5.*** *Main homeostatic and signaling mechanisms of Bergmann glia in different morphological structures (A-D). Abbreviations: AMPAR, α-amino-3-hydroxy-5-methyl-4-isoxazolepropionic acid receptor; AQP4, aquaporin-4; BC, basket cell; BG, Bergmann glia; BV, blood vessel; $Ca^{2+}$, calcium; CBP, $Ca^{2+}$ binding protein; $Cl^-$, chloride; CF, climbing fiber; EAAT, excitatory amino acid transporter; ER, endoplasmic reticulum; GABA, γ-aminobutyric acid; $GABA_AR$, GABA type A receptor; GAT, γ-aminobutyric acid transporter; Glu, glutamate; $H^+$, hydrogen; $H_2O$, water; $IP_3$, inositol trisphosphate; $IP_3R$, inositol trisphosphate receptor; $K^+$, potassium; $K_{ir}4.1$, inwardly rectifying potassium channel type 4.1; $Na^+$, sodium; PC, Purkinje cell; PF, parallel fiber; PLC, phospholipase C; PM, pia mater; SC, stellate cell; SERCA, sarco/endoplasmic reticulum $Ca^{2+}$ adenosine triphosphatase*

Intracellularly, cerebellar astroglial cells control the cytosolic $Ca^{2+}$ concentration by $Ca^{2+}$ binding proteins (CBPs) and the ER (Verkhratsky & Nedergaard, 2018). The CBS include endogenous/stationary and exogenous/mobile $Ca^{2+}$ buffers. ER serves as a $Ca^{2+}$ storage that accumulates $Ca^{2+}$ via SERCA pumps and releases $Ca^{2+}$ through $IP_3$ receptors that are activated by the PLC/$IP_3$ cascade initiated by the metabotropic receptors at PAPs. Other intracellular mechanism that might affect the $Ca^{2+}$ signaling in Bergmann glia is the store-operated $Ca^{2+}$ entry (SOCE), operated by plasmalemmal $Ca^{2+}$ channels, $Ca^{2+}$ sensors in the ER, and possibly SERCAs in the ER (Singaravelu et al. 2006).

Intercellularly, cerebellar astroglial cells are connected to each other via gap junctional channels that allow the passage of various ions and small molecules, including $K^+$ and $Ca^{2+}$ ions and $IP_3$. Intercellular connections are usually made within PAPs or endfeet of adjacent cells, but in rare cases, soma and process may be connected (Müller et al., 1996). Soma-soma contacts have not been observed. $Ca^{2+}$ wave propagation via gap junctions has not been observed in Bergmann glia. Instead, $Ca^{2+}$ increase caused by the activation of AMPARs induces the closing of gap junctions and constricts the $Ca^{2+}$ signal into the microdomain it was initiated in (Grosche et al., 2002; Müller et al., 1996). The propagation of $Ca^{2+}$ waves can occur via diffusion of ATP between adjacent astroglial cells (Hoogland et al., 2009).

Lastly, the endfeet extend to periphery of pia mater or blood vessels and mediate the transfer of various solutes via various channels and transporters. Most notably $K_{ir}4.1$ and AQP4 channels are colocalized in the endfeet and mediate the release of accumulated $K^+$ ions and water, respectively.

### 2.5.1 Calcium

Astrocytes mediate information flow via $Ca^{2+}$ transients, in a time-scale slower than the action potentials fired by neurons (Rusakov, 2015). Bergmann glial $Ca^{2+}$ signaling, in awake and active mice, exhibits three forms: flares, bursts, and sparkles (Nimmerjahn et al., 2009). Flares are $Ca^{2+}$ waves engaging a vast network of astrocytes, with the onset coinciding with blood perfusion associated with locomotion. Bursts are radial $Ca^{2+}$ waves affecting around 10-40 astrocytes and spreading three-dimensionally from the point of initiation. Sparkles are $Ca^{2+}$ increases restricted to individual Bergmann fibers. Spontaneous $Ca^{2+}$ waves have been observed also in anesthetized mice, both in Bergmann glia and velate astrocytes (Hoogland et al., 2009). In Bergmann glia, the waves spread three-dimensionally to a diameter of 50 μm at a speed of

4-11 μm/s. Velate cell waves had a diameter of 49 μm, expansion time of 2.5 s and lasted 10.4 s. Locally ejected ATP triggered $Ca^{2+}$ waves via P2Y receptors, and blocking the P2Y receptors suppressed the waves. (Hoogland et al., 2009) The spontaneous $Ca^{2+}$ waves have been shown to become more frequent with age and hypoxia (Mathiesen et al., 2013). Furthermore, the Bergmann glial $Ca^{2+}$ waves were shown to modulate the $Ca^{2+}$ levels in Purkinje cells; in contrast, spontaneous $Ca^{2+}$ waves in the Purkinje cells did not affect the Bergmann glia (Mathiesen et al., 2013).

### 2.5.2 Potassium

Neuronal excitability depends on astrocytes that remove excess $K^+$ from the extracellular space through local uptake and spatial buffering. Individual astrocytes mediate local $K^+$ uptake via Kir4.1 channels, NKA pumps, and NKCC1 transporters, and release with KCC1 transporters (Verkhratsky & Nedergaard, 2018). $K^+$ ions are distributed among neighboring astrocytes via gap junctions. Spatial buffering enables astrocytes to distribute the locally accumulated $K^+$ ions to neighboring astrocytes via gap junctions that release the $K^+$ ions through $K_{ir}4.1$ channels into the perivascular space or the interstitium to be released into the blood (Verkhratsky & Nedergaard, 2018). Spatial buffering in individual astrocytes is also possible, with $K^+$ ions distributed from presynaptic processes into the endfeet that release the accumulated $K^+$ ions.

### 2.5.3 Glutamate

Glutamate is the principal excitatory neurotransmitter in the CNS and glutamate levels at the synaptic cleft can rise to millimolar levels during synaptic transmission (Verkhratsky & Nedergaard, 2018). Astroglia are the main cells responsible for the maintenance of glutamate homeostasis and prevention of excitotoxicity by clearing glutamate from the synaptic cleft, sequestering neighboring synapses, and supplying glutamate into the neuronal terminals (Verkhratsky & Nedergaard, 2018). Bergmann glia are responsible for the uptake of around 80% of extracellular glutamate through the astroglial glutamate transporters EAAT1/2, shaping the dynamics of glutamate in the synaptic cleft and contributing to the synaptic transmission (Verkhratsky & Reichenbach, 2009).

# 3. OBJECTIVES

The first aim of this thesis was to build a functional and morphologically realistic single-cell model for a cerebellar astroglial cell. The suitability of a novel astrocyte modeling tool, ASTRO, was assessed for modeling the most well-known cerebellar astroglial cell type; the Bergmann glia. Morphometric values found from literature and a video file of a Bergmann glial appendage morphology were utilized for building the model. The second aim was to utilize the final Bergmann glial cell model for studying the spatiotemporal pattern of calcium wave dynamics with and without mobile buffers present. It was hypothesized that the spatiotemporal pattern of calcium wave dynamics would differ across the heterogenous morphology of the Bergmann glial cell.

# 4. MATERIALS AND METHODS

## 4.1 Simulation software

The computational model for Bergmann glial cell was implemented with NEURON and ASTRO simulation software.

### 4.1.1 NEURON

NEURON is a simulation environment for modeling neurons, from the level of individual cells to networks of neurons. The environment enables the user to construct, tune, and utilize models with features such as a variety of channel types, branching morphology, ionic diffusion, and second messenger properties. NEURON is programmed principally with hoc programming language, and interpreted with C-like syntax language or, alternatively, interpreted with Python. The default graphical user interface (GUI) of NEURON is adequate for creating models with wide-ranging levels of complexity. Additionally, hoc programming can be combined effectively with the GUI for optimization and more advanced applications. (Carnevale & Hines, 2006)

The key advantage of the NEURON environment is that it allows the user to evaluate and adjust the models directly based on their neurobiology: the architecture and biophysical properties of the neurons and their communications. Biophysical properties of the cell, including those on the membrane such as ion channels and transporters and those inside cytoplasm like second messengers and buffers, are defined by the user and described as differential equations. The properties are compiled for the efficient computation of the membrane voltage and gating states, using an integration method optimized for branched structures. NEURON applies the idea of a section, a continuous unbranched cable, as a direct analog to an unbranched neurite. By concatenation, sections can be assembled into branched tree structures, along which continuously variable biophysical properties can be applied. Each section can be further divided into segments with the parameter *nseg* to increase the resolution and spatial accuracy of simulations. (Carnevale & Hines, 2006)

Biophysical mechanisms are implemented in NEURON with a high level language NMODL (Carnevale & Hines, 2006). An NMODL language text file, or modfile, describes a biophysical

mechanism as a set of nonlinear algebraic equations, differential equations, or kinetic reaction schemes. Kinetic schemes equate the flow out of one state with the flow into another state. Biophysical mechanisms can be either distributed density mechanisms or point processes. Point processes are restricted to a small region and include a localized shunt that is induced by microelectrode impalement and described in the terms of net conductance or resistance and the total current. Distributed mechanisms are scattered over the cell surface and include voltage-gated ion currents and a passive leak current, described in terms of conductance and current per unit area.

### 4.1.2 ASTRO

ASTRO is a novel computational tool for modeling astrocytes in the NEURON simulation environment (Savtchenko et al., 2018). Through NEURON a repertoire of biophysical mechanisms can be incorporated into biologically relevant, multi-compartmental astrocyte models in ASTRO. The main advantage of ASTRO is that it makes it possible to model the fine nanoscopic architecture of astrocytes. ASTRO provides simulations for $Ca^{2+}$ wave propagation, microscopic $Ca^{2+}$ dynamics, membrane biophysics of glutamate transport, dynamics of intra- and extracellular $K^{+}$, and fluorescence recovery after photobleaching (FRAP).

The latest installation version of ASTRO and the accompanying User Guide can be downloaded online (available at https://github.com/LeonidSavtchenko/Astro). Software requirements for executing basic version of ASTRO (without full-scale simulations of intracellular $Ca^{2+}$ dynamics) include MATLAB (available at version 2012 or later, https://uk.mathworks.com/products/matlab.html) and NEURON (available at version 7.2 or later, https://neuron.yale.edu/neuron/download), installed under Windows 10 or Windows 7. Full version of ASTRO (with full-scale simulations of intracellular $Ca^{2+}$ dynamics in addition to the other biophysical mechanisms) would require remote Worker computer cluster operating under Linux in addition to the host computer.

Building a morphologically-detailed astrocyte model with ASTRO consists of three stages (Savtchenko, 2018). First, the gross morphology of the cell is reconstructed, including the soma and larger branches, while excluding the nanoscopic processes. Second, nanoscopic processes are automatically generated based on the morphometric 3D electron microscopy data and the tissue volume filling based on volumetric two-photon excitation imaging data. Third, desired biophysical functions can be incorporated by adjusting the parameters of the modeled astroglia.

## 4.2 Bergmann glial model

Creating a morphologically detailed computational model for a Bergmann glial cell was done in five steps: 1) Preparing a three-dimensional reconstruction of a Bergmann glial appendage, 2) obtaining statistical properties for the nanoscopic architecture from the three-dimensional reconstruction with ASTRO NanoGeometry module, 3) building a stem tree with values found from the literature, 4) populating the stem tree with the nanoscopic processes with ASTRO, and 5) incorporating the biophysical mechanisms into the complete morphology with ASTRO.

### 4.2.1 Appendage reconstruction

A three-dimensional reconstruction of a Bergmann glial appendage consisting of several microdomains was provided by Grosche et al. (1999) in a video format as the original three-dimensional reconstruction file was not available. The original morphology had been three-dimensionally reconstructed from 450 ultrathin sections from about 20 μm segment of a Bergmann glial cell from a 20-22-day-old mouse (Grosche et al., 1999). The video file consisted of 53 frames that depicted the rotated morphology. Construction of a three-dimensional mesh from the frames was performed with AgiSoft Metashape Professional (Version 1.6.2). First, the frames were aligned with key point limit of 500,000, tie point limit of 0 (0 corresponds to no limit to the number of tie points), generic preselection, and highest accuracy. Key points are defined automatically by the program as the recognizable features in the images, tie points connect the similar key points from the different frames, and the generic preselection matches overlapping images first with a lower accuracy until all matches are found. Next, the dense point cloud was built with ultra-high quality and depth filtering disabled. The mesh was created from the dense point cloud with face count of 500,000 and interpolation enabled. Creation of the surface points was performed with Blender (Version 2.79b). First, the mesh was scaled proportionally so that the height of the mesh was 20 Blender units, interpreted by the ASTRO NanoGeometry module directly as 20 μm. After the mesh was scaled, ParticleSystem was added onto the surface of the mesh with a grid resolution of 160x160. The locations of the surface points were saved into a DAT-file to be used in the ASTRO NanoGeometry module.

### 4.2.2 Nanoscopic processes

Statistics for the nanoscopic processes were obtained from the reconstructed Bergmann glial appendage with the ASTRO NanoGeometry module.

### 4.2.3 Stem tree

The Bergmann glial stem tree was constructed with the NEURON Cell Builder tool (Hines & Carnevale, 2001) with morphometric values found from literature for mouse Bergmann glia. The cell parts included soma, main processes, endfeet, and five different types of lateral processes (Table 4). The main processes were attached directly onto the soma and constructed in such a way that they gradually tapered from the soma and for the most of their length were 0.7 μm wide and in total 80 μm long (Siegel et al., 1991). Stubby and thin lateral processes were modeled as single sections; the branching and bulbous comprised of either one, two, or three sections. The stem tree was populated with the four different types of lateral processes based on the categorization of subtypes and their frequencies by Lippman et al. (2008). In Bergmann glia of 20-day-old mice, the frequency of the lateral process subtypes along 10 μm of stem process were 1.49, 0.36, 0.4, and 1.25 for the stubby, thin, branching, and bulbous subtypes, respectively. In addition to these subtypes, a few short sections named “stem” were created. The same number of each lateral process subtype was attached to each of the main processes relatively uniformly along their length. The nanoscopic processes will be attached only to the branching, bulbous, and stem lateral process subtypes.

***Table 4.*** *Morphometric values of a Bergmann glial cell*

| Cell part | | Number | Sections | | | Species & age | Reference |
|---|---|---|---|---|---|---|---|
| | | | Diameter | Length | Number | | |
| Soma | | 1 | 8.5 µm | 8.5 µm | 1 | Mouse | (Muller et al., 1994) |
| Main processes | | 4 | 3 µm | 5 µm | 1 | Mouse, 2 years | (Siegel et al., 1991) |
| | | | 2 µm | 5 µm | 1 | | |
| | | | 1.2 µm | 5 µm | 1 | | |
| | | | 0.7 µm | 5 µm | 13 | | |
| Endfeet | | 4 | 4 µm | 4 µm | 1 | Mouse, P26 | (Saab et al., 2012) |
| Lateral processes | Stubby | 48 | 0.65 µm | 1 µm | 1 | Mouse, P20 | (Grosche et al., 1999; Lippman et al., 2008) |
| | Thin | 12 | 0.65 µm | 6 µm | 1 | | |
| | Branching 1 | 4 | 1 µm | 3 µm | 1 | | |
| | Branching 2 | 4 | 1 µm | 3 µm | 2 | | |
| | Branching 3 | 4 | 1 µm | 3 µm | 3 | | |
| | Bulbous 1 | 8 | 0.3 µm | 2 µm | 1 | | |
| | Bulbous 2 | 16 | 0.3 µm | 3 µm | 1 | | |
| | | | 0.7 µm | 1 µm | 1 | | |
| | Bulbous 3 | 16 | 0.3 µm | 4 µm | 1 | | |
| | | | 0.9 µm | 2 µm | 1 | | |
| | | | 0.7 µm | 1 µm | 1 | | |
| | Stem | 8 | 1 µm | 0.5 µm | 1 | | |

### 4.2.4 The complete morphology

Uploading the stem tree into ASTRO

There are three options in ASTRO for uploading the astrocyte morphology file to perform simulations: “Select library stem tree”, “Select stem tree with endfoot”, and “Select reconstructed stem tree”. Since the first two options did not preserve the stem tree diameters specified with the Cell Builder tool, the last option was used. This option opens a pop-up box with possibility to adjust the dimensions and location of the astrocyte with parameters for the X-Y scale, Z scale, and X-Y shift, with default values of 5.5, 2, and 200, respectively. These options are mainly relevant for three-dimensionally constructed astrocyte models. Since the two-dimensional Bergmann glial model created with the Cell Builder tool was already correctly scaled and centered, the values of X-Y scale, Z-scale, and X-Y shift were changed to 1, 1, and 0, respectively. As it was not possible to modify all the values in the pop-up box (the box disappeared after changing any of the values), the values were modified directly to the init.hoc and MainProgram.hoc files of the ASTRO tool’s NeuronSims module.

Attaching seeds and nanoprocesses

ASTRO first attaches to the stem tree small sections of length 0.1 μm and diameter 3 μm called "seeds" which will give rise to the nanoprocesses. One nanoprocess is attached to one seed. The parameters NumberDendrites and SeedNumber of the initial script intended to be placed in the beginning of the morphology file define how many seeds and nanoprocesses are created. By default each section, except for the soma and the first section, give rise to three seeds attached consecutively: first seed is attached to the stem tree section, second seed to the first seed, and third seed to the second seed. The final model then has nanoprocesses as bundles of three attached to each section, except for the soma to which no seed is attached and the first section to which only one seed and nanoprocess are attached.

In the case of the Bergmann glial cell model, the seeds and nanoprocesses should neither be attached to all of the sections that make up the main processes nor to the thin or stubby lateral processes. In order to specify the subset of sections (in the NEURON nomenclature, "dendrites") to which ASTRO attaches seeds and nanoprocesses two new parameters were defined: SubsetFirstDend and NumberDendritesSubset. SubsetFirstDend defines the first section to which seeds will be attached and NumberDendritesSubset the number of sections in the subset.

The initial script was modified in the following way (modifications in bold):

```
OriginalDendrite=248 // This number should correspond to the
number of the dendrites of the
//3D reconstructed geometry
SubsetFirstDend=128 // This number should correspond to the
first dendrite that nanoprocesses will
// be attached to (all the subsequent dendrites starting from
this dendrite will then have nanoprocesses)
SubsetDendrites=OriginalDendrite-SubsetFirstDend
NumberDendrites=OriginalDendrite+2*(SubsetDendrites-1)
NumberDendritesSubset=SubsetDendrites+2*(SubsetDendrites-1)
SeedNumber= SubsetDendrites-1
create soma[1]
create dendrite[NumberDendrites]
access soma[0]
```

The Cellinit.hoc file of the ASTRO tool's NeuronSims module was modified in the following way: the original parameter NumberDendrites was substituted by the **NumberDendritesSubset** in lines 8, 89, and 94; the number defining the starting dendrite (i = 0) was changed to

**SubsetFirstDend** in line 15; dendrite[i] was changed to **dendrite[SubsetFirstDend]** in line 82; and dendrite[i] was changed to **dendrite[i+SubsetFirstDend]** in line 90.

### 4.2.5 Calcium mechanisms in simulations

Most of the biophysical mechanisms incorporated into the ASTRO simulations for $Ca^{2+}$ wave, microscopic $Ca^{2+}$ dynamics, membrane biophysics of glutamate transport, and dynamics of intra- and extracellular $K^+$ are present also in Bergmann glia. The only exception is the L-type $Ca^{2+}$ channel that has not been detected in Bergmann glia.

The biophysical mechanisms in the ASTRO $Ca^{2+}$ simulations, including relevant cytosolic, plasma membrane, and ER mechanisms, are explained in this section (Table 5). The cytosolic mechanisms include diffusion and $Ca^{2+}$ buffering. The diffusion consists of radial diffusion through four concentric shells that surround a cylindrical central core and longitudinal diffusion between corresponding concentric compartments. The buffers consists of endogenous stationary buffers and exogenous mobile buffers. The plasma membrane mechanisms include the PMCA pump, L-type $Ca^{2+}$ channel, and gap junction. The ER mechanisms include $IP_3R$, SERCA pump, and leak current. All of the above $Ca^{2+}$ mechanisms except L-type $Ca^{2+}$ channel and gap junction are derived from the same model (Fink et al., 2000) available in ModelDB (McDougal et al., 2017; accession number 125745).

***Table 5.*** *Mechanisms active during $Ca^{2+}$ wave simulation*

| TYPE | MECHANISM | LOCALIZATION |
|---|---|---|
| Cytosolic mechanisms | Radial and longitudinal diffusion | Soma, branches, leaves, stalks |
| | Endogenous/stationary buffer | |
| | Exogenous/mobile buffer | |
| Plasma membrane mechanisms | PMCA pump | Soma, branches, leaves, stalks |
| | L-type $Ca^{2+}$ channel | Branches |
| | Gap junction | Soma, branches |
| ER membrane mechanisms | $IP_3R$ | Soma, branches, leaves, stalks |
| | SERCA pump | |
| | Leak current | |

Abbreviations: $Ca^{2+}$, calcium; ER, endoplasmic reticulum; $IP_3R$, inositol trisphosphate receptor; PMCA, plasma membrane $Ca^{2+}$-ATPase; SERCA, sarco/endoplasmic reticulum $Ca^{2+}$-ATPase.

Calcium buffers

Mobile buffers are denoted by $B_m$ and stationary buffers by $B_s$ with corresponding kinetic constants $k_f$ and $K_D$. The buffer reactions are

$Ca^{2+} + B_s \rightleftharpoons CaB_s \ (k_{fs}, K_{Ds}k_{fs})$,

$Ca^{2+} + B_m \rightleftharpoons CaB_m \ (k_{fm}, K_{Dm}k_{fm})$,

where $k_{fs}$ is the reaction rate constant for a stationary buffer, $K_{Ds}$ the dissociation constant for the stationary buffer, $k_{fm}$ the reaction rate constant for a mobile buffer, and $K_{Dm}$ the dissociation constant for the mobile buffer.

Diffusion and plasma membrane mechanisms

The $Ca^{2+}$ equation including diffusion as well as L-type $Ca^{2+}$ channels and PMCA pump can be given as

$$\frac{d[Ca^{2+}]_i}{dt} = D_{Ca}\frac{d^2[Ca^{2+}]_i}{dt^2} - \frac{\pi(i_{CaL}-i_{pump})D}{2F},$$

where $[Ca^{2+}]_i$ is the intracellular $Ca^{2+}$ concentration, $D_{Ca}$ is the diffusion coefficient, $D$ is the local diameter, $F$ is the Faraday constant, $i_{CaL}$ is the sum of L-type $Ca^{2+}$ currents, and the $i_{pmca}$ is the current through PMCA pump. The equation for $i_{pmca}$ can be given as

$$i_{pmca} = 2F\frac{J_f - J_b}{A_{pump}},$$

where $J_f$ and $J_b$ are the forward and reverse fluxes and $A_{pump}$ is the pump area per unit length.

L-type calcium current

Model for L-type $Ca^{2+}$ current is from ModelDB (Uebachs et al., 2010; accession number 125152). The model was originally described in Royeck et al. (2008). Activation dynamics of the L-type $Ca^{2+}$ current are modeled with equations

$$i_{CaL} = Q(T)\bar{P}_{Ca}m^2\frac{2{\cdot}10^{-5}\ mM}{2{\cdot}10^{-5}\ mM+[Ca^{2+}]_i}\cdot\frac{4F^2V}{RT}\frac{[Ca^{2+}]_o-[Ca^{2+}]_i e^{\frac{2FV}{RT}}}{1-e^{\frac{2FV}{RT}}},$$

$$\frac{dm}{dt} = \frac{m_\infty - m}{\tau_m},$$

$$m_\infty = \left(\frac{1}{1+e^{-\frac{V+11\ mV}{5.7\ mV}}}\right)^{0.5},$$

$$\tau_m = \frac{1}{Q(T)(\alpha_m+\beta_m)},$$

$$\alpha_m = 0.1967\ mV^{-1} \cdot \frac{V - 34.88\ mV}{1 - e^{\frac{-(V-34.88\ mV)}{10\ mV}}},$$

$$\beta_m = 0.046 \cdot e^{-\frac{V-15\ mV}{20.73\ mV}},$$

where $\bar{P}_{Ca}$ is the maximal $Ca^{2+}$ permeability, $F$ is the Faraday constant, $R$ is the ideal gas constant, V is the membrane potential, $[Ca^{2+}]_i$ is the intracellular $Ca^{2+}$ concentration, and $[Ca^{2+}]_o$ is the extracellular $Ca^{2+}$ concentration, and $Q(T)$ is the reaction rate at temperature $T$.

Gap junction

Current leak through gap junctions is modeled as

$$i = \frac{-V_{gap} + V}{R_{gap}},$$

where $R_{gap}$ is the gap junction resistance and $V_{gap}$ the gap junction reversal potential.

$IP_3$ receptor

The flux via $IP_3$Rs from the ER to the cytosol can be given as

$$j_{IP3R} = j_{max}\left(1 - \frac{[Ca^{2+}]_i}{[Ca^{2+}]_{ER}}\right)\left(\frac{[IP_3]_i}{[IP_3]_i + K_{IP3}} \frac{[Ca^{2+}]_i}{[Ca^{2+}]_i + K_{act}} h\right)^3,$$

where $[Ca^{2+}]_i$ is the intracellular $Ca^{2+}$ concentration, $[Ca^{2+}]_{ER}$ is the $Ca^{2+}$ concentration in the ER, $[IP_3]_i$ is the intracellular $IP_3$ concentration, $K_{IP3}$ is the dissociation constant for $IP_3$ binding to an activation site, $K_{act}$ is the dissociation constant for $Ca^{2+}$ binding to an activation site, and $j_{max}$ is the maximal $IP_3$R mediated flux.

The differential equation for the gating variable $h$ of the $IP_3$R inactivation can be given as

$$\frac{dh}{dt} = k_{on}(K_{inh} - ([Ca^{2+}]_i + K_{inh})h),$$

where $[Ca^{2+}]_i$ is the intracellular $Ca^{2+}$ concentration, $k_{on}$ is the reaction rate constant for $Ca^{2+}$ binding to the inhibition site, and $K_{inh}$ is the dissociation constant for $Ca^{2+}$ binding to the inhibition site.

SERCA pump

The mechanistic details of the SERCA pump (Hill equation) are as described in Hernjak et al. (2005). The SERCA pump mediates the uptake of $Ca^{2+}$ ions from the cytoplasm into the ER. The flux equation can be given as

$$j_{SERCA} = v_{max} \frac{[Ca^{2+}]_i^2}{[Ca^{2+}]_i^2 + {K_p}^2},$$

where $[Ca^{2+}]_i$ is the intracellular $Ca^{2+}$ concentration, $v_{max}$ is the maximum rate, and $K_p$ is the half-activation constant of the pump.

Leak

Equation for $Ca^{2+}$ leak flux from the ER to the cytosol is modeled as

$$j_{leak} = L\left(1 - \frac{[Ca^{2+}]_i}{[Ca^{2+}]_{ER}}\right),$$

where $[Ca^{2+}]_i$ is the intracellular $Ca^{2+}$ concentration, $[Ca^{2+}]_{ER}$ is the $Ca^{2+}$ concentration in the ER, and $L$ is a leak constant that depends on the flux balance conditions at a steady state. Nominally $L = 0.1$ nM ms$^{-1}$, but it is adjusted so that

$j_{IP3R} + j_{SERCA} + j_{leak} = 0$, when $[Ca^{2+}]_i = 50$ nM and $h = \frac{K_{inh}}{[Ca^{2+}] + K_{inh}}$.

The parameter values used in this work for simulating the Bergmann glial model are the preset values in ASTRO except for the mobile buffer concentration that was adjusted for the $Ca^{2+}$ wave simulations. The parameters and variables for the $Ca^{2+}$ wave simulations are listed in Table 6.

***Table 6.*** *Parameters and variables of $Ca^{2+}$ wave simulation*

| SYMBOL | VALUE | UNIT | DESCRIPTION |
|---|---|---|---|
| $[Ca^{2+}]_{ER}$ | 0.4 | mM | $Ca^{2+}$ concentration in the ER |
| $F$ | 96485 | C | Faraday constant |
| $R$ | 8.3134 | J/°C | Ideal gas constant |
| $T$ | 279.45 | K | Temperature |
| **Cytosolic mechanisms** | | | |
| $[B_s]$ | 0.07 | mM | Total concentration of endogenous/stationary $Ca^{2+}$ buffer |
| $[B_m]$ | 0 or 0.01 | mM | Total concentration of an exogenous/mobile $Ca^{2+}$ buffer |
| $D_{Ca}$ | 0.3 | $\mu m^2\ ms^{-1}$ | Diffusion coefficient of $Ca^{2+}$ |
| $[IP_3]_i$ | 0.05 | mM | Intracellular $IP_3$ concentration |
| $k_{fs}$ | 1000 | $mM^{-1}\ ms^{-1}$ | Reaction rate constant of a stationary buffer |
| $K_{Ds}$ | 10 | µM | Dissociation constant of a stationary buffer |
| $k_{fm}$ | 1000 | $mM^{-1}\ ms^{-1}$ | Reaction rate constant of a mobile buffer |
| $K_{Dm}$ | 0.24 | µM | Dissociation constant of a mobile buffer |
| $D_m$ | 0.05 | $\mu m^2\ ms^{-1}$ | Diffusion coefficient of a mobile buffer |
| **Plasma membrane mechanisms** | | | |
| $[Ca]_c$ | $2 \times 10^{-5}$ | mM | PMCA activation threshold |
| $\gamma$ | 20 | $\mu M\ s^{-1}$ | PMCA flux density |
| $A_{pump}$ | $2\pi r$ | µm | PMCA area per unit length. |
| $\bar{P}_{Ca}$ | 0.00006622 | cm/s | Maximal $Ca^{2+}$ permeability of the channel |
| $R_{gap}$ | 100000 | Mohm | Gap junction resistance |
| $V_{gap}$ | -85 | mV | Gap junction reversal potential |
| **ER membrane mechanisms** | | | |
| $j_{max}$ | $3.5 \times 10^{-3}$ | $mM\ ms^{-1}$ | Maximal $Ca^{2+}$ flux through $IP_3R$ |
| $k_{on}$ | 2.7 | $mM^{-1}\ ms^{-1}$ | Reaction rate constant of $Ca^{2+}$ binding to $IP_3R$ inhibition site |
| $K_{inh}$ | $0.2 \times 10^{-3}$ | mM | Dissociation constant for $Ca^{2+}$ binding to $IP_3R$ inhibition site |
| $K_{IP3}$ | $0.8 \times 10^{-3}$ | mM | Dissociation constant for $IP_3$ binding to $IP_3R$ activation site |
| $K_{act}$ | $0.3 \times 10^{-3}$ | mM | Dissociation constant for $Ca^{2+}$ binding to $IP_3R$ activation site |
| $v_{max}$ | $3.75 \times 10^{-6}$ | $mM\ ms^{-1}$ | Maximum rate of $Ca^{2+}$ through SERCA pump |
| $K_p$ | 0.00027 | mM | Half-activation constant of SERCA pump |
| $L$ | $0.1 \times 10^{-6}$ | $mM\ ms^{-1}$ | Leak constant |
| **Variables** | | | |
| $[Ca^{2+}]_i$ | $50 \times 10^{-6}$ | mM | Initial value of intracellular $Ca^{2+}$ concentration |
| $[Ca^{2+}]_o$ | 10 | mM | Initial value of extracellular $Ca^{2+}$ concentration |
| $V$ | -85 | mV | Initial value of membrane potential |

Abbreviations: $Ca^{2+}$, calcium; ER, endoplasmic reticulum; $IP_3$, inositol trisphosphate; $IP_3R$, $IP_3$ receptor; PMCA, Plasma membrane $Ca^{2+}$-ATPase; SERCA, sarco/endoplasmic reticulum $Ca^{2+}$-ATPase.

# 5. RESULTS

A morphologically detailed Bergmann glial single-cell model was constructed based on a Bergmann glial appendage morphology from a video file (Grosche et al., 1999) and morphometric values from literature. First, the appendage was reconstructed from the video file as a point cloud where the points were aligned in equidistant circumvents on the shape surface. Second, nanoscopic processes were selected from the appendage and transformed into NEURON and ASTRO -compatible cylindrical structures. Third, a Bergmann glial stem tree was built based on values from the literature. Fourth, the complete single-cell model was assembled by populating the stem tree with the nanoscopic processes. The final model was used in $Ca^{2+}$ wave simulations. In the following sections, the details of these different stages are explained.

## 5.1 Appendage reconstruction

The ASTRO NanoGeometry module is intended for three-dimensional reconstructions of astrocyte fragments, which should be in a format of a XYZ scatter with points circumventing along the original tissue sections. Currently no three-dimensional reconstructions for cerebellar astrocytes are available in the public morphology databases. The data for the Bergmann glial fragment modeled in this work was given to us in a video format (Grosche et al., 1999) and it had to be first transformed into a format compatible with the ASTRO Nanogeometry module.

The procedure to transform the obtained video format into ASTRO-compatible format was developed in this thesis. The procedure included two stages: first, the morphology was reconstructed as a mesh with Agisoft Metashape, after which a regular grid of points was created onto the mesh surface with Blender. The mesh was created from the frames extracted from the video file with Agisoft Metashape in three steps (Figure 6A-C). First, the frames were imported into Metashape that matched the common points between the images and positioned the cameras for each image accordingly. The frames were aligned well; but as seen in Figure 6A, they did not cover the full rotation of the appendage. After the alignment, the estimated camera positions and images were used to build a dense point cloud. Based on the dense point cloud, a three-dimensional polygonal mesh was created. As seen in the Figure 6C, several small shapes were separate from the rest of the mesh. The separate small shapes were removed

manually in the Blender before creating the surface points. The Figure 6D depicts the grid particle system points aligned on the surface of the appendage. Comparison of the appendage point cloud reconstructed from the video file to the original 3D reconstruction is presented in Figure 7.

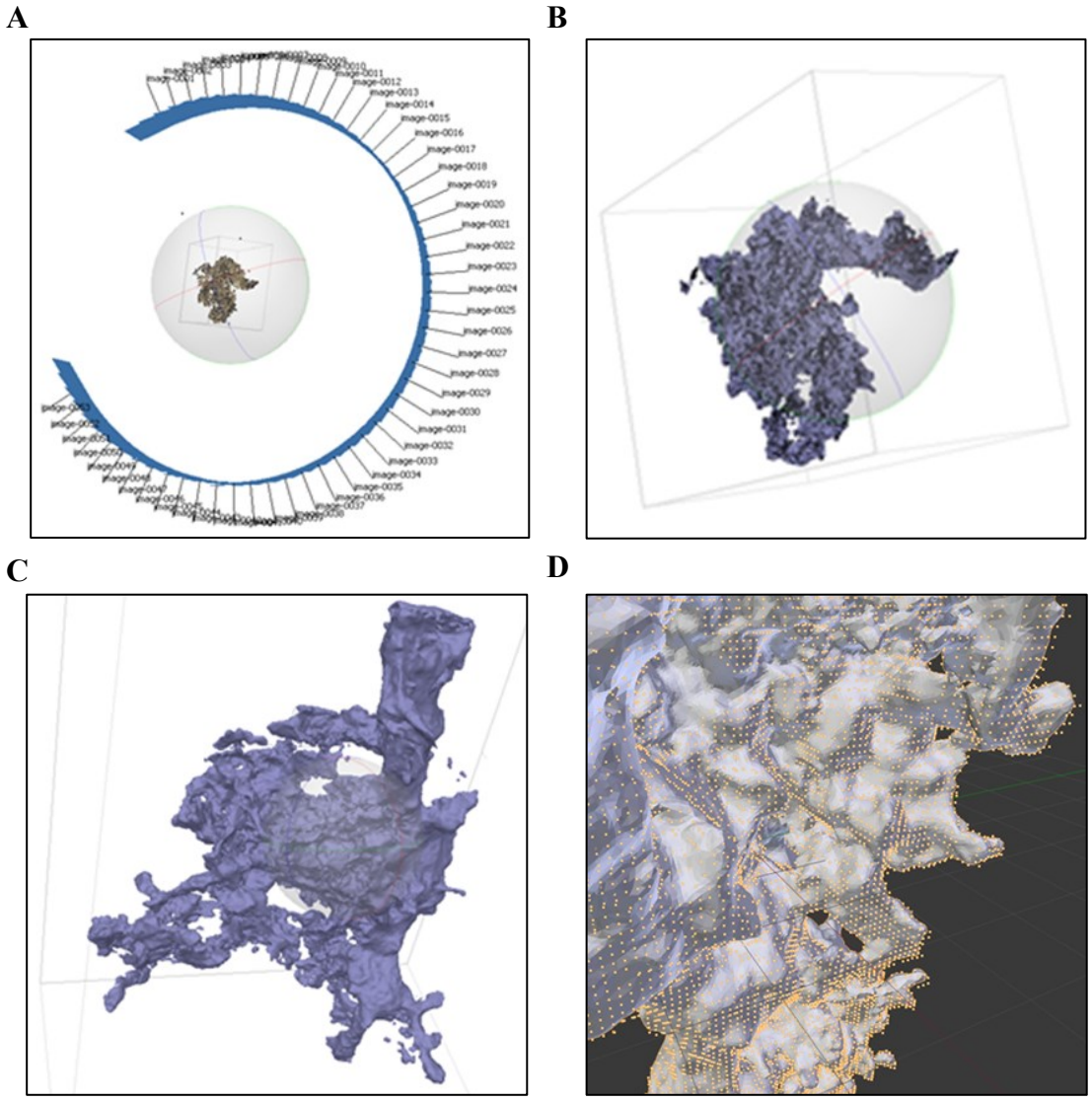


***Figure 6.*** *Morphology reconstruction from a video file provided by Grosche et al.* (1999). *The software used include Agisoft Metashape (A-C) and Blender (D). A) Frames aligned from the video file to form a sparse point cloud. The names along the blue semicircle are the individual frames and the brownish structure in the middle is the sparse point cloud. B) A dense point cloud formed based on the alignment of the frames. C) The final mesh constructed from the dense point cloud. D) A grid particle system created onto the surface of the mesh.*

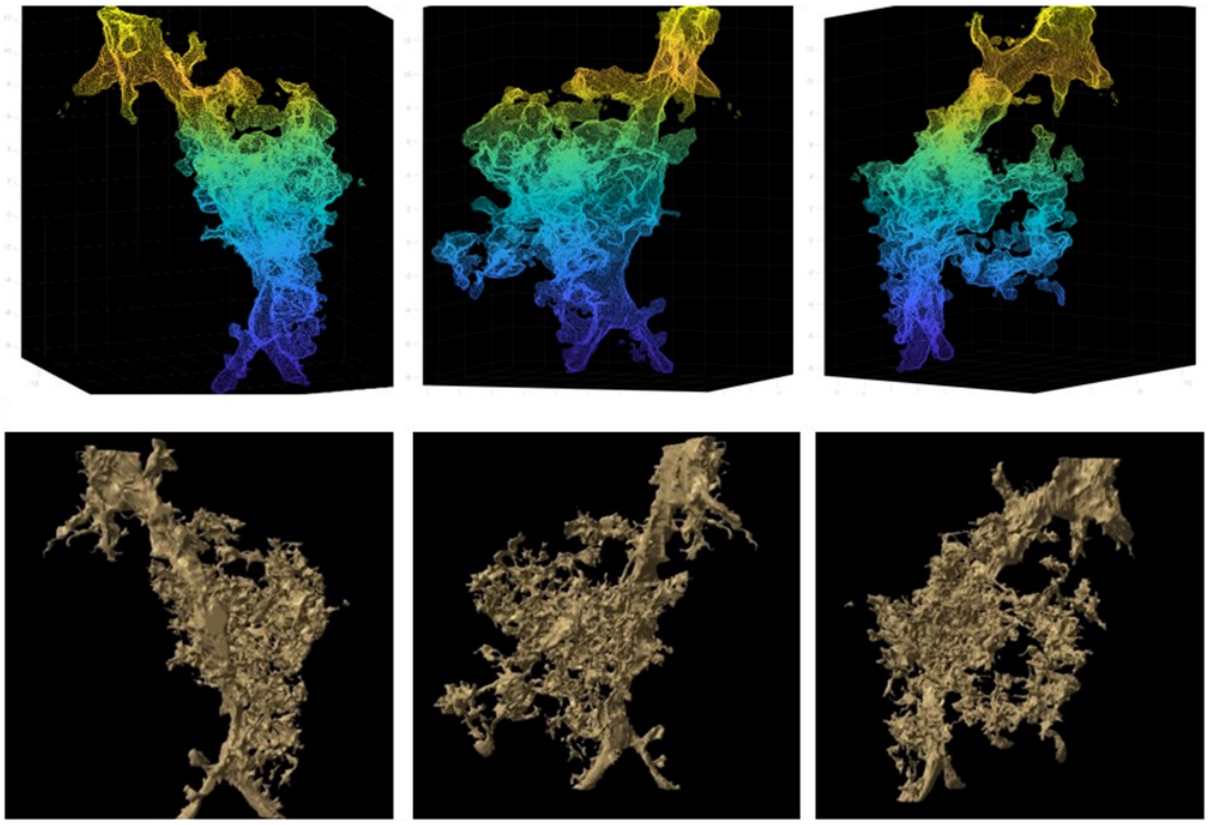

***Figure 7.*** *Comparison of the appendage point cloud reconstructed from the video file (upper row) to the original 3D reconstruction (lower row).*

## 5.2 Nanoscopic processes

The appendage morphology constructed in the previous section was utilized for determining the distribution of nanoscopic processes with the ASTRO Nanogeometry module. Determining the distribution for the nanoscopic processes consisted of four steps. First, the morphology was imported into the ASTRO Nanogeometry tool where all the viable nanoscopic processes from the shape were manually selected. Second, the selected nanoprocesses were transformed into NEURON-compatible cylindrical structures which were individually adjusted to obtain the best possible geometrical and physical match with the original shapes. Lastly, a cylinder radii distribution was formed based on the cylinder diameters of all the adjusted cylindrical structures. The distribution was saved into a text-file to be used when creating the nanoprocesses onto the stem tree.

The selected nanoscopic processes were classified as “good” if they were qualitatively suitable for cylinder reconstruction (Figure 8A). All the of the shapes that were sticking out of the main shape and could be distinguished as nanoprocesses were selected. In total 19 distinct

nanoprocesses were selected with the tool, twelve of which were classified as good (highlighted with different colors in Figure 8B). In few cases it was possible to select only part of the nanoprocess, as the shape as a whole was not qualitatively suitable for cylinder reconstruction. Three examples of the nanoprocesses classified as good are presented in Figure 9. As can be seen, the nanoprocesses could not always be completely selected. In the case of the shapes in Figures 9A and C, small portions of the nanoprocess were excluded, and in the case of the shape in Figure 9A also a small part of the head. The nanoprocesses were selected as accurately as possible with the ASTRO Nanogeometry tool. The shapes were classified mathematically unusable if they had data outliers, topological confusion, or too few data points. An example of a nanoprocess that was unusable is presented in Figure 10. As can been seen in the figure, the points in the upper half of the shape are not properly connected and the Nanogeometry tool failed to form a polygonal stack from the shape.

**A**

| Section name | Good | Levels | Points | Use |
|---|---|---|---|---|
| Whole appendage | No | 381 | 43995 | ☐ |
| Nanoprocess 1 | Yes | 17 | 482 | ☑ |
| Nanoprocess 2 | Yes | 16 | 240 | ☑ |
| Nanoprocess 3 | Yes | 13 | 245 | ☑ |
| Nanoprocess 4 | Yes | 22 | 595 | ☑ |
| Nanoprocess 5 | Yes | 8 | 164 | ☑ |
| Nanoprocess 6 | Yes | 6 | 117 | ☑ |
| Nanoprocess 7 | Yes | 6 | 80 | ☑ |
| Nanoprocess 8 | Yes | 15 | 397 | ☑ |
| Nanoprocess 9 | No | 15 | 723 | ☐ |
| Nanoprocess 10 | No | 11 | 461 | ☐ |
| Nanoprocess 11 | Yes | 8 | 135 | ☑ |
| Nanoprocess 12 | Yes | 9 | 293 | ☑ |
| Nanoprocess 13 | Yes | 17 | 1208 | ☑ |
| Nanoprocess 14 | Yes | 16 | 457 | ☑ |
| Nanoprocess 15 | No | 17 | 163 | ☐ |
| Nanoprocess 16 | No | 29 | 502 | ☐ |
| Nanoprocess 17 | No | 17 | 121 | ☐ |
| Nanoprocess 18 | No | 13 | 240 | ☐ |
| Nanoprocess 19 | No | 5 | 25 | ☐ |

**B**

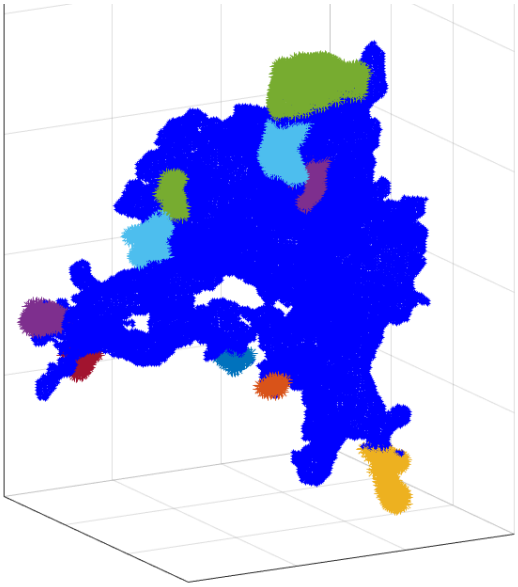

***Figure 8.*** *Selecting nanoscopic processes with ASTRO NanoGeometry module. A) List of the selected and stored sections, indicating whether the shape is qualitatively suitable for cylinder reconstruction (Yes/No), the number of levels (stacks) of points, and the total amount of points. B) Reconstruction of the Bergmann glial appendage with the twelve selected nanoprocesses highlighted.*

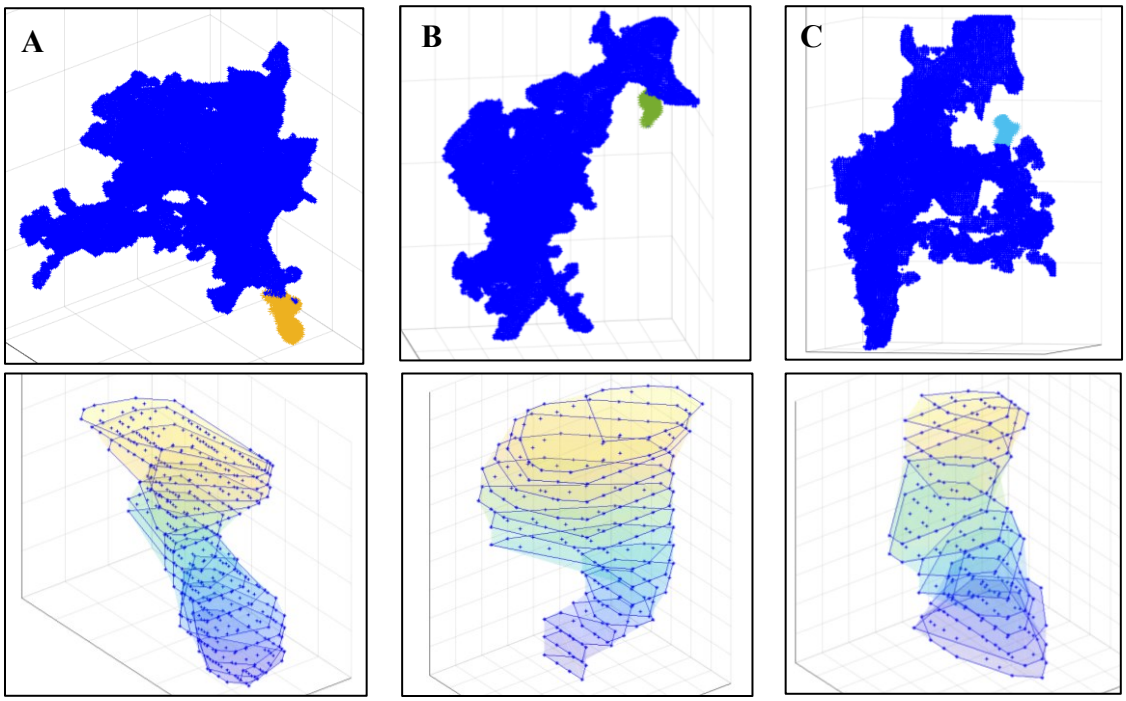


***Figure 9.*** *Examples of the selected nanoprocesses classified as "good". The nanoscopic processes constitute of stacks of polygonal slabs formed by the surface points.*

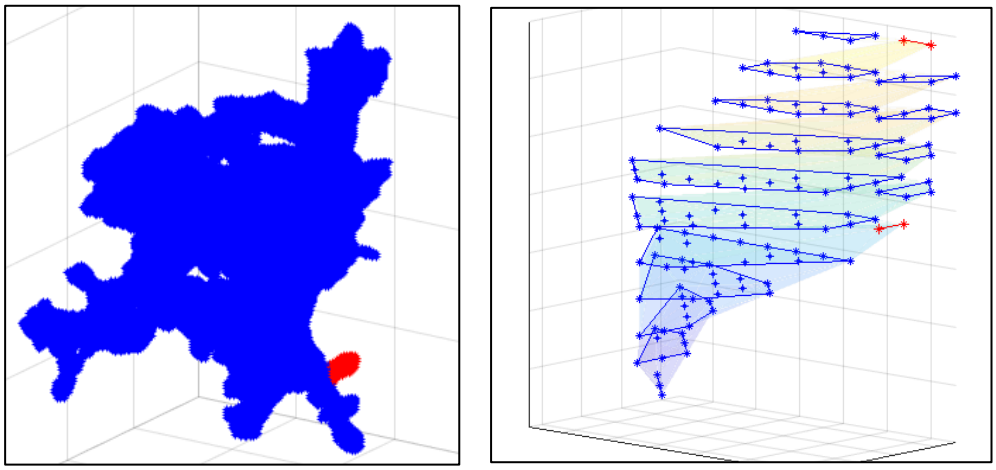

***Figure 10.*** *Example of a qualitatively unusable nanoprocess. The points that form the circumvents of the nanoprocess were not connected correctly.*

All twelve selected polygonal shapes were transformed into cylindrical models which preserved their geometrical and physical properties. The strategy ASTRO employs to accomplish this is to convert each of the adjacent polygonal slabs into three cylindrical disks, where the middle disk corresponds to a "transitional" cylinder and the two surrounding disks are the "regular"

cylinders. The regular cylinders have surface areas corresponding to those of the polygonal slabs. The transitional cylinder has a surface area that corresponds to the interface area between the polygonal slabs. By transforming the two adjacent polygonal slabs into three cylindrical disks, both the side area and the cross-sectional area of the original polygonal shape are for the most part conserved in the final cylinder model. The final cylinder model constitutes of 2N-1 cylindrical disks, with N regular and N-1 transitional disks. All twelve selected nanoprocesses were transformed this way from stacks of polygons into stacks of cylinders.

For the biophysical comparison of the original polygonal shapes and the NEURON-compatible cylinder structures, ASTRO utilizes a simple mode Monte Carlo test. The Monte Carlo test uses Brownian diffusion and electrodiffusion of free particles. The particles are injected in one end of the stack and escape from the other end. The test was implemented for all of the twelve selected nanoprocesses. In Figure 11, the test is displayed for one of the nanoprocesses (the nanoprocess from Figure 9C). By adjusting the diameters of the transitional cylinders by coefficient 0.6, the cylinder-based shape was able to replicate the dynamics of the particle flux of the original polygonal shape reasonably well (Figure 11B). The diameters of the transitional cylinders in the twelve selected shapes were adjusted when needed.

After all the shapes were transformed into cylindrical structures and the diameters of the transitional cylinders adjusted accordingly, the radii of both the regular and transitional cylinders were saved into a radii cylinder distribution file. The cylinder radii distribution of the same nanoscopic process as in Figures 9C and 11 is presented in Figure 12 before and after adjusting the effective diameters of the transitional cylinders. In the adjusted shape, the radii distribution of the transitional cylinders is more clearly distinct from the radii distribution of the regular cylinders. The cylinder radii distribution pooled from all the transformed and adjusted nanoscopic processes is presented in Figure 12C. As observed from the distribution, most of the shapes had a radius of around 0.1 μm, with the number of cylinders gradually decreasing as the radius increased. The distribution was saved into a file to be used in the generation of the nanoscopic processes onto the Bergmann glial stem tree.

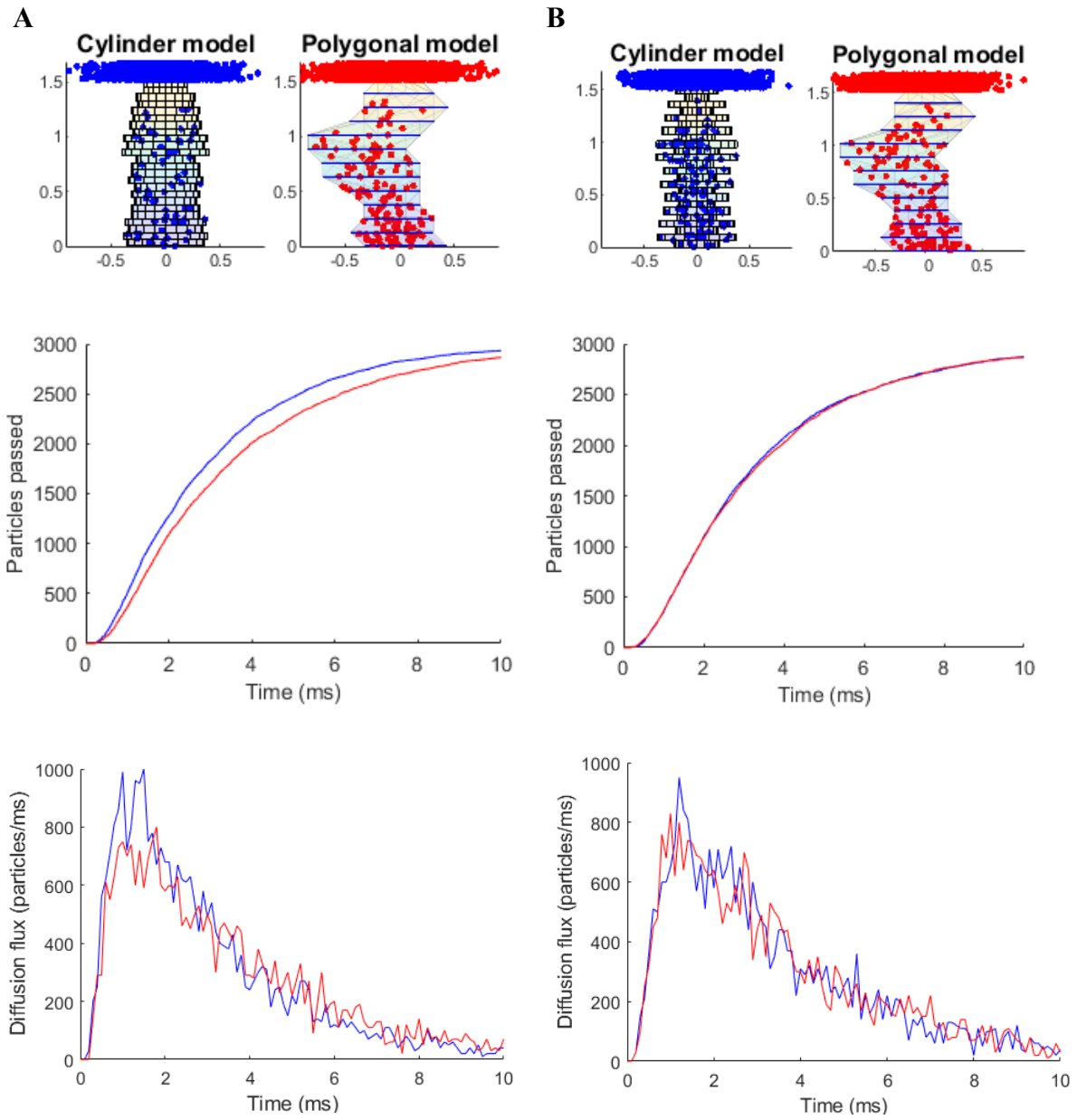


***Figure 11.*** *Comparison of the original polygonal model with the cylinder-based model A) before and B) after adjusting the coefficient of the transitional cylinders diameters to 0.6. The middle row depicts the diffusion flux, which is the number of Brownian Monte Carlo particles escaping the polygon-based process (red) and the cylinder-based process (blue) as a function of time. The bottom row depicts the diffusion flux as a function of time.*

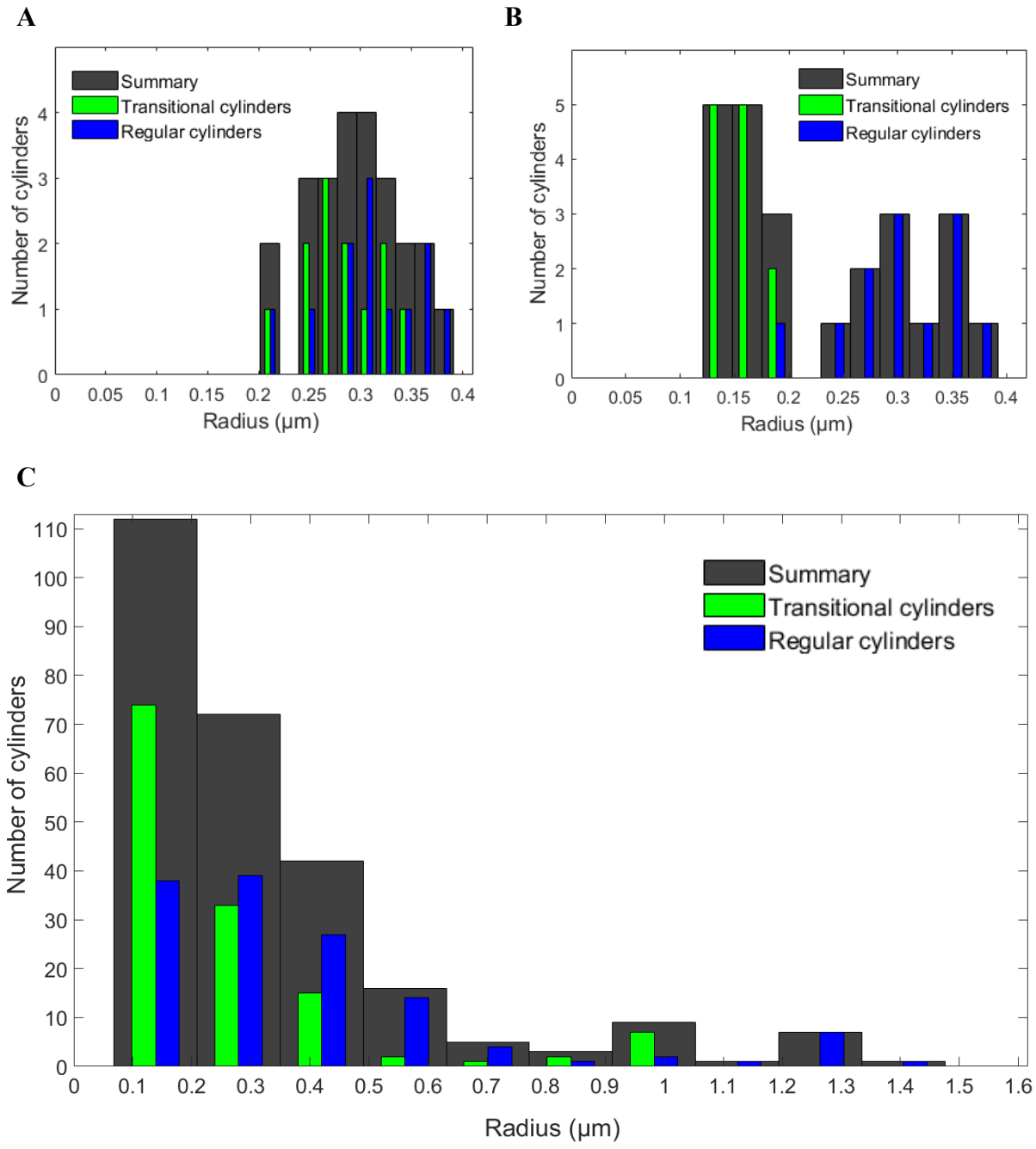


***Figure 12.*** *The cylinder radii distribution of the same nanoscopic process as in Figure 9C and 11 A) before and B) after adjusting the effective diameters of transitional cylinders from 1 to 0.6. C) Cylinder radii distribution for all twelve selected nanoprocesses pooled together. The black bars represent the combined number of both transitional and regular cylinders at different radii. The green bars represent the numbers of transitional cylinders at different radii, and the blue bars the numbers of regular cylinders at different radii.*

## 5.3 Stem tree

The Bergmann glial stem tree was built based on values found from literature with most of the values corresponding to those of age P20-P30 mice. The stem tree was built in three steps with the NEURON Cell Builder tool (Figure 13). First, a soma and one main process consisting of 16 sections and one endfoot were created. The main process including the endfoot was replicated four times and each was attached to the soma. Finally, each of the four main processes were populated with the same composition of lateral processes based on the categorization by Lippman et al. (2008) of stubby, thin, bulbous, and branching appendages. An additional very short lateral process subtype, "stem", was added in order to create a few nanoprocesses that arose close to the stem tree. The lateral processes were arranged onto the length of the main processes relatively uniformly but otherwise arbitrarily. Diameters and lengths were assigned to each section with the NEURON Cell Builder tool. The final stem tree was saved into a hoc-file to be used when composing the final model with the ASTRO tool.

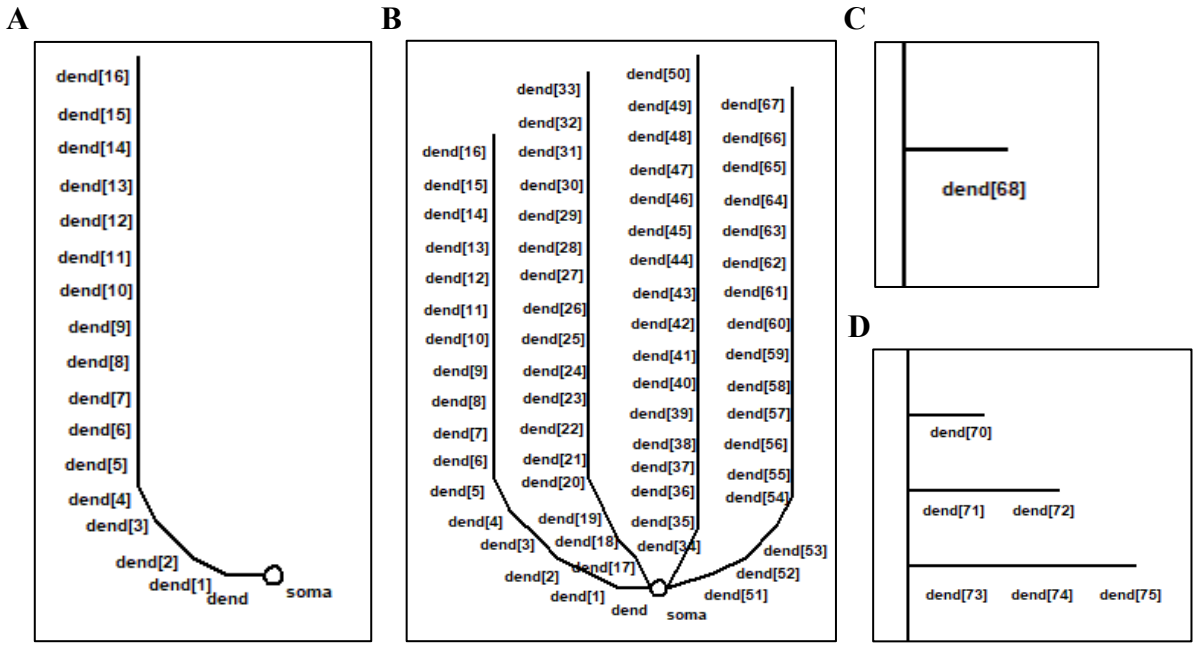


***Figure 13.*** *Building the Bergmann glial stem tree with the NEURON Cell Builder tool. The NEURON term "dend" denotes a single section. The section lengths and diameters were assigned later; here the sections are not displayed in correct proportions. A) The soma and one main process consisting of 16 sections and one endfoot created. B) The main process including the endfoot copied and attached to the soma, resulting in four identical main processes with endfeet at the tips. C) Thin, stubby, and stem lateral processes consisted of one section. D) Bulbous and branching lateral processes consisted of either one, two, or three consecutively attached sections.*

## 5.4 The complete Bergmann glial morphology

The complete Bergmann glial morphology was built by populating the stem tree with the nanoscopic processes generated based on the cylinder radii distribution. The ASTRO code was modified in such a way that only the branching, bulbous, and stem lateral processes gave rise to nanoscopic processes (Figure 14).

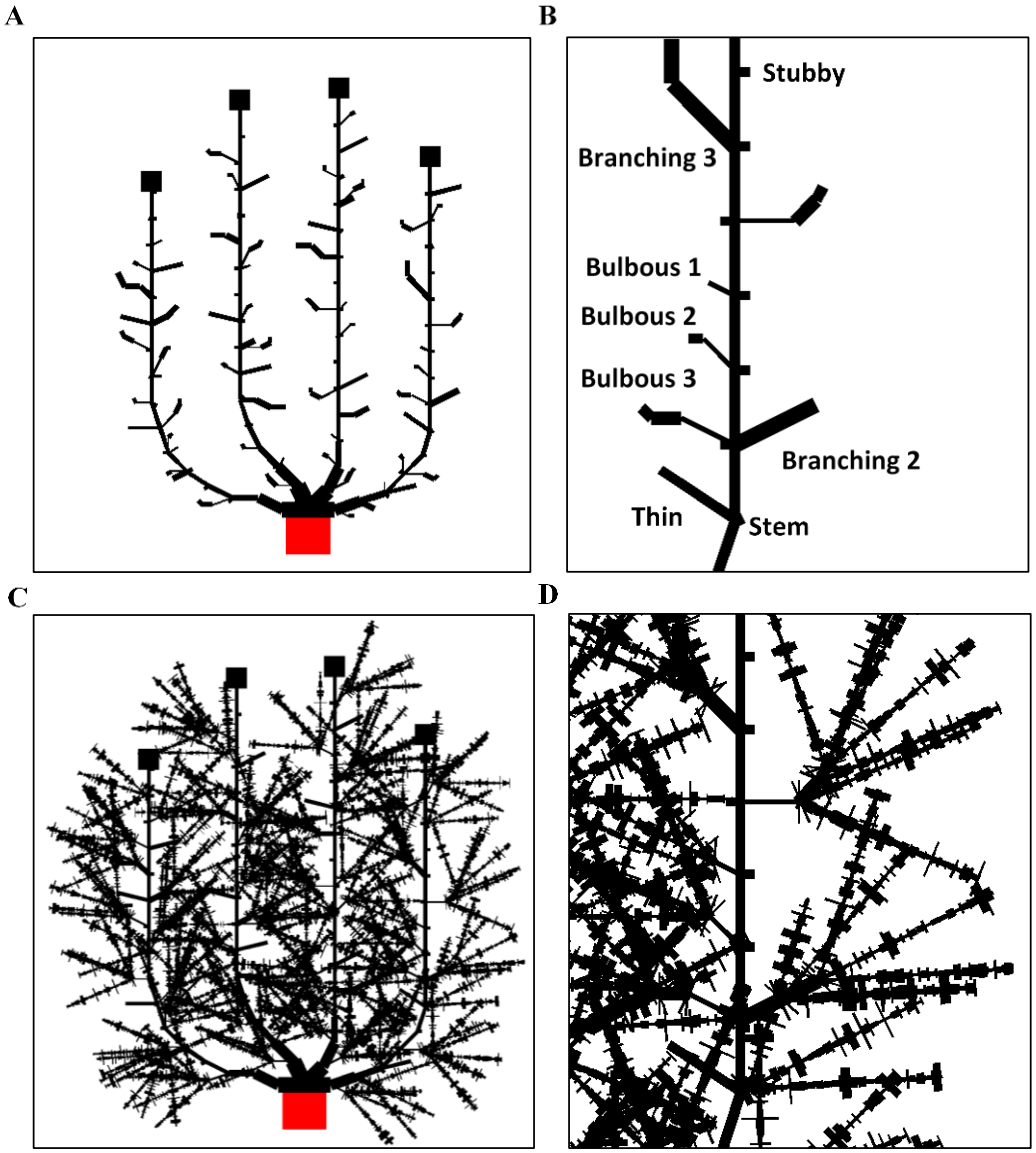


***Figure 14.*** *The Bergmann glial model A) before and C) after adding the nanoscopic processes. Closer view of the lateral processes in (A) and (C) can be seen in (B) and (D), respectively. Branching and bulbous lateral processes are comprised of 1-3 sections and stubby, thin, and stem lateral processes of single sections. Each section of bulbous, branching, and stem lateral processes give rise to three nanoprocesses. Thin and stubby lateral processes do not give rise to nanoprocesses.*

The volumetric characteristics for the model, including the total cell volume, the total cell surface area, the surface-to-volume ratio, and the tissue volume fraction were calculated automatically by ASTRO (Figure 15). The volumetric values were calculated as a function of radial distance from the soma with the assumption that the astrocyte was approximately spherical in morphology. The total cell volume was 2,137 $\mu m^3$, the total cell surface area 18,130 $\mu m^2$, the surface-to-volume ratio 13.07 $\mu m^{-1}$, and the tissue-volume fraction 0.014% (or as a natural logarithm, -8.86).

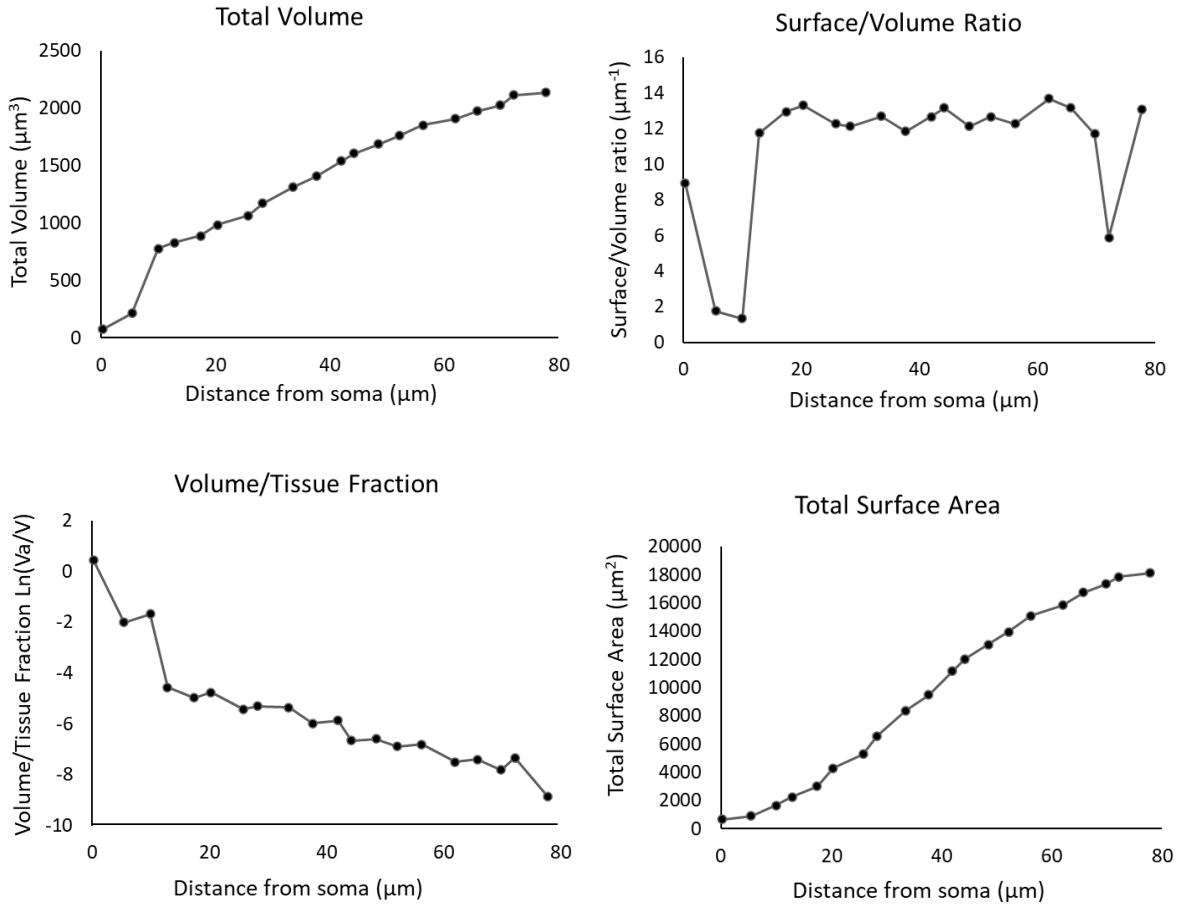


***Figure 15.*** *Morphometric characteristics of the complete Bergmann glial model as a function of radial distance from the soma. Va, volume of the astrocyte; V, volume of a sphere with the same outer diameters as the astrocyte.*

## 5.5 Calcium wave simulations

To study how the dynamics of $Ca^{2+}$ waves along the length of the Bergmann fibers is affected by the localization of lateral processes, the intracellular $Ca^{2+}$ concentration was measured from two of the main processes (Figure 16). The processes were otherwise identical except for the

arrangement of the lateral processes that slightly varied. The $Ca^{2+}$ concentration was measured from the third furthest section and the fourth closest section of the main process in each case. The $Ca^{2+}$ concentration was also measured from two types of lateral processes that give rise to nanoprocesses; bulbous and branching. The chosen bulbous and branching processes consisted of three and two sections, respectively, and were localized close to each other on the first main process. The $Ca^{2+}$ concentration was measured from the second section in each case.

The regulation of free $Ca^{2+}$ ions is important in non-excitable cells like glial cells. To study how the dynamics of the $Ca^{2+}$ wave is affected by the presence of mobile $Ca^{2+}$ buffers that bind to $Ca^{2+}$ ions, the simulations were run for ten seconds both without the mobile buffer (Figure 16A) and with a small concentration of the mobile buffer added (10 μM) (Figure 16B). Time series snapshots of the $Ca^{2+}$ wave dynamics in the Bergmann glial model for the first five seconds with and without the mobile buffer is presented in Figure 17.

The onset of intracellular $IP_3$ increase in the soma was set to 1 s and triggered the first $Ca^{2+}$ wave nearly concurrently along the length of the main processes (Figure 16 and 17). The peak times of the $Ca^{2+}$ waves for all the different measurement points seem to spread gradually the longer the simulation proceeded, as observed both with and without the mobile buffer. In the beginning of the simulation the peaks were within 1 s of each other in different measurements points, whereas towards the end of the simulation they were within 2 s of each other. The $Ca^{2+}$ concentration stayed elevated in the soma as well as in the endfeet after the first wave. The buffer slightly delayed the onset of the $Ca^{2+}$ waves, as observed in Figure 16. Without mobile buffer, an increase in the $Ca^{2+}$ concentration occurred in the soma immediately at 1 s and spread to the distal parts by around 1.5 s. The $Ca^{2+}$ waves continued to oscillate both in distal and proximal parts, but in the latter the amplitude of the waves started to slowly decrease. With the mobile buffer present, the onset of the first $Ca^{2+}$ waves were slightly delayed and the subsequent $Ca^{2+}$ waves in the proximal locations diminished very quickly, but continued to oscillate in the distal parts. The buffer reduced both the frequency and the amplitude of the $Ca^{2+}$ waves. The only exception to this was the first distal location, where the amplitude of the $Ca^{2+}$ wave was increased after adding the mobile buffer.

The dynamics of $Ca^{2+}$ waves differed between the bulbous and branching lateral process subtypes. Without the mobile buffer, $Ca^{2+}$ waves occurred less frequently in the bulbous in comparison to the branching. With the mobile buffer present, $Ca^{2+}$ waves were observed only in the branching lateral process, and not in the bulbous one.

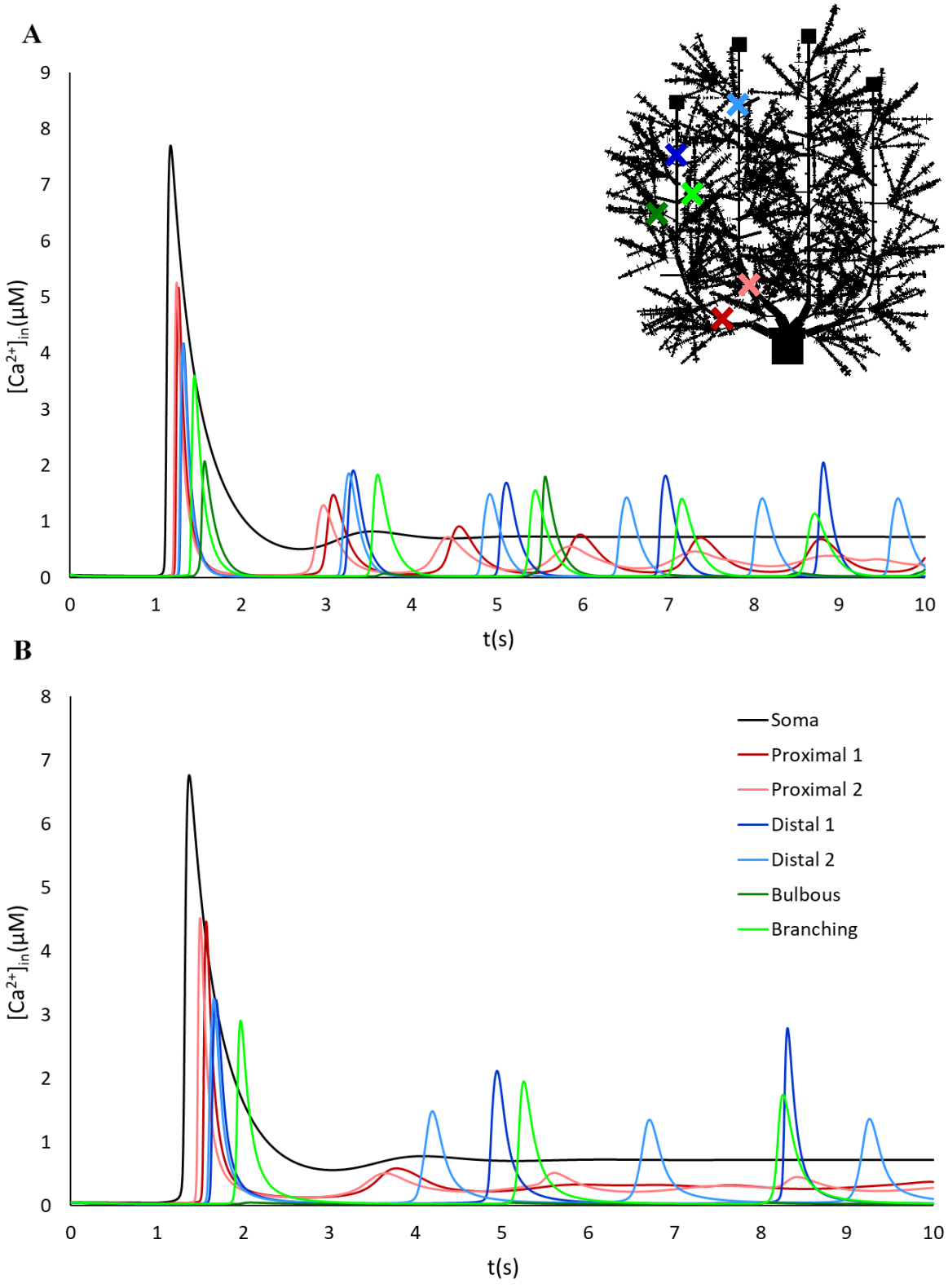


***Figure 16.*** *$Ca^{2+}$ waves A) without mobile buffer and B) with 10 μM mobile buffer added. The crosses in the Bergmann glial model indicate measurement points along two of the main processes, proximal corresponding to the $4^{th}$ and distal to the $14^{th}$ section from the soma.*

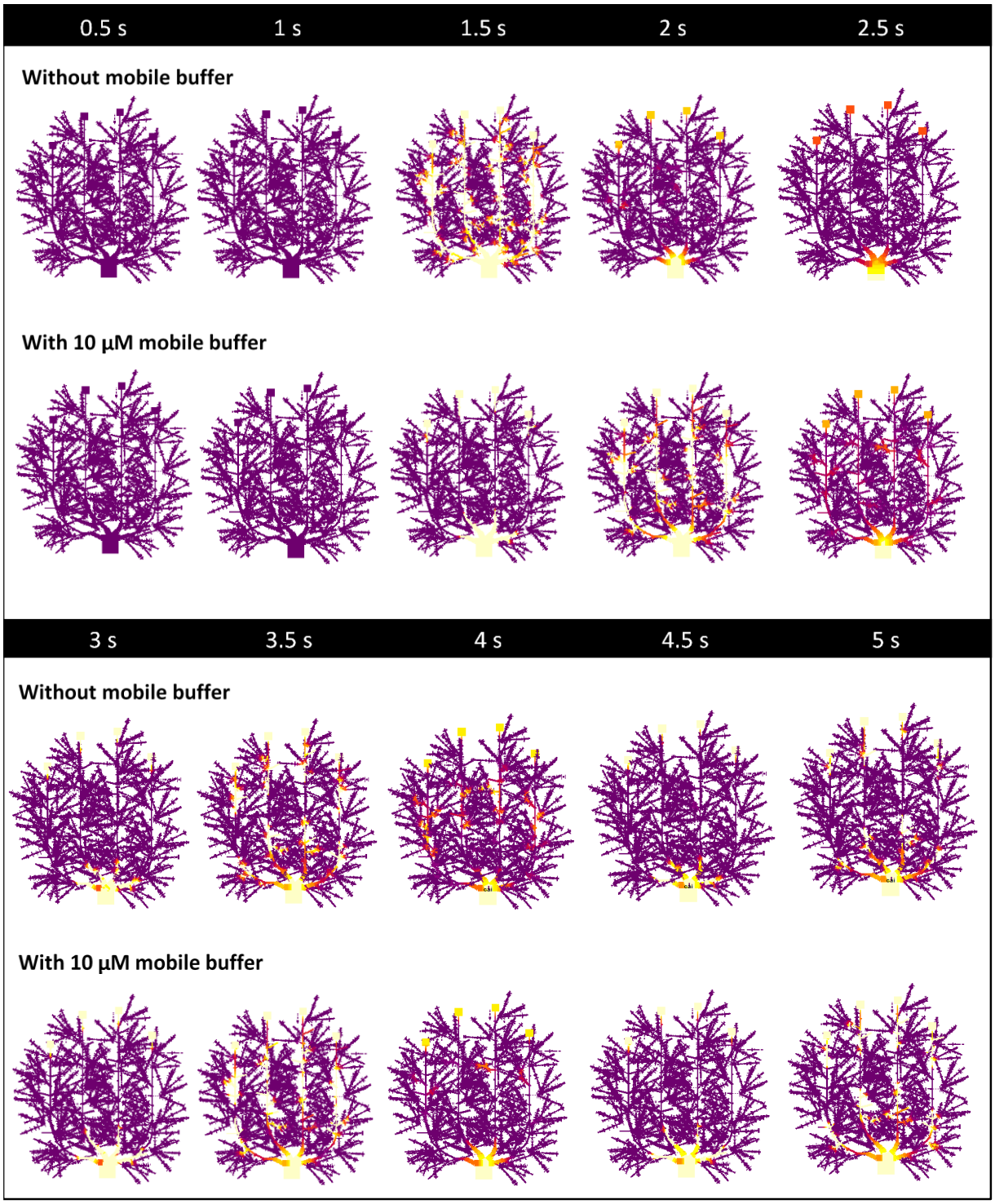


***Figure 17.*** *$Ca^{2+}$ wave time series* snapshots *without mobile buffer and with 10 µM mobile buffer added. Purple, low $Ca^{2+}$ concentration. Yellow, high $Ca^{2+}$ concentration.*

# 6. DISCUSSION

## 6.1 Appendage reconstruction

The Bergmann glial appendage was reproduced from the video file provided by Grosche et al. (1999). There were two major challenges to transform the appendage morphology from the video file into a format that could be utilized with the ASTRO Nanogeometry tool. First, a three-dimensional representation of the morphology had to be extracted from the video file. Second, the three-dimensional representation of the morphology had to be in a correct format. The first challenge was solved by using the photogrammetry tool Agisoft Metashape, with which it was possible to automatically extract the appendage morphology from the video file and create a polygonal mesh representation of it. To our knowledge, no straightforward method existed for solving the second challenge. For the point cloud to be usable in the Nanogeometry tool, the points had to be aligned in equidistant circumvents along the surface. Obtaining the correct format was finally accomplished by utilizing Blender, a 3D computer graphics software. With Blender, it was possible to create a regular grid of points onto the surface of the polygonal mesh and save the point locations into a text-file. The resulting point cloud was in the correct format for the Nanogeometry tool, with points circumventing the appendage surface in regular intervals.

Both reconstruction steps, extraction of the mesh with Agisoft Metashape and creation of the surface points with Blender, created some distortion to the shape. The ability of Agisoft Metashape to recreate the shape accurately was partly limited by the number of frames that could be extracted from the video file. Nonetheless, for the purpose of utilizing the Nanogeometry tool for selecting nanoprocesses from the reconstructed shape, it was enough that the nanoprocesses arising from the shape were correctly reconstructed. The shape as a whole was not completely accurate representation of the original Bergmann glial appendage, but the morphology of the nanoprocesses it gave rise to were roughly captured with the developed approach. Comparison of the video frames to the point cloud morphology indicated that while some of the smaller details were lost, the general shape of the nanoprocesses was relatively well preserved (see Figure 7).

## 6.2 Nanogeometry

For the diffusion simulations to work properly, the circumvents of the nanoscopic processes should comprise of around 10-20 XYZ points according to the ASTRO user guide. For the smallest nanoscopic processes arising from the Bergmann glial appendage reconstruction, the amount of points was mostly within these boundaries. However, most of the nanoscopic processes had around 20-40 XYZ points along their circumvents, and in the case of one large nanoprocess, the average was about 70 XYZ points per circumvent. The higher amount of points along the circumvents of the nanoprocesses was due to the resolution of the Blender Particle System applied onto the mesh. The value chosen for the resolution, 160x160, was a compromise between limiting the number of surface points and capturing as much of the details in the nanoprocesses as possible. As the diffusion simulations seemed to work correctly with even a larger than recommended number of points, the resolution was not decreased further. In addition, a sample of at least 15-20 nanoscopic processes should be selected for the accumulation of sufficient shape statistics, according to the ASTRO user guide. In total twelve distinct nanoscopic processes were classified as qualitatively "good" from the total of 19 nanoscopic processes that were possible to select from the morphology of the Bergmann glial appendage. According to the user guide, the shapes are considered "good" by the Nanogeometry tool if they are mathematically usable, i.e. do not have data outliers, topological confusion, or too few data points. The unusability of the seven nanoprocesses seemed to be caused primarily by too few data points or topological confusion that caused the tool not to connect the points in the circumvents correctly.

## 6.3 Stem tree

The Bergmann glial stem tree, including the soma, main processes, lateral processes, and endfeet, was built with the NEURON Cell Builder tool based on values the found for the mouse Bergmann glia. As determined by Hoogland et al. (2009) the area encompassed by the fibers of a single Bergmann glial cell in mice is about 40 µm in the transverse direction and 19 µm longitudinally. With the Cell Builder tool, however, it was possible to create the stem tree only in a two-dimensional plane. The two-dimensional representation with the correct average section lengths and diameters should still preserve the conductivity properties of the shape. In a further study, the two-dimensional morphology could be transformed into three-dimensional representation by fitting the morphology into the known three-dimensional boundaries of

Bergmann glial cells. It would then be possible to determine more accurately further morphometric properties from the shape, such as the volume-to-tissue fraction. On the other hand, an advantage of the Cell Builder tool was the possibility to draw the cell morphology in such a way that the spatiotemporal dynamics in the different parts of the modeled cell could be more easily visually distinguished.

The length and diameter of the Bergmann glial main processes were average values measured from 2-year-old mice (Siegel et al., 1991). As determined for rat Bergmann glial cells, the length of the main processes tends to increase and the diameter decrease as the animal ages (Hanke & Reichenbach, 1987). While the main processes were based on the properties of Bergmann glial cells from 2-year-old mice, the frequency of the lateral processes subtypes was based on Bergmann glia from 20-day-old mice (Lippman et al., 2008). The relative coverage by the lateral processes in rats is estimated to peak at 5 months but decreases as the animal gets older (Hanke & Reichenbach, 1987). The values in 16-day, 30-day, and 2-year-old rats were in roughly similar caliber, 39 %, 49 %, and 53 %, respectively (Hanke & Reichenbach, 1987). It could thus be postulated that the frequency of the lateral processes would be roughly the same in mice aged 20 days and 2 years. However, this does not take into account the frequency of the different subtypes. According to the study by Lippman et al (2008), the frequency of bulbous and branching appendages in comparison to the frequency of stubby and thin appendages increased as mice matured from 10-day-old to 20-day-old. It is conceivable that in 2-year-old mice, the frequency of bulbous and branching appendages in comparison to stubby and thin processes would have further increased. In addition, the main processes were built as straight cylinders with uniform diameter along their length. This is not the case in a real Bergmann glial cell; in reality, the Bergmann fibers are uneven in thickness, often twisted, and ellipsoidal rather than cylindrical (Rakic, 1971).

The lateral process subtypes and their frequencies were based on the categorization by Lippman et al (2008). The overall characteristics of the shapes were as described by Lippman et al. (2008), but the precise lengths and diameters were estimated. Important distinction was between the morphologies of bulbous and branching appendages. According to the description by Lippman et al. (2008), the bulbous lateral processes were defined with a smaller neck to which the nanoprocesses were attached. Branching lateral processes were connected to the main processes with a thicker stalk. Both of these lateral processes were modeled in three sizes, consisting of 1-3 consecutively attached sections, each of which nanoprocesses were attached to. In reality, however, these lateral processes likely have much more elaborate structures and

come in multiple different sizes. The main functional distinction between the bulbous and lateral processes may be their electrical connectivity to the main processes. The thin neck of the bulbous processes could serve to sequester the nanoprocesses it contained from the rest of the cell, while the branching lateral appendage would more readily receive the signals propagating from other parts of the cell. The stubby and thin lateral processes were modeled as simple protrusions consisting of one section with uniform diameter and length. The categorization of lateral processes by Lippman et al. (2008) did not include appendages longer than 10 μm or shapes otherwise unclassifiable to the above categories. For simplicity, these were left unmodeled. Instead, a few additional short single-section outgrowths from the stem tree, "stems", were defined to give rise to nanoprocesses close to the main processes. Each of the four main processes arising from the soma were populated with the same number and types of lateral processes. The only difference was their localization along the length of the main processes.

The endfeet were modeled as simple one section structures attached to the tips of each of the main processes. However, their morphology is much more elaborate than that (Palay & Chan-Palay, 1974), and for a more detailed cell model where endfeet-specific mechanisms are incorporated, they could be modeled in more detail.

In conclusion, the real Bergmann glial stem tree is more elaborate and uneven than the modeled stem tree, and the fibers radiate three-dimensionally from the soma instead of lying flat on one plane. As a simplification, the modeled stem tree populated with the nanoscopic processes may still be able to reproduce some of the properties specific to the elongated form of Bergmann glial cell, decorated with a heterogeneous set of lateral processes.

## 6.4 The complete Bergmann glial morphology

The final Bergmann glial morphology was built by populating the stem tree with the nanoscopic processes based on cylinder radii distribution with the ASTRO tool. As the Bergmann glial stem processes seem to give rise to the nanoprocesses mainly via their lateral processes (Grosche et al., 1999; Palay & Chan-Palay, 1974), the functionality of the ASTRO tool was modified in such a way that the tool attached the nanoprocesses only onto a specified set of sections. By default without the modifications, the ASTRO tool would have attached nanoprocesses to each section except the soma. With the implemented modification, the

nanoprocesses were attached only to the bulbous, branching, and stem appendages, but not directly onto the stem tree nor to the stubby or thin appendages.

The metric that was used for defining the leaves per stalk of the nanoprocesses was the surface-to-volume ratio that has been estimated to be about 13 $\mu m^{-1}$ for Bergmann glia (Grosche et al., 1999). The surface-to-volume ratio was automatically calculated by ASTRO among other morphometric values, including the volume, surface area, and tissue-to-volume fraction. For the Bergmann glial model implemented in this study only the surface-to-volume ratio was an applicable metric. The adjusted number of leaves was 24 per stalk which produced a final surface-to-volume ratio of 13.07 $\mu m^{-1}$ for the Bergmann glial model.

The tissue-to-volume fraction of a single Bergmann glial cell is estimated to be about 17.5% (Grosche et al., 2002), much higher than the value provided by the ASTRO's morphometric readout (0.014%). The very low tissue-to-volume fraction calculated for the Bergmann glial cell model is explained by the fact that ASTRO calculates the tissue-to-volume fraction of the astrocyte by comparing the astrocyte volume to the volume of a sphere radiating from the soma. As the Bergmann glial fibers elongate longitudinally into one direction, this approach clearly does not work for the developed cell mode. A different approach should be implemented for determining the tissue-volume fraction of the Bergmann glial cell. This, however, would have been difficult to determine accurately for the created morphology, since the orientation and total width taken by the four stem processes was approximated with the NEURON Cell Builder tool as a two-dimensional stem tree. Determining accurately the tissue-to-volume fraction of the modeled Bergmann glial cell would require it to be adjusted to the three-dimensional boundaries it is experimentally found in (Hoogland et al., 2009).

The other morphometric values of the readout, including the volume and surface area (and the surface-to-volume ratio), were applicable to Bergmann glia, as they did not depend on the volume of the background shape. From the literature review no estimation for the volume of a mouse Bergmann glial cell was found, but the volume of a rat Bergmann glial cell is estimated to be about 3,600 $\mu m^3$ (Reichenbach et al., 1995). As the rat Bergmann glial cell is about two times as long as mouse Bergmann glial cells and has a similar fractal dimension (Siegel et al., 1991), the total volume of 2,137 $\mu m^3$ of the reconstructed Bergmann glial cell seems reasonable.

In conclusion, the ASTRO tool was suitable for creating a whole-cell model for Bergmann glial cell after modifications. With modifications to how the tissue-to-volume fraction is calculated, the tool would be even better suited for Bergmann glia. The other cerebellar astroglial cells,

velate astrocytes and fibrous astrocytes, are rounded in shape and could conceivably be (if adequate morphometric data were available) modeled with the ASTRO tool without further modifications to the tool.

## 6.5 Functionality

The biophysical mechanisms present in the astroglia-specific simulations provided by the ASTRO tool, including the simulations for $Ca^{2+}$ waves, microscopic $Ca^{2+}$ dynamics, membrane biophysics of glutamate transport, and dynamics of intra- and extracellular $K^{+}$, are common to astrocytes in general (Verkhratsky & Nedergaard, 2018). As reviewed for the cerebellar astroglial cells, most of the biophysical mechanisms used in these simulations are present in Bergmann glia. The only exception is the L-type $Ca^{2+}$ channel that has not been detected in Bergmann glia nor is it commonly found in other astrocytes (Verkhratsky & Nedergaard, 2018). Instead of mediating the plasmalemmal $Ca^{2+}$ flux through $Ca^{2+}$ channels, Bergmann glia may mediate it via ionotropic receptors; in contrast to other astrocytes whose AMPARs are $Ca^{2+}$ impermeable, Bergmann glia has AMPARs that lack the second subunit and thus are permeable to $Ca^{2+}$ (Muller et al., 1992). The literature review conducted in this work provided a comprehensive background on the membrane proteins present in cerebellar astroglial cells and their single-cell localization. In future studies, the morphologically-detailed Bergmann glial model implemented here could be equipped with different biophysical mechanisms for simulating a wide variety of different biological processes.

The preset parameters for the biophysical mechanism in the ASTRO tool were optimized for hippocampal astrocytes, which differ from Bergmann glial cells considerably both in form and function (Verkhratsky & Nedergaard, 2018). For a biophysically more accurate model, the parameters should be optimized for Bergmann glial cells.

## 6.6 Calcium dynamics

The ASTRO tool provides an assortment of simulations specifically designed for simulating the various mechanisms of astroglial cells. Within the ASTRO simulation platform, it is possible to adjust both the morphometric and biophysical properties of the modeled astrocyte and perform simulations for $Ca^{2+}$ waves, microscopic $Ca^{2+}$ dynamics, membrane biophysics of glutamate transport, dynamics of intra- and extracellular $K^{+}$, as well as the FRAP. With

adjustments to the parameter values, the simulations could possibly elucidate some of the functions of Bergmann glial cells that are difficult to study experimentally, such as the detailed spatiotemporal dynamics of $Ca^{2+}$, glutamate, or $K^{+}$. As the developed Bergmann glial model lacked the parameter optimization specific to Bergmann glia, the simulation was mainly utilized for the purposes of studying the effect of the morphology on $Ca^{2+}$ dynamics. The simulation chosen for more detailed analysis was the $Ca^{2+}$ wave simulation.

The purpose of the $Ca^{2+}$ simulations was to study the effect of morphology on the spatiotemporal dynamics of $Ca^{2+}$ within the modeled Bergmann glial cell. $Ca^{2+}$ simulations with and without a mobile buffer present were conducted in order to probe the buffering capacity of the modeled Bergmann glial cell. The main processes were all identical and had the same lateral processes. The only difference was the localization of the lateral processes along the length of the main processes, as well as the nanogeometry that was stochastically created.

$Ca^{2+}$ increases measured from the proximal locations attenuated faster than those measured from the distal locations, both with and without the mobile buffer. In the distal locations, the $Ca^{2+}$ waves continued to propagate. The occurrence of $Ca^{2+}$ waves in one of the processes was slightly delayed in comparison to the other, both when measured from proximal and distal locations, and the difference between the wave occurrences between the two main processes grew larger as the $Ca^{2+}$ wave propagated. This was likely due to the localization of the lateral processes. It is difficult, however, to ascertain what exactly in their arrangement caused the delay in the second main process. Further, more detailed study on the effect of the arrangement of the appendages would require a more systematic approach when populating the main processes with appendages. Nevertheless, the simulations conducted in this study provided the indication that the propagation of the $Ca^{2+}$ waves is affected by the localization of the lateral processes and could be worth studying in more detail.

The mobile buffer reduced both the frequency and the amplitude of the $Ca^{2+}$ waves. The only exception to this was the distal measurement from one of the main branches, where the amplitude of the $Ca^{2+}$ wave was increased after adding the mobile buffer. The lower occurrence of $Ca^{2+}$ waves without mobile buffer present in bulbous appendages in comparison to the branching appendages was most likely caused by the thinner and slightly longer neck that connected the appendage to the stem tree. With 10 μm of mobile buffer present, $Ca^{2+}$ waves failed completely to occur in the bulbous appendage but still occurred in the branching appendage. The chosen bulbous and branching appendages were located in the same main process and close to

each other, the branching appendage being slightly more distal to the soma. The effect of the location on the difference observed in the $Ca^{2+}$ dynamics in the two appendage subtypes was thus likely relatively small.

In conclusion, the $Ca^{2+}$ dynamics across main processes of the modeled Bergmann glial cells are affected by the localization of the lateral processes and differ between the lateral processes of bulbous and branching subtypes. The bulbous appendages may altogether be sequestered from the propagating $Ca^{2+}$ waves if the concentration of mobile buffer is high enough.

# 7. CONCLUSIONS

Even though no three-dimensional cell morphologies for cerebellar astroglial cells were available in the public databases, it was possible to create a detailed whole-cell model for a Bergmann glial cell by utilizing morphometric data from literature and a video-file of a single astroglial appendage (Grosche et al., 1999). The model construction included four stages. First, the Bergmann glial appendage was reconstructed from the video file by using AgiSoft Metashape and Blender. Second, nanoscopic processes were selected from the appendage and transformed into NEURON and ASTRO -compatible cylindrical structures. Third, the Bergmann glial stem tree was built with NEURON Cell Builder tool based on values from the literature. Fourth, the complete single-cell model was assembled in the novel astrocyte simulation tool ASTRO by populating the stem tree with the nanoscopic processes. The functionality of the ASTRO tool was extended in this study to better suit the modeling of the Bergmann glial cell. The final model was used for simulating $Ca^{2+}$ waves with and without mobile buffers. The spatiotemporal pattern of $Ca^{2+}$ wave dynamics across the Bergmann glial morphology was influenced by the localization and shape of the lateral processes. The mobile buffers reduced both the amplitude and frequency of $Ca^{2+}$ waves.

# 8. REFERENCES


Adamaszek, M., D'Agata, F., Ferrucci, R., Habas, C., Keulen, S., Kirkby, K. C., Leggio, M., Mariën, P., Molinari, M., Moulton, E., Orsi, L., Van Overwalle, F., Papadelis, C., Priori, A., Sacchetti, B., Schutter, D. J., Styliadis, C., & Verhoeven, J. (2017). Consensus Paper: Cerebellum and Emotion. *Cerebellum*, *16*(2), 552–576. https://doi.org/10.1007/s12311-016-0815-8

Apps, R., & Hawkes, R. (2009). Cerebellar cortical organization: A one-map hypothesis. *Nature Reviews Neuroscience*, *10*(9), 670–681. https://doi.org/10.1038/nrn2698

Apps, R., Hawkes, R., Aoki, S., Bengtsson, F., Brown, A. M., Chen, G., Ebner, T. J., Isope, P., Jörntell, H., Lackey, E. P., Lawrenson, C., Lumb, B., Schonewille, M., Sillitoe, R. V., Spaeth, L., Sugihara, I., Valera, A., Voogd, J., Wylie, D. R., & Ruigrok, T. J. H. (2018). Cerebellar Modules and Their Role as Operational Cerebellar Processing Units. *Cerebellum*, *17*(5), 654–682. https://doi.org/10.1007/s12311-018-0952-3

Araque, A., Parpura, V., Sanzgiri, R. P., & Haydon, P. G. (1999). Tripartite synapses: Glia, the unacknowledged partner. *Trends in Neurosciences*, *22*(5), 208–215. https://doi.org/10.1016/S0166-2236(98)01349-6

Araujo, A. P. B., Carpi-Santos, R., & Gomes, F. C. A. (2019). The Role of Astrocytes in the Development of the Cerebellum. *Cerebellum*, *18*, 1017–1035. https://doi.org/10.1007/s12311-019-01046-0

Barros, L. F., Courjaret, R., Jakoby, P., Loaiza, A., Lohr, C., & Deitmer, J. W. (2009). Preferential transport and metabolism of glucose in Bergmann glia over Purkinje cells: A multiphoton study of cerebellar slices. *Glia*, *57*(9), 962–970. https://doi.org/10.1002/glia.20820

Baude, A., Molnar, E., Latawiec, D., McIlhinney, R. A. J., & Somogyi, P. (1994). Synaptic and nonsynaptic localization of the GluR1 subunit of the AMPA- type excitatory amino acid receptor in the rat cerebellum. *Journal of Neuroscience*, *14*(5 I), 2830–2843. https://doi.org/10.1523/jneurosci.14-05-02830.1994

Beierlein, M., & Regehr, W. G. (2006). Brief bursts of parallel fiber activity trigger calcium

signals in Bergmann glia. *Journal of Neuroscience*, *26*(26), 6958–6967. https://doi.org/10.1523/JNEUROSCI.0613-06.2006

Bergles, D. E., Dzubay, J. A., & Jahr, C. E. (1997). Glutamate transporter currents in Bergmann glial cells follow the time course of extrasynaptic glutamate. *Proceedings of the National Academy of Sciences of the United States of America*, *94*(26), 14821–14825. https://doi.org/10.1073/pnas.94.26.14821

Blackstone, C. D., Moss, S. J., Martin, L. J., Levey, A. I., Price, D. L., & Huganir, R. L. (1992). Biochemical Characterization and Localization of a Non-N-Methyl-D-Aspartate Glutamate Receptor in Rat Brain. *Journal of Neurochemistry*, *58*(3), 1118–1126. https://doi.org/10.1111/j.1471-4159.1992.tb09370.x

Blanz, J., Schweizer, M., Auberson, M., Maier, H., Muenscher, A., Hübner, C. A., & Jentsch, T. J. (2007). Leukoencephalopathy upon disruption of the chloride channel ClC-2. *Journal of Neuroscience*, *27*(24), 6581–6589. https://doi.org/10.1523/JNEUROSCI.0338-07.2007

Boisvert, M. M., Erikson, G. A., Shokhirev, M. N., & Allen, N. J. (2018). The Aging Astrocyte Transcriptome from Multiple Regions of the Mouse Brain. *Cell Reports*, *22*(1), 269–285. https://doi.org/10.1016/j.celrep.2017.12.039

Brasko, C., Hawkins, V., De La Rocha, I. C., & Butt, A. M. (2017). Expression of Kir4.1 and Kir5.1 inwardly rectifying potassium channels in oligodendrocytes, the myelinating cells of the CNS. *Brain Structure and Function*, *222*(1), 41–59. https://doi.org/10.1007/s00429-016-1199-8

Carnevale, N. T., & Hines, M. L. (2006). The NEURON book. In *The NEURON Book*. Cambridge University Press. https://doi.org/10.1017/CBO9780511541612

Castejon, O. J., Dailey, M., Apkarian, R. P., & Castejon, H. V. (1999). Correlative microscopy of cerebellar Bergmann glial cells. *Journal of Submicroscopic Cytology and Pathology*, *18*, 2002. https://doi.org/10.1017.S1431927602107057

Cerminara, N. L., Lang, E. J., Sillitoe, R. V., & Apps, R. (2015). Redefining the cerebellar cortex as an assembly of non-uniform Purkinje cell microcircuits. *Nature Reviews Neuroscience*, *16*(2), 79–93. https://doi.org/10.1038/nrn3886

Chan-Palay, V., & Palay, S. L. (1972). The form of velate astrocytes in the cerebellar cortex of monkey and rat: High voltage electron microscopy of rapid Golgi preparations. *Zeitschrift*

*Für Anatomie Und Entwicklungsgeschichte*, *138*(1), 1–19. https://doi.org/10.1007/BF00519921

Chaudhry, F. A., Lehre, K. P., Lookeren Campagne, M. van, Ottersen, O. P., Danbolt, N. C., & Storm-Mathisen, J. (1995). Glutamate transporters in glial plasma membranes: Highly differentiated localizations revealed by quantitative ultrastructural immunocytochemistry. *Neuron*, *15*(3), 711–720. https://doi.org/10.1016/0896-6273(95)90158-2

Chrobak, A. A., & Soltys, Z. (2017). Bergmann Glia, long-term depression, and autism spectrum disorder. *Molecular Neurobiology*, *54*(2), 1156–1166. https://doi.org/10.1007/s12035-016-9719-3

D'Angelo, E., Antonietti, A., Casali, S., Casellato, C., Garrido, J. A., Luque, N. R., Mapelli, L., Masoli, S., Pedrocchi, A., Prestori, F., Rizza, M. F., & Ros, E. (2016). Modeling the cerebellar microcircuit: New strategies for a long-standing issue. *Frontiers in Cellular Neuroscience*, *10*(176), 1–29. https://doi.org/10.3389/fncel.2016.00176

D'Angelo, E., & Casali, S. (2013). Seeking a unified framework for cerebellar function and dysfunction: From circuit operations to cognition. *Frontiers in Neural Circuits*, *6*(116), 1–23. https://doi.org/10.3389/fncir.2012.00116

De Blas, A. L. (1984). Monoclonal antibodies to specific astroglial and neuronal antigens reveal the cytoarchitecture of the Bergmann glia fibers in the cerebellum. *Journal of Neuroscience*, *4*(1), 265–273. https://doi.org/10.1523/jneurosci.04-01-00265.1984

Douyard, J., Shen, L., Huganir, R. L., & Rubio, M. E. (2007). Differential neuronal and glial expression of GluR1 AMPA receptor subunit and the scaffolding proteins SAP97 and 4.1N during rat cerebellar development. *Journal of Comparative Neurology*, *502*(2007), 141–156. https://doi.org/10.1002/cne

Dzubay, J. A., & Jahr, C. E. (1999). The concentration of synaptically released glutamate outside of the climbing fiber-Purkinje cell synaptic cleft. *Journal of Neuroscience*, *19*(13), 5265–5274. https://doi.org/10.1523/jneurosci.19-13-05265.1999

Fañanas, J. R. y. (1916). Contribucion al estudo de la neuroglia del cerebelo. *Trabajos de Los Laboratorios de Investigaciones Biológicas (Madrid)*, *14*, 163–179.

Farmer, W. T., Abrahamsson, T., Chierzi, S., Lui, C., Zaelzer, C., Jones, E. V., Ponroy Bally, B., Chen, G. G., Théroux, J.-F. F., Peng, J., Bourque, C. W., Charron, F., Ernst, C.,

Sjöström, P. J., Murai, K. K., Bally, B. P., Chen, G. G., Théroux, J.-F. F., Peng, J., … Murai, K. K. (2016). Neurons diversify astrocytes in the adult brain through sonic hedgehog signaling. *Science*, *351*(6275), 849–854. https://doi.org/10.1126/science.aab3103

Fink, C. C., Slepchenko, B., Moraru, I. I., Watras, J., Schaff, J. C., & Loew, L. M. (2000). An image-based model of calcium waves in differentiated neuroblastoma cells. *Biophysical Journal*, *79*(1), 163–183. https://doi.org/10.1016/S0006-3495(00)76281-3

Fisher, M., Trimmer, P., & Ruthel, G. (1993). Bergmann glia require continuous association with Purkinje cells for normal phenotype expression. *Glia*, *8*, 172–182.

Goertzen, A., & Veh, R. W. (2018). Fañanas cells—the forgotten cerebellar glia cell type: Immunocytochemistry reveals two potassium channel-related polypeptides, Kv2.2 and Calsenilin (KChIP3) as potential marker proteins. *Glia*, *66*(10), 2200–2208. https://doi.org/10.1002/glia.23478

Golgi, C. (1885). Sulla fina anatomia degli organi centrali del sistema nervoso VIII. Tessuto interstiziale degli organi nervosi centrali (Neuroglia). *Rivista Sperimentale Di Freniatria*, *11*, 72–123.

Grosche, J., Kettenmann, H., & Reichenbach, A. (2002). Bergmann glial cells form distinct morphological structures to interact with cerebellar neurons. *Journal of Neuroscience Research*, *68*(2), 138–149. https://doi.org/10.1002/jnr.10197

Grosche, J., Matyash, V., Möller, T., Verkhratsky, A., Reichenbach, A., & Kettenmann, H. (1999). Microdomains for neuron-glia interaction: Parallel fiber signaling to Bergmann glial cells. *Nature Neuroscience*, *2*(2), 139–143. https://doi.org/10.1038/5692

Habbas, S., Ango, F., Daniel, H., & Galante, M. (2011). Purinergic signaling in the cerebellum: Bergmann glial cells express functional ionotropic P2X7 receptors. *Glia*, *59*(12), 1800–1812. https://doi.org/10.1002/glia.21224

Hanke, S., & Reichenbach, A. (1987). Quantitative-morphometric aspects of bergmann glial (Golgi epithelial) cell development in rats - A golgi study. *Anatomy and Embryology*, *177*(2), 183–188. https://doi.org/10.1007/BF00572543

Hernjak, N., Slepchenko, B. M., Fernald, K., Fink, C. C., Fortin, D., Moraru, I. I., Watras, J., & Loew, L. M. (2005). Modeling and analysis of calcium signaling events leading to long-

term depression in cerebellar Purkinje cells. *Biophysical Journal*, *89*(6), 3790–3806. https://doi.org/10.1529/biophysj.105.065771

Hines, M. L., & Carnevale, N. T. (2001). NEURON: a tool for neuroscientists. *The Neuroscientist : A Review Journal Bringing Neurobiology, Neurology and Psychiatry*, *7*(2), 123–135. https://doi.org/10.1177/107385840100700207

Hirrlinger, P. G., Wurm, A., Hirrlinger, J., Bringmann, A., & Reichenbach, A. (2008). Osmotic swelling characteristics of glial cells in the murine hippocampus, cerebellum, and retina in situ. *Journal of Neurochemistry*, *105*(4), 1405–1417. https://doi.org/10.1111/j.1471-4159.2008.05243.x

Holtzclaw, L. A., Pandhit, S., Bare, D. J., Mignery, G. A., & Russell, J. T. (2002). Astrocytes in adult rat brain express type 2 inositol 1,4,5-trisphosphate receptors. *GLIA*, *39*(1), 69–84. https://doi.org/10.1002/glia.10085

Hoogland, T. M., & Kuhn, B. (2010). Recent developments in the understanding of astrocyte function in the Cerebellum in vivo. *Cerebellum*, *9*(3), 264–271. https://doi.org/10.1007/s12311-009-0139-z

Hoogland, T. M., Kuhn, B., Gobel, W., Huang, W., Nakai, J., Helmchen, F., Flint, J., & Wang, S. S.-H. (2009). Radially expanding transglial calcium waves in the intact cerebellum. *Proceedings of the National Academy of Science*, *106*(9), 3496–3501. https://doi.org/10.1073/pnas.0809269106

Huang, H., Barakat, L., Wang, D., & Bordey, A. (2004). Bergmann glial GlyT1 mediates glycine uptake and release in mouse cerebellar slices. *Journal of Physiology*, *560*(3), 721–736. https://doi.org/10.1113/jphysiol.2004.067801

Iino, M., Goto, K., Kakegawa, W., Okado, H., Sudo, M., Ishiuchi, S., Miwa, A., Takayasu, Y., Saito, I., Tsuzuki, K., & Ozawa, S. (2001). Glia-synapse interaction through Ca2+-permeable AMPA receptors in Bergmann glia. *Science*, *292*(5518), 926–929. https://doi.org/10.1126/science.1058827

Keto, L. & Manninen, T. (2020). Morphologically-detailed reconstruction of cerebellar glial cells. BMC Neuroscience, 21(Suppl 1): P124, Conference Abstract: 29th Annual Computational Neuroscience Meeting (CNS*2020, Online), 18.-22.07.2020.

Kirischuk, S., Kettenmann, H., & Verkhratsky, A. (1997). Na+/Ca2+ exchanger modulates

kainate-triggered Ca2+ signaling in Bergmann glial cells in situ. *The FASEB Journal*, *11*(7), 566–572. https://doi.org/10.1096/fasebj.11.7.9212080

Kirischuk, Sergej, Tuschick, S., Verkhratsky, A., & Kettenmann, H. (1996). Calcium signalling in mouse Bergmann glial cells mediated by α1-adrenoreceptors and H1 histamine receptors. *European Journal of Neuroscience*, *8*, 1198–1208. https://doi.org/10.1111/j.1460-9568.1996.tb01288.x

Kiyoshi, C. M., Du, Y., Zhong, S., Wang, W., Taylor, A. T., Xiong, B., Ma, B., Terman, D., & Zhou, M. (2018). Syncytial isopotentiality: A system-wide electrical feature of astrocytic networks in the brain. *Glia*, *66*(12), 2756–2769. https://doi.org/10.1002/glia.23525

Koirala, S., & Corfas, G. (2010). Identification of novel glial genes by single-cell transcriptional profiling of Bergmann glial cells from mouse cerebellum. *PLoS ONE*, *5*(2). https://doi.org/10.1371/journal.pone.0009198

Koziol, L. F., Budding, D., Andreasen, N., D'Arrigo, S., Bulgheroni, S., Imamizu, H., Ito, M., Manto, M., Marvel, C., Parker, K., Pezzulo, G., Ramnani, N., Riva, D., Schmahmann, J., Vandervert, L., & Yamazaki, T. (2014). Consensus paper: The cerebellum's role in movement and cognition. *Cerebellum*, *13*(1), 151–177. https://doi.org/10.1007/s12311-013-0511-x

Kulik, A., Haentzsch, A., Lückermann, M., Reichelt, W., & Ballanyi, K. (1999). Neuron-glia signaling via α1 adrenoceptor-mediated Ca2+ release in Bergmann glial cells in situ. *Journal of Neuroscience*, *19*(19), 8401–8408. https://doi.org/10.1523/jneurosci.19-19-08401.1999

Lee, S., Yoon, B. E., Berglund, K., Oh, S. J., Park, H., Shin, H. S., Augustine, G. J., & Lee, C. J. (2010). Channel-mediated tonic GABA release from glia. *Science*, *330*(6005), 790–796. https://doi.org/10.1126/science.1184334

Lehre, K. P., & Danbolt, N. C. (1998). The number of glutamate transport subtype molecules at glutamatergic synapses: Chemical and stereological quantification in young adult rat brain. *Journal of Neuroscience*, *18*(21), 8751–8757. https://doi.org/10.1523/jneurosci.18-21-08751.1998

Lehre, K. R., & Rusakov, D. A. (2002). Asymmetry of glia near central synapses favors presynaptically directed glutamate escape. *Biophysical Journal*, *83*(1), 125–134. https://doi.org/10.1016/S0006-3495(02)75154-0

Leonoudakis, D., Mailliard, W. S., Wingerd, K. L., Clegg, D. O., & Vandenberg, C. A. (2001). Inward rectifier potassium channel Kir2.2 is associated with synapse-associated protein SAP97. *Journal of Cell Science*, *114*(5), 987–998.

Lippman, J. J., Lordkipanidze, T., Buell, M. E., Yoon, S. O., & Dunaevsky, A. (2008). Morphogenesis and regulation of Bergmann glial processes during Purkinje cell dendritic spine ensheathment and synaptogenesis. *Glia*, *56*(13), 1463–1477. https://doi.org/10.1002/glia.20712

Luque, J. M., & Richards, J. G. (1995). Expression of NMDA 2B receptor subunit mRNA in Bergmann glia. *Glia*, *13*, 228–232.

Manninen, T., Havela, R., & Linne, M.-L. (2019). *Computational Models of Astrocytes and Astrocyte–Neuron Interactions: Characterization, Reproducibility, and Future Perspectives* (pp. 423–454). Springer, Cham. https://doi.org/10.1007/978-3-030-00817-8_16

Manninen, T., Havela, R., & Linne, M. L. (2018). Computational models for calcium-mediated astrocyte functions. In *Frontiers in Computational Neuroscience* (Vol. 12, p. 14). Frontiers Media S.A. https://doi.org/10.3389/fncom.2018.00014

Mathiesen, C., Brazhe, A., Thomsen, K., & Lauritzen, M. (2013). Spontaneous calcium waves in Bergman glia increase with age and hypoxia and may reduce tissue oxygen. *Journal of Cerebral Blood Flow and Metabolism*, *33*(2), 161–169. https://doi.org/10.1038/jcbfm.2012.175

Matyash, M., Matyash, V., Nolte, C., Sorrentino, V., Kettenmann, H., & Neuroscience, C. (2001). Requirement of functional ryanodine receptor type 3 for astrocyte migration. *The FASEB Journal*. https://doi.org/10.1096/fj.01-0380fje

McDougal, R. A., Morse, T. M., Carnevale, T., Marenco, L., Wang, R., Migliore, M., Miller, P. L., Shepherd, G. M., & Hines, M. L. (2017). Twenty years of ModelDB and beyond: Building essential modeling tools for the future of neuroscience. *J Comput Neurosci*, *42*(2), 1–10. https://doi.org/10.1007/s10827-016-0623-7.Twenty

Miras-Portugal, M. T., Menéndez-Méndez, A., Gómez-Villafuertes, R., Ortega, F., Delicado, E. G., Perez-Sen, R., & Gualix, J. (2019). Physiopathological role of the vesicular nucleotide transporter (VNUT) in the central nervous system: relevance of the vesicular nucleotide release as a potential therapeutic target. *Frontiers in Cellular Neuroscience*,

*13*(May), 1–15. https://doi.org/10.3389/fncel.2019.00224

Mitchell, S. J., & Silver, R. A. (2000). GABA spillover from single inhibitory axons suppresses low-frequency excitatory transmission at the cerebellar glomerulus. *Journal of Neuroscience*, *20*(23), 8651–8658. https://doi.org/10.1523/jneurosci.20-23-08651.2000

Morara, S., Brecha, N. C., Marcotti, W., Provini, L., & Rosina, A. (1996). Neuronal and glial localization of the GABA transporter GAT-1 in the cerebellar cortex. *NeuroReport*, *7*(18), 2993–2996. https://doi.org/10.1097/00001756-199611250-00039

Mugnaini, E., Sekerková, G., & Martina, M. (2011). The unipolar brush cell: A remarkable neuron finally receiving deserved attention. In *Brain Research Reviews* (Vol. 66, Issues 1–2, pp. 220–245). Elsevier. https://doi.org/10.1016/j.brainresrev.2010.10.001

Muller, T., Fritschy, J. M., Grosche, J., Pratt, G. D., Mohler, H., & Kettenmann, H. (1994). Developmental regulation of voltage-gated K+ channel and GABA(A) receptor expression in Bergmann glial cells. *Journal of Neuroscience*, *14*(5 I), 2503–2514. https://doi.org/10.1523/jneurosci.14-05-02503.1994

Muller, T., Möller, T., Berger, T., Schnitzer, J., & Kettenmann, H. (1992). Calcium Entry Through Kainate Receptors and Resulting Potassium-Channel Blockade in Bergmann Glial Cells. *Science*, *256*(5063), 1563–1566. https://doi.org/10.1126/science.1317969

Müller, T., Möller, T., Neuhaus, J., & Kettenmann, H. (1996). Electrical coupling among Bergmann glial cells and its modulation by glutamate receptor activation. *Glia*, *17*(4), 274–284. https://doi.org/10.1002/(SICI)1098-1136(199608)17:4<274::AID-GLIA2>3.0.CO;2-#

Muller, Thomas, & Kettenmann, H. (1995). Physiology of Bergmann glial cells. *International Review of Neurobiology*, *38*, 341–359. https://doi.org/10.1016/s0074-7742(08)60530-9

Nicholson, C., & Syková, E. (1998). Extracellular space structure revealed by diffusion analysis. *Trends in Neurosciences*, *21*(5), 207–215. https://doi.org/10.1016/S0166-2236(98)01261-2

Nimmerjahn, A., Mukamel, E. A., & Schnitzer, M. J. (2009). Motor behavior activates Bergmann glial networks. *Neuron*, *62*(3), 400–412. https://doi.org/10.1016/j.neuron.2009.03.019

Ormel, L., Lauritzen, K. H., Schreiber, R., & Kunzelmann, K. (2020). GABA, but Not

Bestrophin-1, is localized in astroglial processes in the mouse hippocampus and the cerebellum. *Frontiers in Molecular Neuroscience*, *13*(7), 1–14. https://doi.org/10.3389/fnmol.2020.00135

Ormel, L., Stensrud, M. J., Chaudhry, F. A., & Gundersen, V. (2012). A distinct set of synaptic-like microvesicles in atroglial cells contain VGLUT3. *Glia*, *60*(9), 1289–1300. https://doi.org/10.1002/glia.22348

Pakhotin, P., & Verkhratsky, A. (2005). Electrical synapses between Bergmann glial cells and Purkinje neurones in rat cerebellar slices. *Molecular and Cellular Neuroscience*, *28*(1), 79–84. https://doi.org/10.1016/j.mcn.2004.08.014

Palay, S. L., & Chan-Palay, V. (1974). The neuroglial cells of the cerebellar cortex. In S. L. Palay & V. Chan-Palay (Eds.), *Cerebellar cortex cytology and organization* (pp. 288–321). Springer. https://doi.org/10.1007/978-3-642-65581-4_11

Piet, R., & Jahr, C. E. (2007). Glutamatergic and purinergic receptor-mediated calcium transients in bergmann glial cells. *Journal of Neuroscience*, *27*(15), 4027–4035. https://doi.org/10.1523/JNEUROSCI.0462-07.2007

Poopalasundaram, S., Knott, C., Shamotienko, O. G., Foran, P. G., Dolly, J. O., Ghiani, C. A., Gallo, V., & Wilkin, G. P. (2000). Glial heterogeneity in expression of the inwardly rectifying K+ channel, Kir4.1, in adult rat CNS. *Glia*, *30*(4), 362–372. https://doi.org/10.1002/(SICI)1098-1136(200006)30:4<362::AID-GLIA50>3.0.CO;2-4

Price, D. L., Ludwig, J. W., Mi, H., Schwarz, T. L., & Ellisman, M. H. (2002). Distribution of rSlo Ca2+-activated K+ channels in rat astrocyte perivascular endfeet. *Brain Research*, *956*, 183–193. https://doi.org/10.1016/s0006-8993(02)03266-3

Rakic, P. (1971). Neuron-glia relationship during granule cell migration in developing cerebellar cortex. A Golgi and electronmicroscopic study in Macacus rhesus. *The Journal of Comparative Neurology*, *141*(3), 283–312. https://doi.org/10.1002/cne.901410303

Ramón y Cajal, S. (1911). *Histologie du systéme nerveux de l'homme et des vertébrés*.

Reichenbach, A., & Wolburg, H. (2013). Astrocytes and ependymal glia. In H. Kettenmann & B. R. Ransom (Eds.), *Neuroglia* (3rd ed., pp. 35–49). Oxford University Press. https://doi.org/10.1093/acprof:oso/9780195152227.003.0002

Reichenbach, A, Siegel, A., Rickmann, M., Wolff, J. R., Noone, D., & Robinson, S. R. (1995).

Distribution of Bergmann glial somata and processes: implications for function. *Journal Fur Hirnforschung*, *36*(4), 509–517.

Reichenbach, Andreas, & Wolburg, H. (2009). Structural association of astrocytes with neurons and vasculature: Defining territorial boundaries. In *Astrocytes in (Patho)Physiology of the Nervous System* (pp. 251–286). Springer US. https://doi.org/10.1007/978-0-387-79492-1_10

Riquelme, R., Miralles, C. P., & De Blas, A. L. (2002). Bergmann glia GABAA receptors concentrate on the glial processes that wrap inhibitory synapses. *Journal of Neuroscience*, *22*(24), 10720–10730. https://doi.org/10.1523/jneurosci.22-24-10720.2002

Rose, E. M., Koo, J. C. P., Antflick, J. E., Ahmed, S. M., Angers, S., & Hampson, D. R. (2009). Glutamate transporter coupling to Na,K-ATPase. *Journal of Neuroscience*, *29*(25), 8143–8155. https://doi.org/10.1523/JNEUROSCI.1081-09.2009

Roy, M. L., Saal, D., Perney, T., Sontheimer, H., Waxman, S. G., & Kaczmarek, L. K. (1996). Manipulation of the delayed rectifier Kv1.5 potassium channel in glial cells by antisense oligodeoxynucleotides. *Glia*, *18*(3), 177–184. https://doi.org/10.1002/(SICI)1098-1136(199611)18:3<177::AID-GLIA2>3.0.CO;2-X

Royeck, M., Horstmann, M., Remy, S., Reitze, M., Yaari, Y., & Beck, H. (2008). Role of Axonal Na V 1 . 6 Sodium Channels in Action Potential Initiation of CA1 Pyramidal Neurons. *J Neurophysiol*, *100*, 2361–2380. https://doi.org/10.1152/jn.90332.2008.

Rusakov, D. A. (2015). Disentangling calcium-driven astrocyte physiology. In *Nature Reviews Neuroscience* (Vol. 16, Issue 4, pp. 226–233). Nature Publishing Group. https://doi.org/10.1038/nrn3878

Saab, A. S., Neumeyer, A., Jahn, H. M., Cupido, A., Šimek, A. A. M., Boele, H.-J. J., Scheller, A., Le Meur, K., Götz, M., Monyer, H., Sprengel, R., Rubio, M. E., Deitmer, J. W., De Zeeuw, C. I., Kirchhoff, F., Simek, A. A. M., Boele, H.-J. J., Scheller, A., Le Meur, K., … Kirchhoff, F. (2012). Bergmann glial AMPA receptors are required for fine motor coordination. *Science*, *337*(August), 749–753. https://doi.org/10.1126/science.1221140

Sakai, K., Shimizu, H., Koike, T., Furuya, S., & Watanabe, M. (2003). Neutral amino acid transporter ASCT1 is preferentially expressed in L -Ser-synthetic/storing glial cells in the mouse brain with transient expression in developing capillaries. *The Journal of Neuroscience*, *23*(2), 550–560. https://doi.org/10.1523/JNEUROSCI.23-02-00550.2003

Salas, E., Carrasquero, L. M. G., Olivos-Oré, L. A., Bustillo, D., Artalejo, A. R., Miras-Portugal, M. T., & Delicado, E. G. (2013). Purinergic P2X7 receptors mediate cell death in mouse cerebellar astrocytes in culture. *Journal of Pharmacology and Experimental Therapeutics*, *347*(3), 802–815. https://doi.org/10.1124/jpet.113.209452

Savtchenko, L. P. (2018). *ASTRO 1.0. User Guide*. https://github.com/LeonidSavtchenko/Astro

Savtchenko, L. P., Bard, L., Jensen, T. P., Reynolds, J. P., Kraev, I., Medvedev, N., Stewart, M. G., Henneberger, C., & Rusakov, D. A. (2018). Disentangling astroglial physiology with a realistic cell model in silico. *Nature Communications*, *9*(3554). https://doi.org/10.1038/s41467-018-05896-w

Schaller, K. L., & Caldwell, J. H. (2003). Expression and distribution of voltage-gated sodium channels in the cerebellum. *The Cerebellum*, *2*, 2–9. https://doi.org/10.1080/14734220309424

Schiweck, J., Eickholt, B. J., & Murk, K. (2018). Important shapeshifter: Mechanisms allowing astrocytes to respond to the changing nervous system during development, injury and disease. *Frontiers in Cellular Neuroscience*, *12*(August), 1–17. https://doi.org/10.3389/fncel.2018.00261

Siegel, A., Reichenbach, A., Hanke, S., Senitz, D., Brauer, K., & Smith, T. G. (1991). Comparative morphometry of Bergmann glial (Golgi epithelial) cells - A Golgi study. *Anatomy and Embryology*, *183*(6), 605–612. https://doi.org/10.1007/BF00187909

Singaravelu, K., Lohr, C., & Deitmer, J. W. (2006). Regulation of store-operated calcium entry by calcium-independent phospholipase A2 in rat cerebellar astrocytes. *Journal of Neuroscience*, *26*(37), 9579–9592. https://doi.org/10.1523/JNEUROSCI.2604-06.2006

Sofroniew, M. V., & Vinters, H. V. (2010). Astrocytes: Biology and pathology. *Acta Neuropathologica*, *119*(1), 7–35. https://doi.org/10.1007/s00401-009-0619-8

Suárez-Pozos, E., Martínez-Lozada, Z., Méndez-Flores, O. G., Guillem, A. M., Hernández-Kelly, L. C., Castelán, F., Olivares-Bañuelos, T. N., Chi-Castañeda, D., Najimi, M., & Ortega, A. (2017). Characterization of the cystine/glutamate antiporter in cultured Bergmann glia cells. *Neurochemistry International*, *108*, 52–59. https://doi.org/10.1016/j.neuint.2017.02.011

Sylantyev, S., Savtchenko, L. P., Ermolyuk, Y., Michaluk, P., & Rusakov, D. A. (2013). Spike-

driven glutamate electrodiffusion triggers synaptic potentiation via a homer-dependent mGluR-NMDAR link. *Neuron*, *77*(3), 528–541. https://doi.org/10.1016/j.neuron.2012.11.026

Tamamushi, S., Nakamura, T., Inoue, T., Ebisui, E., Sugiura, K., Bannai, H., & Mikoshiba, K. (2012). Type 2 inositol 1,4,5-trisphosphate receptor is predominantly involved in agonist-induced Ca2+ signaling in Bergmann glia. *Neuroscience Research*, *74*(1), 32–41. https://doi.org/10.1016/j.neures.2012.06.005

Tanaka, M., Yamaguchi, K., Tatsukawa, T., Theis, M., Willecke, K., & Itohara, S. (2008). Connexin43 and Bergmann glial gap junctions in cerebellar function. *Frontiers in Neuroscience*, *2*(2), 225–233. https://doi.org/10.3389/neuro.01.038.2008

Thompson, C. L., Drewery, D. L., Atkins, H. D., Stephenson, F. A., & Chazot, P. L. (2000). Immunohistochemical localization of N-methyl-D-aspartate receptor NR1, NR2A, NR2B and NR2C/D subunits in the adult mammalian cerebellum. *Neuroscience Letters*, *283*(2), 85–88. https://doi.org/10.1016/S0304-3940(00)00930-7

Thomzig, A., Wenzel, M., Karschin, C., Eaton, M. J., Skatchkov, S. N., Karschin, A., & Veh, R. W. (2001). Kir6.1 is the principal pore-forming subunit of astrocyte but not neuronal plasma membrane K-ATP channels. *Molecular and Cellular Neuroscience*, *18*(6), 671–690. https://doi.org/10.1006/mcne.2001.1048

Tuschick, S., Kirischuk, S., Kirchhoff, F., Liefeldt, L., Paul, M., Verkhratsky, A., & Kettenmann, H. (1997). Bergmann glial cells in situ express endothelinB receptors linked to cytoplasmic calcium signals. *Cell Calcium*, *21*(6), 409–419. https://doi.org/10.1016/s0143-4160(97)90052-x

Uebachs, M., Opitz, T., Royeck, M., Dickhof, G., Horstmann, M., Isom, L. L., & Beck, H. (2010). Efficacy Loss of the Anticonvulsant Carbamazepine in Mice Lacking Sodium Channel Beta Subunits via Paradoxical Effects on Persistent Sodium Currents. *The Journal of Neuroscience*, *30*(25), 8489–8501. https://doi.org/10.1523/JNEUROSCI.1534-10.2010

Untiet, V., Kovermann, P., Gerkau, N. J., Gensch, T., Rose, C. R., & Fahlke, C. (2017). Glutamate transporter-associated anion channels adjust intracellular chloride concentrations during glial maturation. *Glia*, *65*(2), 388–400. https://doi.org/10.1002/glia.23098

Verkhratsky, A., & Reichenbach, A. (2009). Bergmann glial cells. In *Encyclopedia of Neuroscience* (pp. 161–171). Elsevier Ltd. https://doi.org/10.1016/B978-008045046-9.00999-2

Verkhratsky, Alexei, & Nedergaard, M. (2018). Physiology of astroglia. *Physiological Reviews*, *98*(1), 239–389. https://doi.org/10.1152/physrev.00042.2016

Verkhratsky, Alexei, & Parpura, V. (2015). Physiology of astroglia: channels, receptors, transporters, ion signaling and gliotransmission. *Physiological Reviews*, *98*(1), 239–389. https://doi.org/10.1152/physrev.00042.2016

von Bartheld, C. S., Bahney, J., & Herculano-Houzel, S. (2016). The search for true numbers of neurons and glial cells in the human brain: A review of 150 years of cell counting. *Journal of Comparative Neurology*, *524*(18), 3865–3895. https://doi.org/10.1002/cne.24040

Voogd, J., & Glickstein, M. (1998). The anatomy of the cerebellum. *Trends in Cognitive Sciences*, *2*(9), 307–313. https://doi.org/10.1016/S1364-6613(98)01210-8

Xu-Friedman, M. A., Harris, K. M., & Regehr, W. G. (2001). Three-dimensional comparison of ultrastructural characteristics at depressing and facilitating synapses onto cerebellar Purkinje cells. *Journal of Neuroscience*, *21*(17), 6666–6672. https://doi.org/10.1523/jneurosci.21-17-06666.2001

Yamada, K., & Watanabe, M. (2002). Cytodifferentiation of Bergmann glia and its relationship with Purkinje cells. *Anatomical Science International / Japanese Association of Anatomists*, *77*(2), 94–108. https://doi.org/10.1046/j.0022-7722.2002.00021.x

Yoon, B., Woo, J., Chun, Y., Chun, H., Jo, S., Bae, J. Y., An, H., Min, J. O., Oh, S., Han, K., Kim, H. Y., Kim, T., Kim, Y. S., Bae, Y. C., & Lee, C. J. (2014). Glial GABA, synthesized by monoamine oxidase B , mediates tonic inhibition. *J Physiol*, *592*(22), 4951–4968. https://doi.org/10.1113/jphysiol.2014.278754

Zafra, F., Aragon, C., Olivares, L., Danbolt, N. C., Gimenez, C., & Storm-Mathiesen, J. (1995). Glycine transporters are differentially expressed among CNS cells. *The Journal of Neuroscience*, *15*(5), 3952–3969. https://doi.org/10.1523/JNEUROSCI.15-05-03952.1995

Zhou, H., Lin, Z., Voges, K., Ju, C., Gao, Z., Bosman, L. W. J., Ruigrok, T. J., Hoebeek, F. E.,

De Zeeuw, C. I., & Schonewille, M. (2014). Cerebellar modules operate at different frequencies. *ELife*, *2014*(3). https://doi.org/10.7554/eLife.02536

Zhou, M., Tanaka, O., Suzuki, M., Sekiguchi, M., Takata, K., Kawahara, K., & Abe, H. (2002). Localization of pore-forming subunit of the ATP-sensitive K+-channel, Kir6.2, in rat brain neurons and glial cells. *Molecular Brain Research*, *101*(1–2), 23–32. https://doi.org/10.1016/S0169-328X(02)00137-7